



**EFFECT OF TEMPERATURE IN
CATHODIC ELECTRODEPOSITION
OF ANATASE TiO₂ FILMS ON
CONDUCTIVE GLASS**

CARLOS FERNANDO CRUZ BLANCO
SCHOOL OF ENGINEERING AND MATERIALS SCIENCE
QUEEN MARY UNIVERSITY OF LONDON

MPhil Thesis

June 2014

London, UK

Declaration

I hereby declare that the work carried out and presented in this thesis is based on my own work and that it has not been submitted as an exercise for any other qualification. Wherever contributions of others were involved, it is fully acknowledged.

Name CARLOS FERNANDO CRUZ BLANCO

Signature

Date

Abstract

Polycrystalline titania (TiO_2) films were prepared on the ultrasonically cleaned indium tin oxide glass (ITO) substrates on high temperature annealing of TiO_2 hydrates electrodeposited from the chemical bath of titanyl sulphate at room temperature and above. The film grew in thickness monotonically from 53nm to 113nm with the rise in bath temperature at constant bath deposition time. The bath temperature was found to be important for the extent to which the anatase phase was achieved for a given set of annealing temperatures and deposition times.

The Raman spectra of the annealed films which were deposited at the bath temperature of 336K exhibited distinct anatase phase. Optical (UV/vis absorption) in the annealed TiO_2 was found to be due to indirect allowed transitions over the band gap of 3.4eV. The experimental data was analysed in Tauc and Urbach regions. The Urbach energy obtained for the films deposited at 336K was equal to 0.26eV and showed an almost linear relationship.

The transformation from amorphous to crystalline structure on annealing was observed in the XRD pattern and the AFM images. The grain size was estimated to be 88nm from XRD measurements.

The correct stoichiometry of the TiO_2 film was achieved according to the X-ray photoelectron analysis. An extended study including interactions between temperature of the bath and deposition potential is finally recommended to optimise even more the film preparation method.

Acknowledgements

I would like to express my deepest appreciation to both my supervisors: Professor Asim Ray and Professor Paul Hogg. They gave me the opportunity.

I am also thankful to Dr Rory Wilson, Dr Zofia Luklinska, Prof Ken Scott and Dr Jesus Ojeda for helping me during different stages of this project.

Special thanks to my friends and colleagues at Queen Mary during these years, Marjan, Zahra, Shweta, Elnaz, Guillermo, Jasminder and Bea.

Thank you to Ivonne Marcela, Silvia, Jana, Nora and Adam, Father John and Reverend Jenny for their love, support and inspiration.

Sincere thanks to my family in Colombia for everything they provided me with to be where I am now.

Lastly, I offer my regards and blessings to all of those who supported me in any respect during the completion of this work.

Table of Contents

Declaration	ii
Abstract	iii
Acknowledgements	iv
Table of Contents.....	v
List of Figures.....	vii
List of Tables	xi
Chapter One.....	12
Introduction	12
Chapter Two	14
Literature Review	14
2.1 Introduction	14
2.2 Applications of titanium dioxide	14
2.3 Physical properties of titania	16
2.4 Crystallographic structure of titania	17
2.5 Electronic Properties of TiO₂.....	21
2.5.1 Energy Band Diagram for Anatase and Rutile titania.....	22
2.6 Effect of Temperature, Partial Pressure and Doping on conductivity of TiO₂.....	25
2.6.1 Temperature and Doping Dependence of Electrical Conductivity.	26
2.6.1.1 Titanium Dioxide Films Conductivity at Different Temperature Regions.	26
2.6.1.2 Titanium Dioxide crystals	33
2.6.2 Effect of Doping on electrical conductivity of titania	38
2.7 Cathodic electrodeposition of TiO₂ films.....	39
2.8 Peroxo Complexes of Titanium	40
Chapter Three	49
Experimental Methodology	49
3.1 Introduction	49
3.2 Substrate Preparation.....	50
3.3 Safety Considerations	50
3.4 Preparation of the Peroxo titanium complex	51
3.5 Exploratory experiments.....	52
3.5.1 Temperature vs pH of the Electrolytic Bath.....	52
3.5.2 Cyclic Voltammetry	52
3.6 Film electrodeposition.	54
3.7 Characterisation Methods and Equipment.....	57

3.7.1 Raman Spectroscopy	57
3.7.2. UV-Visible Spectroscopy	59
3.7.3. X-Ray Diffraction	62
3.7.4. The Scanning Electron Microscope (SEM)	64
3.7.5. Energy Dispersive X-Ray Spectroscopy (EDX)	67
3.7.6. X-Ray Photoelectron Spectroscopy	69
3.7.7. Surface profilometry	70
3.7.8. Non-Contact Atomic Force Microscopy	72
Chapter 4	75
4.1 Introduction	75
4.2 pH variation in electrochemical solution due to Temperature	75
4.3 Results of Cyclic Voltammetry	78
4.4 Chemical analysis of electrodeposited titania films by Raman spectral analyses .	82
4.5 Energy dispersive spectroscopy	84
4.6 Optical characterisation	84
4.7 X-Ray Diffraction	88
4.8 X- Ray photoelectron spectroscopy of TiO ₂	92
4.9 TiO ₂ film surface microstructure	94
4.10 Atomic force scans of as-deposited and heat-treated TiO ₂ films	96
Chapter 5	98
References	101
Publication	108

List of Figures

Figure 2.1. Rutile unit cell. Modified from references [21] and [22]	19
Figure 2.2. Schematic crystal structure of rutile consisting of 9 egde-sharing TiO ₆ octahedra. Modified from references [22] and [23].	19
Figure 2.3. Anatase unit cell. From [21] and [22]	20
Figure 2.4. Schematic crystal structure of anatase showing the TiO ₆ octahedra stacking. From [22] and [23].	21
Figure 2.5. Schematic atomic d ₂ sp ₃ hybridization/bonding orbitals orbital arrangement in titanium. The nucleus is embedded in the minor lobe. The six orbitals are separated for easier view [24].	22
Figure 2.6. Molecular orbital arrangements for (a) rutile and (b) anatase TiO ₂ , showing two different energy d-orbitals in anatase. Modified for easier view from [24].	23
Figure 2.7. Density of States (DOS) for rutile and anatase, showing the narrower high occupied and lower unoccupied states for anatase. Taken from [26]	24
Figure 2.8. Band structure for rutile and anatase TiO ₂ without doping. The minimum of the balance band is set as 0eV. On the right, the Brillouin zone of simple tetragonal lattice for guidance. Combined from references [22] and [26].	25
Figure 2.9. Resistivity ρ vs 1000/T on anatase (\square) and rutile (\bullet) films: (1) as deposited; (2) reduced at 400°C for 2h; (3) reduced at 450°C for 2h. Modified from [29].	27
Figure 2.10. Dependences $\ln\delta = f(103/T)$ plotted for anatase and rutile sputtered films, in the range 13-320K. Adjusted for easier view from reference [31].	29
Figure 2.11. Dependences $\ln\delta = f(103/T)$ in anatase and rutile films according to reference [31], in the range 310 -468 K.	29
Figure 2.12. $\ln\sigma$ versus 103 /T plotted for a sample: on the left, polycrystalline anatase thin film; on the right, polycrystalline rutile thin film. The dot arrows show the evolution during the heat treatment, while the solid vertical arrows mark the chosen temperature domains [32].	30
Figure 2.13. Dependences $\ln\sigma = f(10^3/T)$ plotted in the range 120K-320K for anatase and rutile samples. Adjusted for easier view from reference [32].	31

Figure 2.14. Temperature dependence of the electrical resistivity of rutile and anatase TiO ₂ sample in vacuum. From reference [35].	33
Figure 2.15. High temperature conductivity plot for rutile TiO ₂ crystals perpendicular to c axis [36].	34
Figure 2.16. High temperature conductivity plot for rutile TiO ₂ parallel to c axis [36].	35
Figure 2.17. Temperature dependence of the resistivity of an as-grown anatase single crystal [37].	36
Figure 2.18. Temperature dependent conductivity of TiO ₂ as a plot of lnσ vs. T. The thermal activation energy of conductivity is obtained from slope of straight the line [38].	37
Figure 2.19. Conductivity as a function of oxygen pressure. A - rutile, 968°C; B- rutile, 820°C; C- anatase, 81°C [39].	38
Figure 2.20. Configuration of the titanium complex C ₁₄ H ₁₆ N ₂ O ₁₈ K ₂ Ti ₂ . The distances of the bonds are given in Å. Only bonds surrounding the Ti atom are detailed. From reference [62].	44
Figure 2.21. On the left: Tinanyl sulphate hydrate structure; on the right: structure of tinanyl sulphate monohydrate viewed along (010). Modified for easier view from reference [64].	46
Figure 2.22. Structure of pseudooctahedral mononuclear peroxo complexes of titanium: [Ti (O ₂) (Pic) ₂ (HMPT)]. From reference [65].	47
Figure 2.23. Structure of pseudooctahedral binuclear peroxo complexes of titanium: [{Ti (O ₂)(Dipic)(H ₂ O)} ₂ (μ-O)] ²⁻ [65].	47
Figure 2.24. Structure of a tetranuclear peroxo complex of titanium: [{Ti(O ₂)(μ-Cit)} ₄] ⁸⁻ [65].	48
Figure 3.1. Schematic representation of cyclic voltammetry.	53
Figure 3.2. Schematic representation of the diffusion double layer at the electrode surface.	55
Figure 3.3. Three electrode set up used for the electrodeposition of TiO ₂ . Reference electrode (Ag/AgCl); working electrode (Indium doped Tin Oxide); Platinum wire was employed as counter electrode.	56
Figure 3.4 Schematic illustration of the vibrational energy state involved in Raman signal.	57
Figure 3.5 Schematic configuration of Raman spectroscopy.	58

Figure 3.6. Ultraviolet and visible light spectra configuration [71].....	61
Figure 3.7. Schematic illustration showing the scattered x-ray deflected beam	62
Figure 3.8 Bragg's Law. Constructive scattering of deflected waves [72].	63
Figure 3.9 Diagram showing the components of SEM [74].	66
Figure 3.10 Illustration of the atomic structure and the principle of EDX [74].....	68
Figure 3.11 Schematic diagram of X-ray photoelectron spectroscopy [78]	70
Figure 3.12. Principle of Profilometer [78].	71
Figure 3.13 Schematic illustration of Atomic Force Microscopy (AFM)[80].	73
Figure 4.1. Cyclic voltammetry for the redox pairs; $\text{TiOSO}_4:\text{NH}_3\text{NO}_4$, $\text{TiOSO}_4:\text{H}_2\text{O}_2$ and $\text{NH}_3\text{NO}_4:\text{H}_2\text{O}_2$	79
Figure 4.2. Experimental voltammetry of Peroxo-titanium in a aqueous solution at a scan rate of 120m V/min, pH 1.3, 293K. There is a rapid increase in current around around -1.2 V corresponding to the formation of metallic Ti.	81
Figure 4.3. Raman Spectra for TiO_2 films electrodeposited at temperatures: (a) 296K, (b) 318K, (c) 336K and (d) 353K. The Raman values for anatase peaks are shown for reference (anatase powder from Aldrich)	82
Figure 4.4 Optical absorption spectrum of TiO_2 films of ITO glass at different bath temperatures (a) 296K, (b) 318K, (c) 336K and (d) 353K. All samples were heat treated at (823 in air for 30 min). (e) Tauc region for the near the absorption edge, (f) Urbach low energy tail.	85
Figure 4.5. Numerical fitting of Y'/Y vs $h\nu$. Y' is the numerical differentiation for A $h\nu$ vs. $h\nu$. The inverse of the slope is the exponent n in the Tauc equation.	86
Figure 4.6. From the inverse of the slope of the linear part of the curve (Urbach region) is E_u (Urbach energy) for TiO_2 film electrodeposited at 296K, -1.2V (potential).	87
Figure 4.7 XRD of TiO_2 precipitated after heating the solution. a) As precipitated. b) After annealing at 823K for 30 min.	89
Figure 4.8 XRD of TiO_2 electrodeposited film (-1.2V; 30 min, 336K) as deposited (a) and after annealed at 823K for 30 min (b). Anatase peaks for different crystallographic planes are labelled. The peaks from the conductive glass Indium doped tin oxide (ITO) glass substrate are marked as solid circles (\bullet). The inset shows the linear fitting of the Hull equation.	90
Figure 4.9. XPS spectra of titanium hydroxide gel film deposited at room temperature. The $2p_{1/2}$ and $2p_{3/2}$ peaks correspond to Ti^{+4} typical of anatase. ...	93

Figure 4.10 SEM photograph of TiO ₂ electrodeposited film as deposited (deposition temperature, 338K) and further annealing at 823K for 30 min.	94
Figure 4.11 SEM photograph of TiO ₂ electrodeposited films as deposited (A – deposition temperature, 338K; B – deposition temperature, 353K)	95
Figure 4.12 SEM photograph of TiO ₂ electrodeposited films as deposited (A – deposition temperature, 338K; C – deposition temperature, 353K) and after annealing at 823K for 30 min (C,D) submicrophotography of film in (A). Cracks are visible on the films.....	96
Figure 4.13 AFM images for TiO ₂ films electrodeposited at 336K. A (as deposited). B (after annealing at 823K for 30 min).....	97

List of Tables

Table 2.1. Physical properties of titanium dioxide (bulk form) [19].....	16
Table 2.2. Crystallographic parameters of TiO ₂ polymorphs [19]	17
Table 2.3. Interionic distances in TiO ₂ anatase and rutile, in Å [20]. Values differ slightly from the ones reported in Figures 1 and 3.	18
Table 2.4 Dependency of colour and transparency of a peroxy titanium complex solution with its pH. Taken from [61].....	41
Table 4.1 Experimental variation of pH of Peroxy Titanium solution at different temperatures.	76
Table 4.2. Colour variation of the Peroxy Titanium solution at different temperatures and its correspondent pH value.....	77
Table 4.3 Raman Peak positions and their assignment for anatase.....	83
Table 4.4 Parameters derived from optical absorption spectra.	88
Table 4.5. XRD peaks for TiO ₂ electrodeposited films (Experimental and Standard [95])	91

Chapter One

Introduction

The past thirty years have seen increasingly rapid advances in the field of microelectronics and nanotechnology. Titania is one of the most widely used materials in this industry due to its very interesting optical and electrical properties (high permittivity, high transmittance in the visible region and non-toxicity) which make it an important component in diverse applications such as: solar cells, chemical sensors, photo catalysts, cellular therapies and tissue engineering. Many manufacturing processes have been developed to obtain high quality films, and electrodeposition is one of the most versatile due to its controllability and low cost. Although extensive research has been carried out on TiO₂, no single study exists which adequately covers the effect of bath temperature in the cathodic electrodeposition of titania films.

The aim of this research is to determine whether increasing the temperature of the electrochemical bath improves the optical properties of titania films, while keeping constant other possible variables such as the composition of the bath, electrodeposition potential, deposition time and heat treatment.

The dissertation has been organised in the following way: Chapter 1 begins by laying out the different properties of TiO₂ relevant to the field of opto-electronics as well as examining the main characteristics and chemistry of the peroxo-complexes of titanium, which is an intermediate agent of the manufacturing process of the titania films. Chapter 2 will present the theoretical dimensions of the exploratory experiments, and the preparation and characterisation methods used in the present research. Instruments and technical specifications employed in the different analysis are also included.

Chapter 3 assesses the exploratory experiments in addition to the design, synthesis, and evaluation of the titania films produced. Chapter 4 includes the analysis and discussion of the results obtained. This chapter includes optical parameters including Urbach energy and band gap energy.

Chapter 5 outlines the conclusions and possibilities and proposals for future research stemming from this work.

Chapter Two

Literature Review

2.1 Introduction

Titania (TiO₂) has been extensively studied in thin-film forms and other arrays, for a wide spectrum of applications depending on the different treatments that are capable of inducing alterations to its physical and chemical properties. As there is a remarkable range of practical uses of titanium dioxide, the scope of this revision will be limited and categorised by the properties of titania more relevant to the particular usages.

2.2 Applications of titanium dioxide

TiO₂ acts as a structural support material, in the form of layers, either encapsulating or bedding metal clusters (Va, Au, etc.) for heterogeneous catalysis of oxidation reactions and is codeposited in binary films with other oxides for catalysis (Ni, Zn, WO₃, RuO₂/Al₂O₃) [1][2][3][4].

Due to its high refractive index (2.52-2.96) [5], TiO₂ is extensively employed as a white pigment and thickener in paints [6]; titania possesses a high dispersing capability and is also nontoxic, which makes it ideal for its use in cosmetics and food additives (when used in pure form) and in pharmaceuticals, as a drug delivery agent [7],[8]. The titania index of refraction is also advantageous for optical interference thin-film coatings which become a component for anti-reflective layers in glass windows, multilayer mirrors for lasers and optical filters [9].

Titanium dioxide coated surface and pigments are hydrophilic (0° water contact angle), and are employed as a coating on lighting bulbs and ceramic tiles and as a self-cleaning smart materials [10][11].

Titania is a highly active photocatalytic material which is preferred for the elimination and decomposition of organic pollutants and other chemical compounds, in aqueous solution or in gas phase, by generating free radicals under UV radiation that oxidise organic material. This characteristic has been employed for environmental clean-up in the decomposition of the nitrogen oxide molecules present in waste gases from coal power plants, the cleaning of exhaust gases of diesel engines, purification of air and water, and for sterilising and deodorising. As well as its capacity for photodissociation of water [12], a further advantage of the photocatalytic activity of titanium dioxide applied in pigments is its good resistance to UV and chemical degradation while maintaining a good thermal stability [11].

Titanium dioxide characterised by ultrafine particle size (1-150nm) transmits visible light while scattering UV radiation, this leads to its use as a UV blocker in sunscreen and plastics, catalysts and colour pigment precursors and in electroceramics [13][14].

Although the titanium dioxide quantum yield photochemical of solar energy is not very high, the combination of colloidal suspensions of TiO₂ with different kinds of dye compounds has resulted in low-cost high-photovoltaic power conversion efficiency solar cells [15].

The high dielectric constant of titanium dioxide (86-173) [5] has made TiO₂ an interesting candidate for metal–oxide–semiconductor–field-effect transistor (MOSFET) devices, as a gate insulator for capacitors.

Cobalt doped TiO₂ films are ferromagnetic, as well as maintaining its semiconduct-

ing nature. This quality has been studied for its use in electronic devices [16]. Additionally, it has been found that by controlling the presence and nature of defects of titanium dioxide via doping, it has been possible to use TiO₂ as chemical gas sensor [17].

Finally, it is important to mention some applications of titanium dioxide in biomedical research, which take advantages of the different chemical and physical properties of this oxide. The excellent corrosion resistance of TiO₂ allows its inclusion in the manufacturing of alloys, ceramics and composite implants and hard coatings which improve the lifetime of prosthetics and dental fillings. Its bio-compatibility with animal tissue has permitted the use of titania as a total track digestibility marker for ruminants [18].

Such a diversity of practical uses is mainly due to a useful blend of optical and electronic properties in addition to chemical and thermal stability. In the next section, relevant knowledge about different properties of titanium dioxide will be discussed.

2.3 Physical properties of titania

As mentioned above, titanium dioxide possesses a very interesting mix of properties that can be taken into advantage separately or combined to obtain different effects in the miscellaneous group of applications detailed in the previous section. Some physical and mechanical properties of titanium dioxide are summarised in table 2.1:

Table 2.1. Physical properties of titanium dioxide (bulk form) [19]

Atomic radius (nm)		
O	0.066 (covalent)	
Ti	0.146 (metallic)	
Ionic radius (nm)		
O(-2)	0.14	
Ti(+4)	0.064	
Density (kg/m ³)	Rutile	4240
	Anatase	3830
Standard heat capacity, C _p ^o , 298.15 J/(mol °C)	Brookite	4170
	Rutile	55.06
Standard heat capacity, C _p ^o , 298.15 J/(mol °C)	Anatase	55.52

Since the properties presented above are not sufficient to support the understanding of the processes, experimental methods employed and repercussions of the result of the present research, along with the mechanical properties it is necessary to complement the scope of the discussion with the crystallographic, optical, electronic and electrical properties of titania.

2.4. Crystallographic structure of titania

Titanium dioxide crystallises in three major structures: rutile, anatase and brookite (as showed in the density data in Table 2.1). Commercially, rutile and anatase are the most utilised polymorphs and also the most studied.

Table 2.2, the main crystallographic descriptive characteristics of these structures are listed.

Table 2.2. Crystallographic parameters of TiO₂ polymorphs [19]

Crystal Structure	System	Space group	Lattice constants (nm)			
			a	b	c	c/a

Rutile	Tetragonal	D ¹⁴ _{4h} -P4 ₂ /nm	0.4	-	0.2	0.
			584		953	644
Anatase	Tetragonal	D ¹⁹ _{4h} -I4 ₁ /amd	0.3	-	0.9	2.
			733		37	51
Brookite	Rhombohedral	D ¹⁵ _{2h} -Pbca	0.5436	0.9166	0.5135	0.944

In both, rutile and anatase structures, slightly distorted TiO₆ octahedra are the basic building units of the lattice. Structural characteristics have been found to affect optical and electronic properties of TiO₂ polymorphs. The differences in interionic distances between Ti and O are shown in Table 2.3.

Table 2.3. Interionic distances in TiO₂ anatase and rutile, in Å [20]. Values differ slightly from the ones reported in Figures 1 and 3.

	Anatase	Rutile
Ti-Ti [1]	3.04	2.96
Ti-Ti [2]	3.79	3.57
Ti-O [1]	1.91	1.94
Ti-O [2]	1.95	1.99
O-O [1]	2.45	2.52
O-O [2]	2.80	2.78
O-O [3]	3.04	2.96

The unit cell of rutile is showed schematically in Figure 2.1. Rutile has a structure built of quasi-hexagonal closed packed (HCP) oxygen atoms. As the Ti⁺⁴ cations fill one-half of the available octahedral sites in this HCP, the resulting cell is tetragonal with two TiO₂ molecules per unit cell. Due to the partial occupancy of the sites by the highly charged Ti⁺⁴ ions, the atoms are displaced slightly from their positions in the perfect HCP lattice.

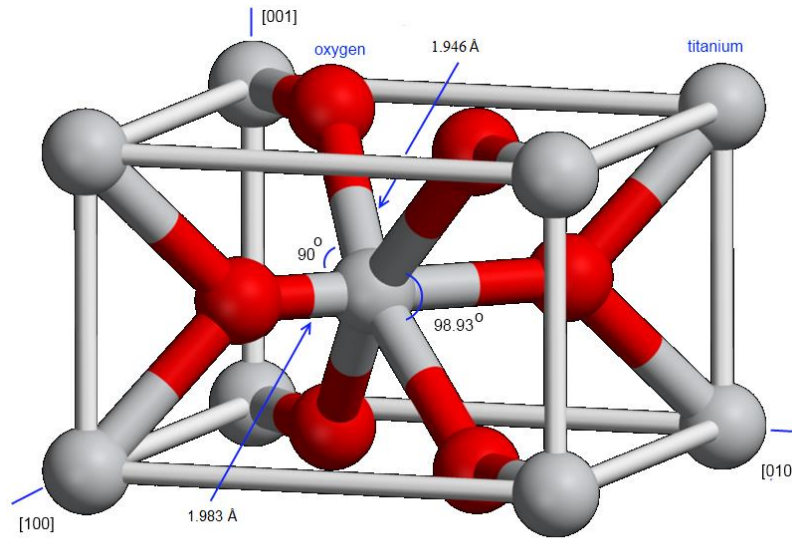


Figure 2.1. Rutile unit cell. Modified from references [21] and [22]

The crystal structure of rutile, shown in Figure 2.2, consists of TiO₆ octahedra that share corners and faces in a way that each oxygen atom is shared by three octahedra forming an edge-sharing-perpendicularly intercalated stacking of such octahedra.

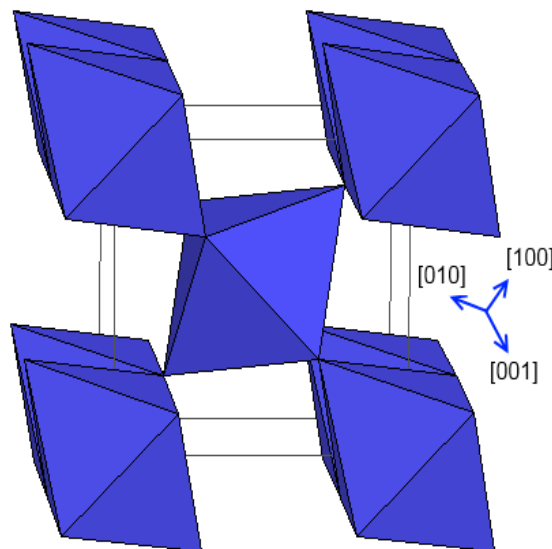


Figure 2.2. Schematic crystal structure of rutile consisting of 9 edge-sharing TiO₆ octahedra. Modified from references [22] and [23].

Anatase, on the other hand, contains four molecules per unit cell and is a metastable phase compared to the stable rutile phase. The TiO₆ octahedra configuration is distort-

ed into a less symmetric structure in anatase, so forming a larger unit cell with lower density.

The schematic structure of the anatase unit cell is shown in Figure 2.3.

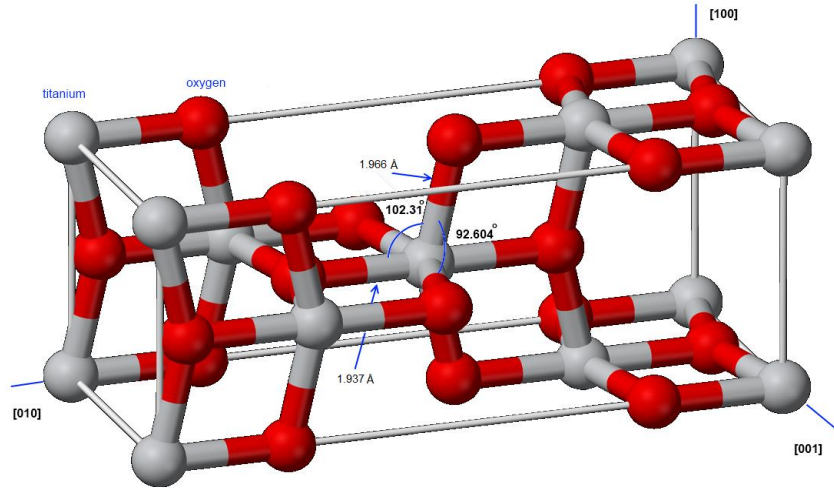


Figure 2.3. Anatase unit cell. From [21] and [22]

The basic building block of anatase consists of one titanium atom surrounded by six oxygen atoms (similar to rutile). A comparison between the atomic distances in the two structures, figures 1 and 3, shows that the two bonds between Ti and O atoms at each apex of the octahedron are slightly shorter in anatase than in rutile. The corner-sharing octahedra form (001) planes. The stacking is then formed by joining the edges of the octahedra in each two parallel planes. As a result each octahedron is in contact with eight neighbours with four octahedra sharing an edge and the other four sharing a corner as shown in Figure 2.4.

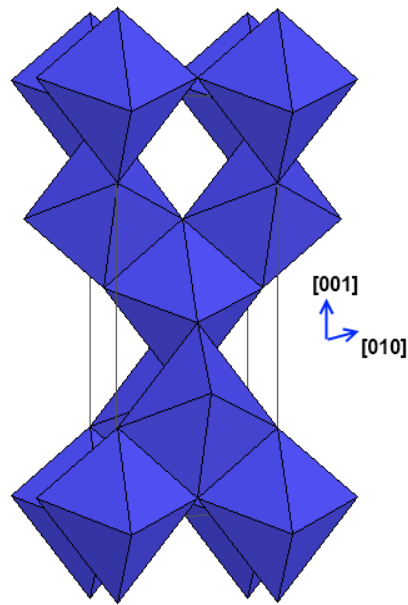


Figure 2.4. Schematic crystal structure of anatase showing the TiO₆ octahedra stacking. From [22] and [23].

2.5 Electronic Properties of TiO₂

This section reviews the literature concerning the electronic properties of TiO₂ as its understanding is central to the entire discipline of optical absorption and electrical conduction.

The electronic configurations of Ti and O atoms, that combine to give titania, are $1s^2, 2s^2, 2p^6, 3s^2, 3p^6, 4s^2, 3d^2$ for titanium and $1s^2, 2s^2, sp^4$ for oxygen. As a transition metal, titanium exhibits various oxidation states (+2, +3, +4) of which +4 and +3 the most common. It also forms d^2sp^3 hybridization/bonding orbitals with d shells available for bonding. These particular hybrids are a combination of two 3d (from $d_{yz}, d_{xz}, d_{xy}, d_{x^2-y^2},$ and d_{z^2}), one 3s, and three 3p ($p_x, p_y,$ and p_z) orbitals all of which participate in the bonding. In synthesis, there are six d^2sp^3 hybrid orbitals arranged in an octahe-

dral layout, which gives the basic electronic structure to titania as illustrated in figure 2.5:

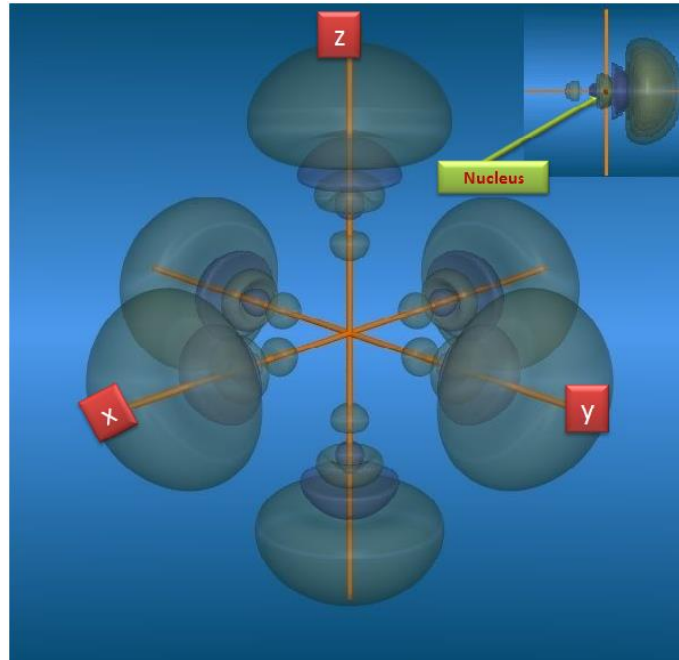


Figure 2.5. Schematic atomic d₂sp₃ hybridization/bonding orbitals orbital arrangement in titanium. The nucleus is embedded in the minor lobe. The six orbitals are separated for easier view [24].

2.5.1 Energy Band Diagram for Anatase and Rutile titania

Both titania polymorphs (anatase and rutile) are wide-gap insulators when stoichiometric, with band gaps of 3.0eV (rutile) and 3.2eV (anatase) [25]. The octahedral coordination, explained in the last section, causes a crystal-field splitting of the d bands orbitals into two sub-bands.

Figure 2.6 shows a comparison of the schematic molecular orbital diagrams.

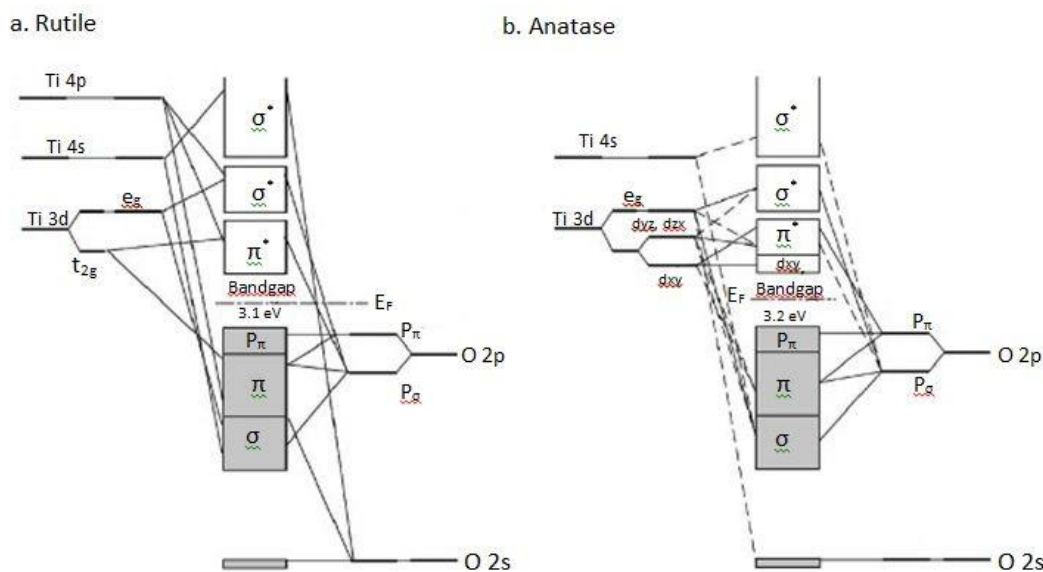
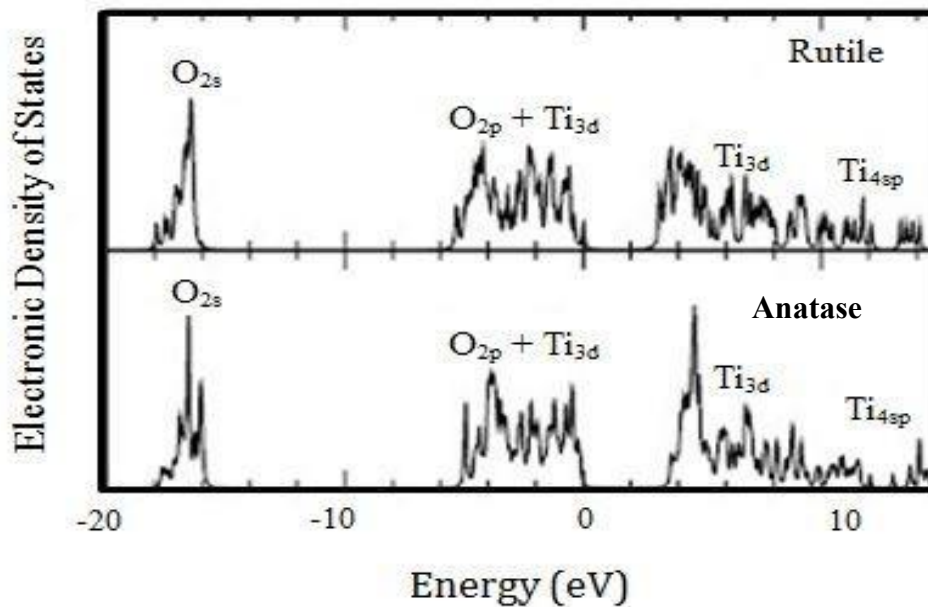


Figure 2.6. Molecular orbital arrangements for (a) rutile and (b) anatase TiO₂, showing two different energy d-orbitals in anatase. Modified for easier view from [24].

For both titanium dioxide phases, the e_g orbitals (d_{z^2} and $d_{x^2-y^2}$) point straight to the incoming oxygen ligands, forming σ -type orbitals and increasing its potential energy. The d_{xy} , d_{xz} and d_{yz} orbitals (t_{2g} orbitals) are concentrated in the space between the oxygen ligands and form π -type interactions [22]. This means that the d-orbitals divide into two groups, one lower energy than the other, as shown in Figure 2.6. (b).

Structural differences between anatase and rutile (Table 2.3) showed that the rutile structure is more regular, more dense, and the metal-metal bonds are shorter than anatase. The lower symmetry of the Ti sites (TiO_6^{-8} ions) in anatase lifts degeneracies between d_{yz} , d_{zx} and d_{xy} leaving the nonbonding d_{xy} states isolated at the bottom of the conduction band and their corresponding nonbonding $O_{p\pi}$ orbitals at the top of the valence bands, resulting in a narrow conduction band, as discussed below.

The Density of States (DOS) in Figure 2.7 shows that the lower energy bands around -17 eV result from a predominantly oxygen 2s (O_{2s}) character with a width of 1.89eV for the rutile structure and 1.80 eV for the anatase structure respectively. The occupied states are mostly O_{2p} and hybridized Ti_{3d}-O_{2p} derived orbitals have a width of



5.75 eV and 4.86 eV for respectively for rutile and anatase structures.

Figure 2.7. Density of States (DOS) for rutile and anatase, showing the narrower high occupied and lower unoccupied states for anatase. Taken from [26]

In both cases, the conduction band is mostly hybrid Ti_{3d}/4_{sp} related. The octahedral coordination causes a crystal-field splitting of the d bands, the triply degenerate t_{2g} and doubly degenerate e_g, into two sub-bands (Figure 2.6 (b)) [27]. The lower conduction bands, composed primarily of unoccupied Ti_{3d} states, have a full width of 5.8eV for the rutile structure and 5.6eV for the anatase structure [26] as it can be appreciated in Figure 2.7 and Figure 2.8.

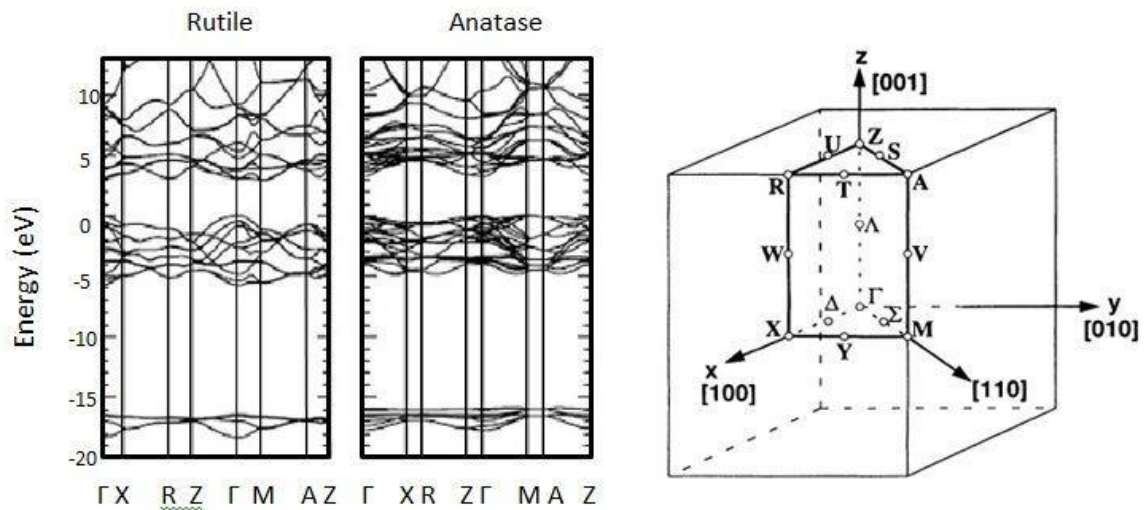


Figure 2.8. Band structure for rutile and anatase TiO₂ without doping. The minimum of the conduction band is set as 0eV. On the right, the Brillouin zone of simple tetragonal lattice for guidance. Combined from references [22] and [26].

The larger unit cell of anatase (Figure 2.3) compared to rutile (Figure 2.1) corresponds to a smaller Brillouin zone, which also favours the narrowing of the bands which in turn contributes to localization. Anatase and rutile structures host, as a result, two distinct excitonic states: self-trapped (localised) excitons in anatase and free excitons in rutile [28] [29].

2.6 Effect of Temperature, Partial Pressure and Doping on conductivity of TiO₂.

In this section the effects of temperature, partial oxygen pressure and doping on the electrical conductivity of titania are discussed. A comparison between the electronic properties of anatase and rutile will be studied and the implications in terms of transport mechanism. The information discussed becomes fundamental to support the heat treatment chosen in the present project.

2.6.1 Temperature and Doping Dependence of Electrical Conductivity.

A considerable amount of literature has been published on the electrical conductivity of titania crystals and films and its temperature dependency. Difficulties arise, however, when an attempt is made to synthesize the findings as different research groups have encountered different and sometimes opposite relationships between the variables (dopants, deposition method, etc.) which might interact with each other making the analysis difficult.

2.6.1.1 Titanium Dioxide Films Conductivity at Different Temperature Regions.

Undoped, as-deposited, reactive triode sputtering thin anatase and rutile films exhibited high resistivity when prepared under high oxygen partial pressure. Upon thermal reduction or oxidation of the films, the resistivity changed considerably, implying that it is the non-stoichiometry of the undoped films that raises the charge carrier mobility [29].

In this research, both anatase and rutile displayed thermally activated conduction as deposited films. Very interestingly, after reduction in vacuum at 400°C for two hours, the resistivity of anatase films diminished and practically became independent of temperature (Figure 2.9). Rutile on the other hand, continued to show activation energy, even when the reduction treatment was increased to 400°C and then to 450°C, behaviour showed by lines 2 and 3 in Figure 2.9. It was inferred that anatase is subjected to a metallic transition as the carrier concentration increases and reaches a certain level.

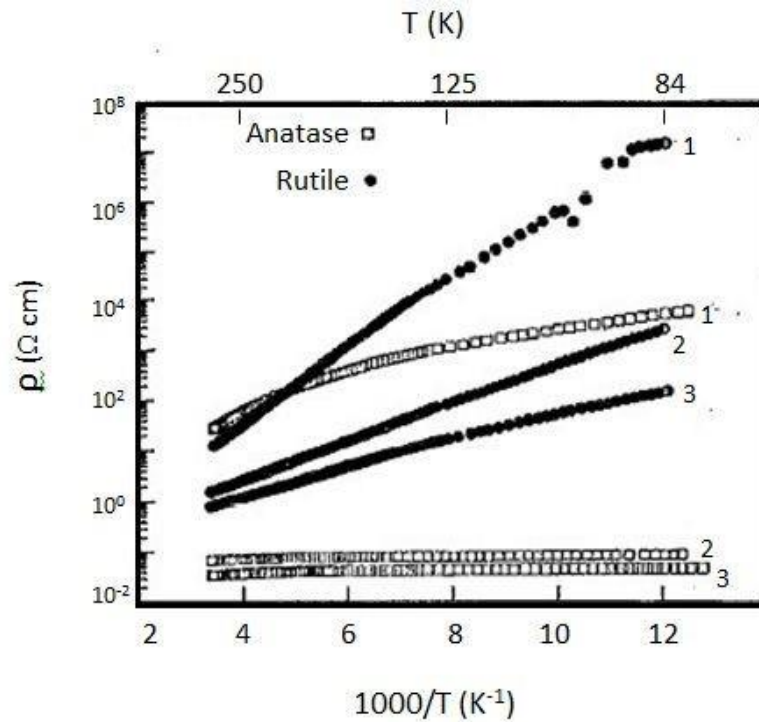


Figure 2.9. Resistivity ρ vs $1000/T$ on anatase (\square) and rutile (\bullet) films: (1) as deposited; (2) reduced at 400°C for 2h; (3) reduced at 450°C for 2h. Modified from [29].

At lower temperatures, the diminishing of electrons in the conduction band changed the dominant mechanism of conduction of the as-deposited anatase samples. The conduction band (higher mobility band) ceases to be the predominant mechanism and it is the lower mobility band (the donor band, valence band) which makes for the conduction of charges in the film. Grain-boundary changes under Hall-effect experiments have given rise to a theory that explains this phenomenon.

It was suggested [30] that trap states present at grain boundaries deplete the grain of free carriers at low carrier concentration. The higher the density of grain-boundary states in the film (more traps), the deeper the resulting donor band. Increasing the carrier concentration will reduce this depletion region to a much more localised layer at the grain boundary. As the depletion layer becomes thinner, both carrier concentration

and dopant level in anatase grains turn out to be less affected by the temperature. Approaching room temperature does not affect the concentrations and the excitation to the conduction band is still a minor effect, while the dominant conduction is in the donor band. Flat resistivity and Hall constant maximum versus temperature signposts this transition to metallic conduction mechanism [29]. In comparison, it was found that for rutile films, the conduction mechanism is influenced primarily by the excitation of electrons forming donor levels to the conduction band.

In Madare et al [31], the temperature dependencies of the electrical conductivities of DC magnetron-sputtering TiO₂ polycrystalline films on glass substrates (with water vapour as the reactive gas) were studied in the wider range 13-468K. The temperature dependency of the electrical conductivity was found to follow the form $\ln \delta = f(10^3/T)$. The general behaviour for all the samples analysed showed that for all temperatures the conductivity of anatase is higher than that of rutile.

Between 13-100K (low temperature range) as shown in Figure 2.10, the electrical conductivity of both anatase and rutile samples showed little dependency on temperature, increasing only sluggishly when the temperature reached approximately 70-80K. This result indicates that for this region, electronic transport is not activated thermally ($E_a \approx 10^{-4} - 10^{-3}$ eV), and other mechanisms come into place (hopping conduction, tunneling). Explaining by the use of mechanisms was however, out of the scope of this publication.

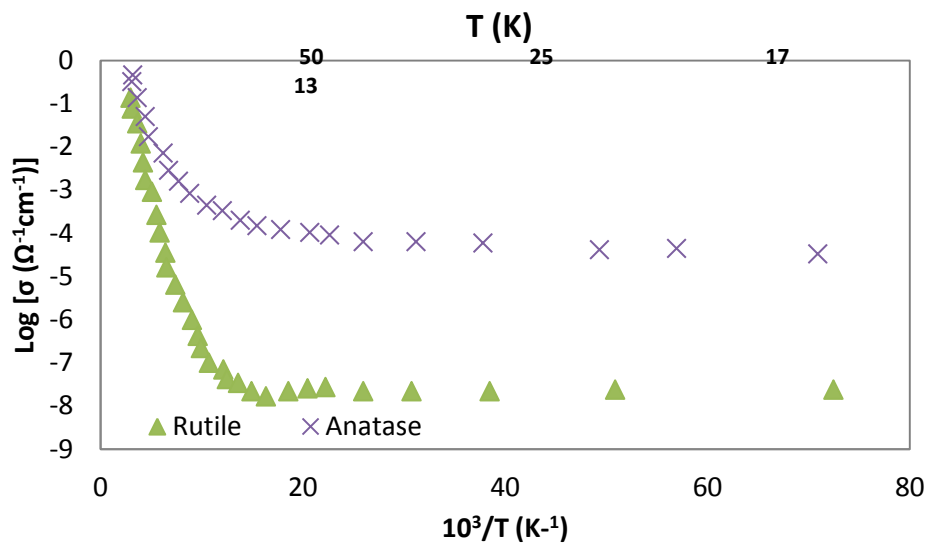


Figure 2.10. Dependences $\ln\sigma = f(10^3/T)$ plotted for anatase and rutile sputtered films, in the range 13-320K. Adjusted for easier view from reference [31].

For 310-468K temperature range, the values of thermal energy of electrical conduction obtained from the graph ranged between 0.21-0.29 eV. Figure 2.11 shows that for this higher temperature range, anatase films are more conductive than their rutile counterparts.

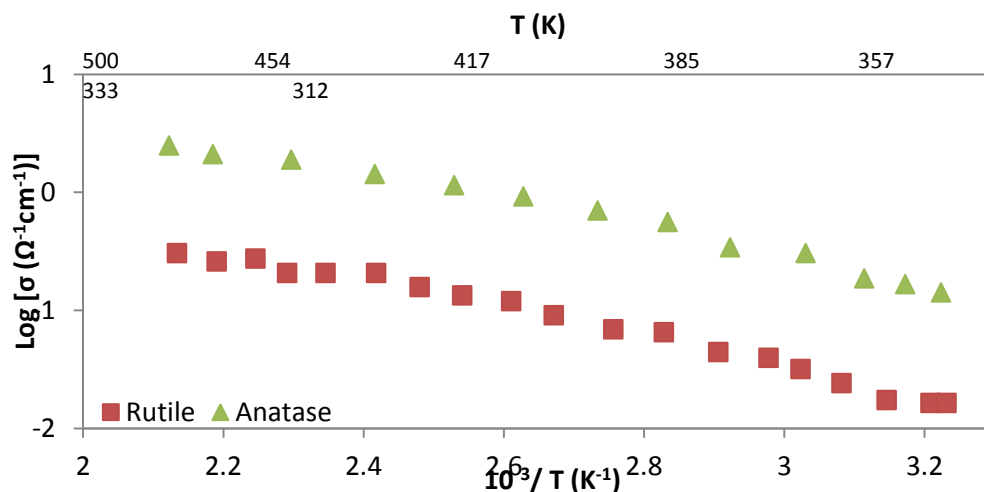


Figure 2.11. Dependences $\ln\sigma = f(10^3/T)$ in anatase and rutile films according to reference [31], in the range 310 -468 K.

In order to explain the transport mechanism models for polycrystalline titania films,

a further research [32] was conducted, in which TiO₂ films were studied during two consecutive heating/cooling cycles in the range 120K-570K. This particular research arrived to the conclusion that there are three different linear regions with different activation energies of electrical conduction. The relationship $\ln\delta = f(10^3/T)$ was once more confirmed (Figure 2.12).

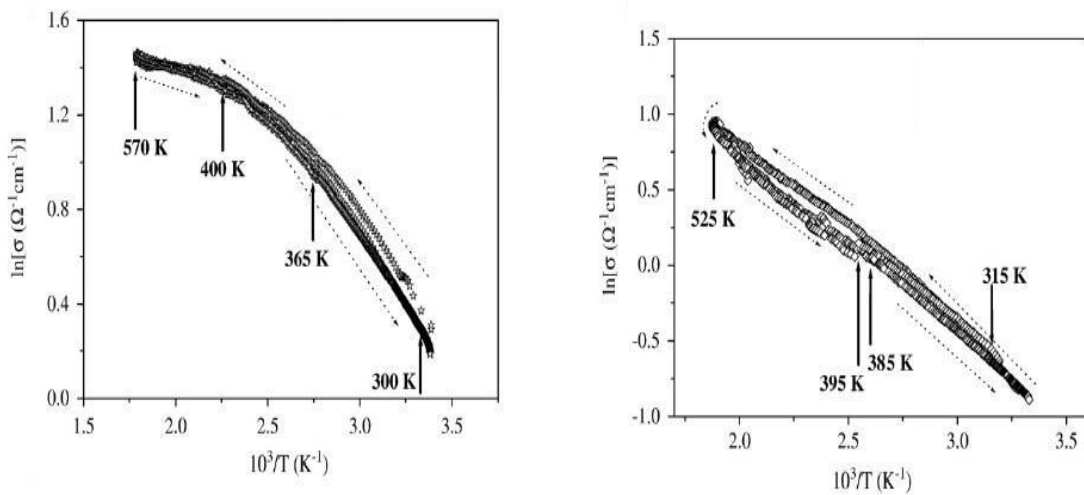


Figure 2.12. $\ln\sigma$ versus $10^3/T$ plotted for a sample: on the left, polycrystalline anatase thin film; on the right, polycrystalline rutile thin film. The dot arrows show the evolution during the heat treatment, while the solid vertical arrows mark the chosen temperature domains [32].

In the high temperature region $395\text{K} < T < 570\text{K}$, there is an observable lowering in conductivity after the first heating. Oxidation processes and phase composition changes were associated with this behaviour. After the second heating/cooling cycle was performed, it was found that the temperature-electrical conductivity relationship becomes reversible [32] strongly implying that the film reaches a stable state in structure and composition. The activation energy E_a in this region ranges from 0.047-0.073eV.

For the intermediate region ($300\text{K} < T < 390\text{K}$), a larger slope in the graphs was observed (E_a varies from 0.107eV to 0.134 eV) showing the highest dependency of

conductivity on temperature. The low temperature range ($120\text{K} < T < 290\text{K}$) exhibited the same values of E_a as the high temperature region (values of $0.046\text{-}0.082\text{eV}$). It has to be noted that this research did not include temperatures in the domain $13\text{K}\text{-}100\text{K}$ as in the previous study.

Yildiz et al. explained the resulting temperature dependent conductivity for the same type of films and linked the findings to two complementary mechanisms [33]. The data obtained fitted perfectly the Mott law ($\ln(\sigma T^{1/2})$ versus $T^{-1/4}$ is linear) for temperatures ranging from 100K to 305K (Figure 2.13). In this region, variable-range hopping (VHR) mechanism dominates the transport of the charge carriers that are mainly localised within the grains. The hopping length varies for each hop of the charge carriers from one localised state to another [34].

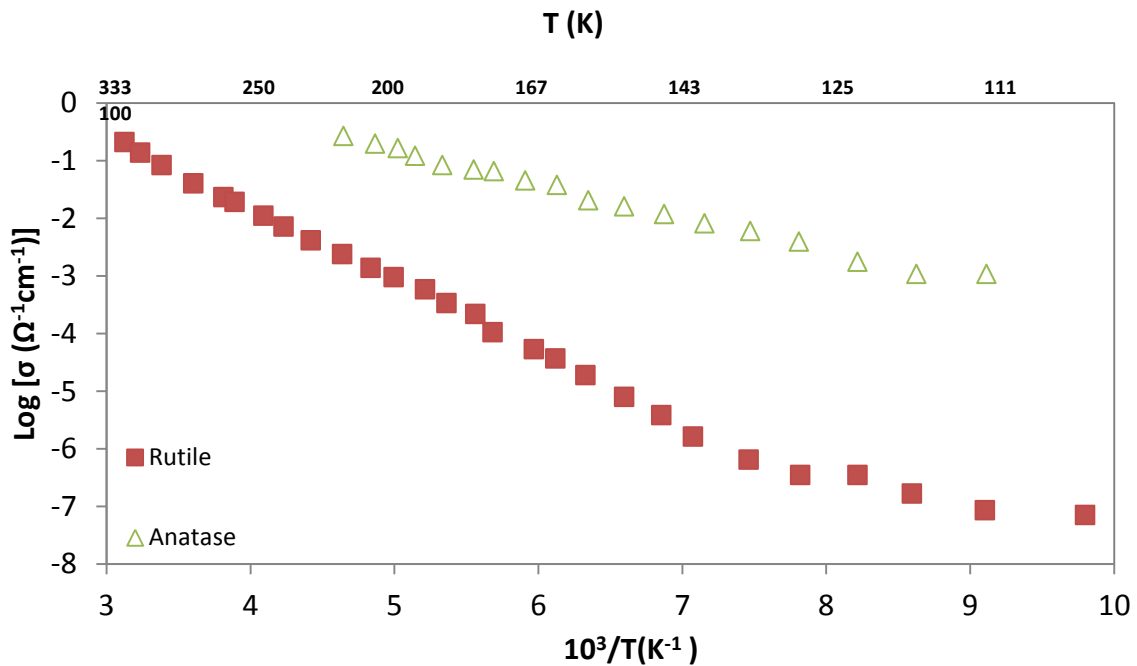


Figure 2.13. Dependences $\ln\sigma = f(10^3/T)$ plotted in the range $120\text{K}\text{-}320\text{K}$ for anatase and rutile samples. Adjusted for easier view from reference [32].

Starting from 110K there is a transition in the dependence relationship to $\ln\sigma$ that

ends approximately around $T \sim 80\text{K}$. Between 13K-60K this relationship changes to $\ln \sigma$ being proportional to $T^{-1/2}$. The mechanism corresponding to the observed behaviour is the same VHR mechanism with the inclusion of Coulomb repulsion between carriers (long range Coulomb interactions) that result in different hopping processes [33].

The electrical resistance and dielectric loss of anatase and rutile films prepared by the chemical vapour deposition (CVD) on Si substratum was studied in the temperature range 290K - 1100K a controlled Ar/O₂ atmosphere ($10^{-7} \leq p(\text{Ar/O}_2) \leq 10^{-3} \text{Pa}$). This suggested that under these circumstances the conductivity of TiO₂ is n-type (ionic contribution becomes negligible for $p(\text{O}_2)$ lower than 10^{-2}Pa [35]). The controlled atmosphere affects the oxygen vacancies of the thin films. Both AC ($f=200\text{Hz}$, 1kHz and 10kHz) and DC measurements gave the same result: in anatase films, the resistivity diminishes as the temperature increases; while in rutile films, the decrement in resistivity is less pronounced and remains relatively constant between 450K-1000K, as shown in Figure 2.14.

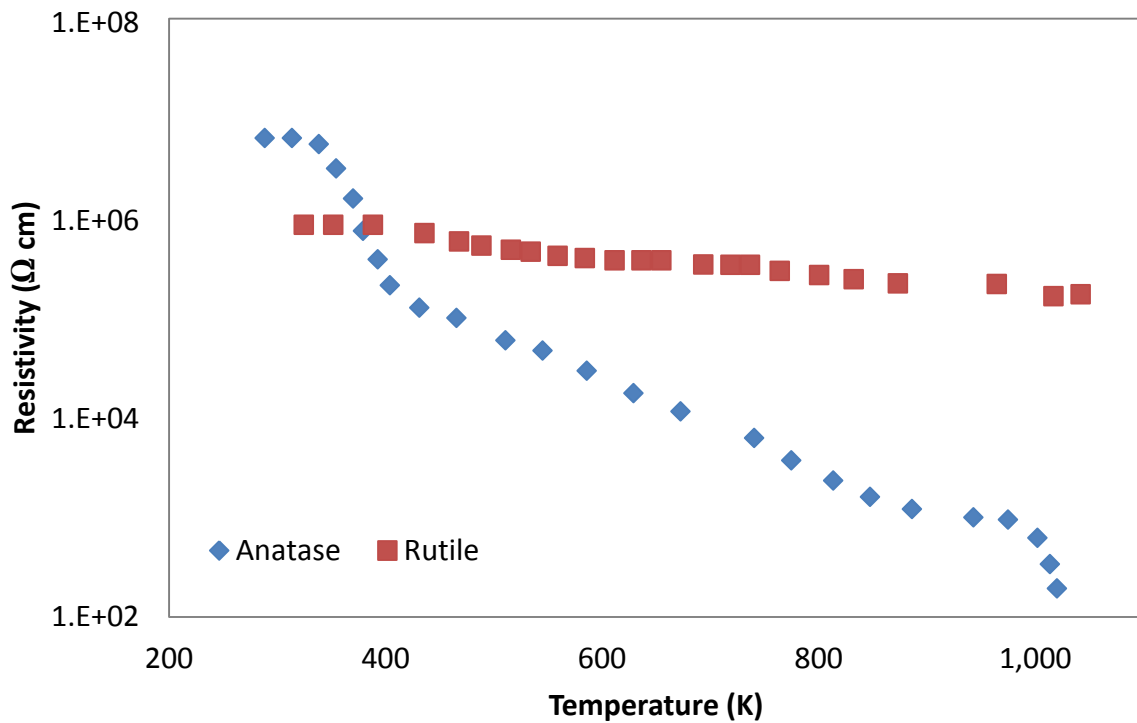


Figure 2.14. Temperature dependence of the electrical resistivity of rutile and anatase TiO₂ sample in vacuum. From reference [35].

When adding these differences together it could be argued that there are four main temperature regions for electrical conductivity in titania films.

2.6.1.2 Titanium Dioxide crystals

Cronemeyer [36], studied the conductivity-temperature behaviour in rutile single crystals (prepared by the boule technique) using the four-terminal method, in two crystallographic directions: parallel and perpendicular to the crystal c-axis. Although for both orientations a linear fit was obtained (cooling down from a starting temperature of 1400°C), no definite answer was provided as to when the direction is perpendicular to the c-axis, conductivity was still predominantly linear (inversely proportional to 10³/K) down to 350°C (Figure 2.15), while for the direction parallel to c axis, this line-

arity came to an end at 550°C (Figure 2.16).

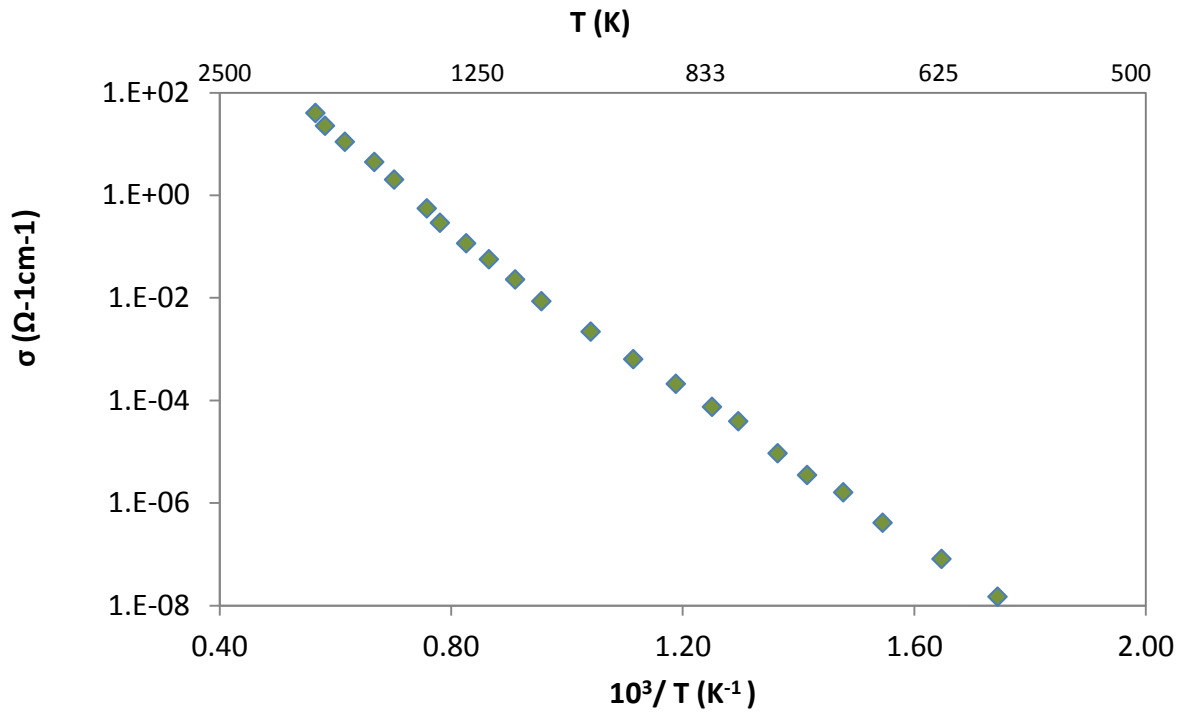


Figure 2.15. High temperature conductivity plot for rutile TiO₂ crystals perpendicular to c axis [36].

A similar study (comparing the direction of the electronic flow) for anatase crystal was not found in the literature research performed.

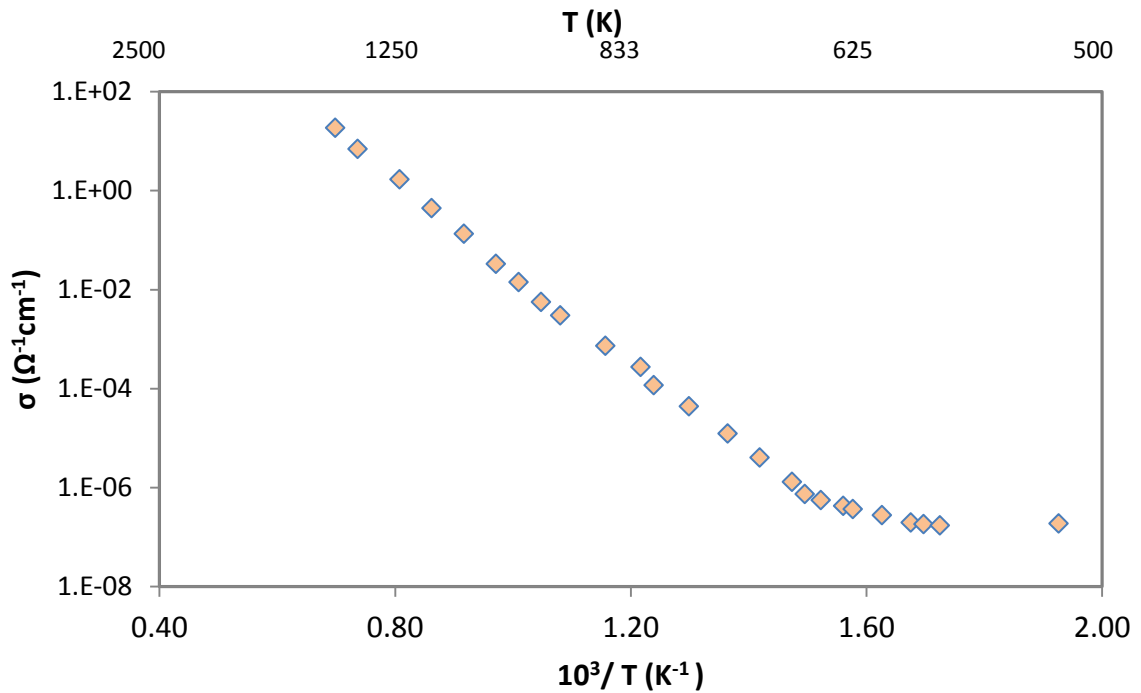


Figure 2.16. High temperature conductivity plot for rutile TiO₂ parallel to c axis [36].

For high temperatures (>500°C) conductivity agreed to an intrinsic conduction mechanism as data fit the equation:

$$\delta = \delta_0 e^{((-E_G)/2kT)} \quad (2.1)$$

Where δ is the carrier concentration, E_G is the band gap, k is the Boltzmann constant ($1.3806488 \times 10^{-23} \text{ m}^2 \text{ kg s}^{-2} \text{ K}^{-1}$), $\delta_0 = n_0 e b$; $n_0 = 1.127 \times 10^{29} / \text{m}^3$, (valence electrons per m^3); $b = 0.1 - 10 \text{ cm}^2 / \text{v-sec}$ (carrier mobility).

In comparable research, after synthesizing chemical transport reaction anatase single crystals, Forro et al. [37] analysed two different temperature dependent resistivity regions. Below 50-70K (low temperature region) resistivity moves downwardly as the temperature increases (Figure 2.17). While the increment in temperature brings about the fall of carrier mobility in the conduction band, it also causes more electrons to be excited to the conduction band. Out of these two phenomena, opposed in terms of

promoting the conductivity, it is the increase in electrons excited from the valence region that predominates.

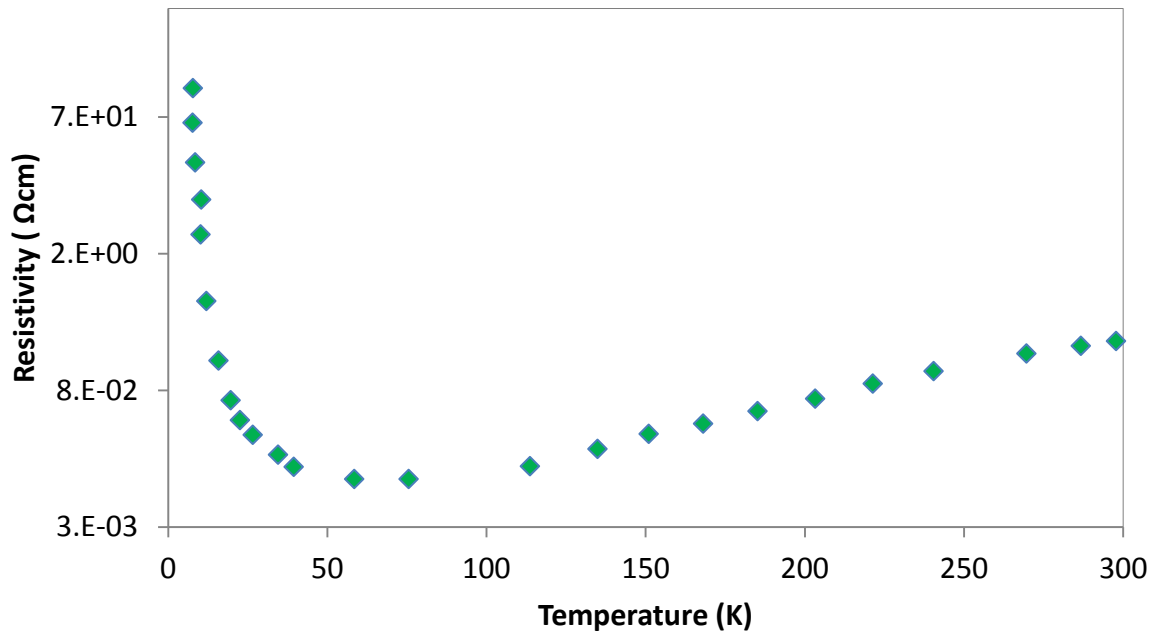


Figure 2.17. Temperature dependence of the resistivity of an as-grown anatase single crystal [37].

Above 50-70K, the system enters into the exhaustion regime (the saturation of the carrier concentration) and the mobility of conductive electrons is lessened. There is a constant increment in resistivity as the temperature is risen as a result.

The manner in which the Hall coefficient, Hall mobility, carrier density and thermoelectric power of the single anatase crystals behaved with temperature changes revealed different features: Hall coefficient decreases with increasing temperature, while the density of conducting carriers rises constantly to a maximum. In addition to that, the thermoelectric power decreases negatively as the temperature increased reflecting low carrier semiconductor behaviour. Additionally, it was found that the temperature dependence of the thermoelectric power in anatase crystals has a resem-

blance to those of the exhaustion regime of conventional semiconductors with ambulant charge carriers.

On the other hand, carrier mobility above 50K falls sharply with an increase of temperature, at $T > 160\text{K}$ the rate at which the carrier mobility dwindles down in a proportional fashion ($\sim \exp^{(T_0/T)}$, T_0 around 850K). This result in mobility was believed to be because of optical phonons induced scattering of the electrons.

Similar results were obtained for TiO₂ films on silicon wafers prepared by sol-gel spray pyrolysis technique [38]. The conductivity activation Energy E_a was 101meV for anatase films and 63meV for rutile films as shown in Figure 2.18.

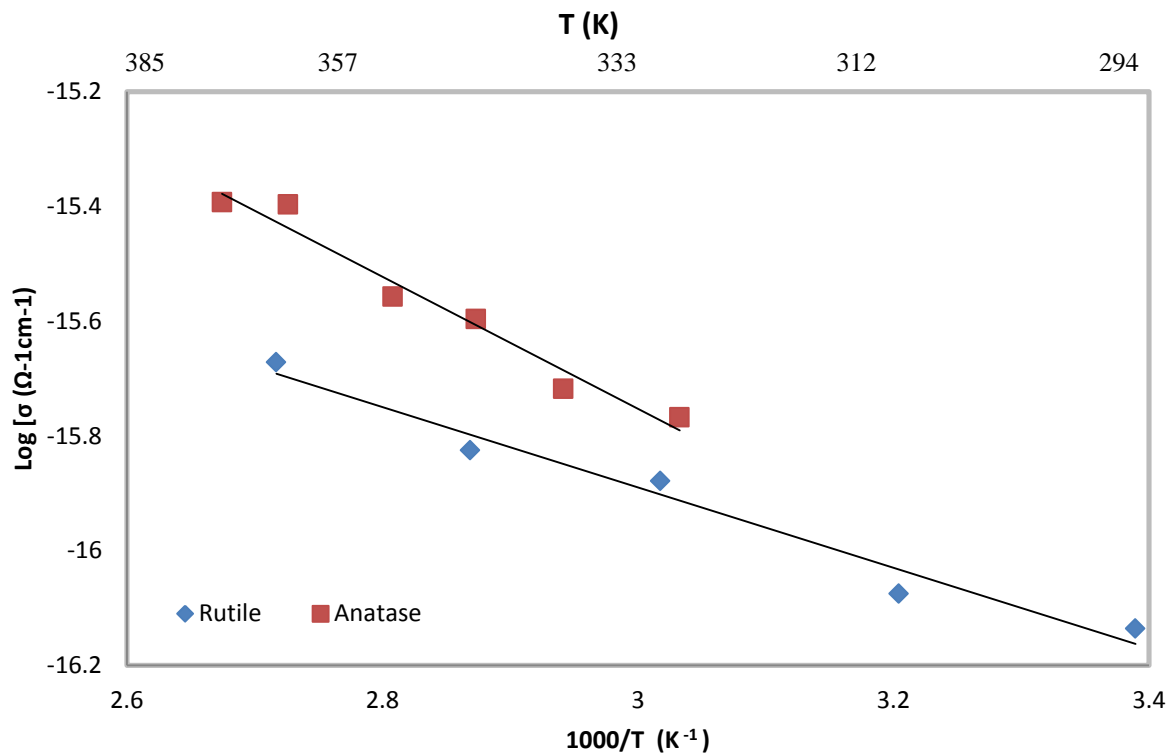


Figure 2.18. Temperature dependent conductivity of TiO₂ as a plot of $\ln\sigma$ vs. T . The thermal activation energy of conductivity is obtained from slope of straight the line [38].

2.6.2 Effect of Doping on electrical conductivity of titania

Earle M. D. [39], was one of the pioneers in studying the conductivity of titanium dioxide. His description of the relationship of oxygen partial pressure and electric conductivity is denoted by the equation:

$$\sigma = kP_0^{(-1/n)} \quad (2.2)$$

Where σ is conductivity; P_0 is oxygen partial pressure and k and n are temperature dependent parameters. When heated, titanium dioxide is deprived of oxygen atoms (the electronegative element) from its surface, leaving plenty of the electropositive element (Ti) atoms occupying interstitial positions. The electrons of these interstitial Ti atoms are more easily removed thermally into an allowed region for conduction [39]. This behaviour is presented in Figure 2.19

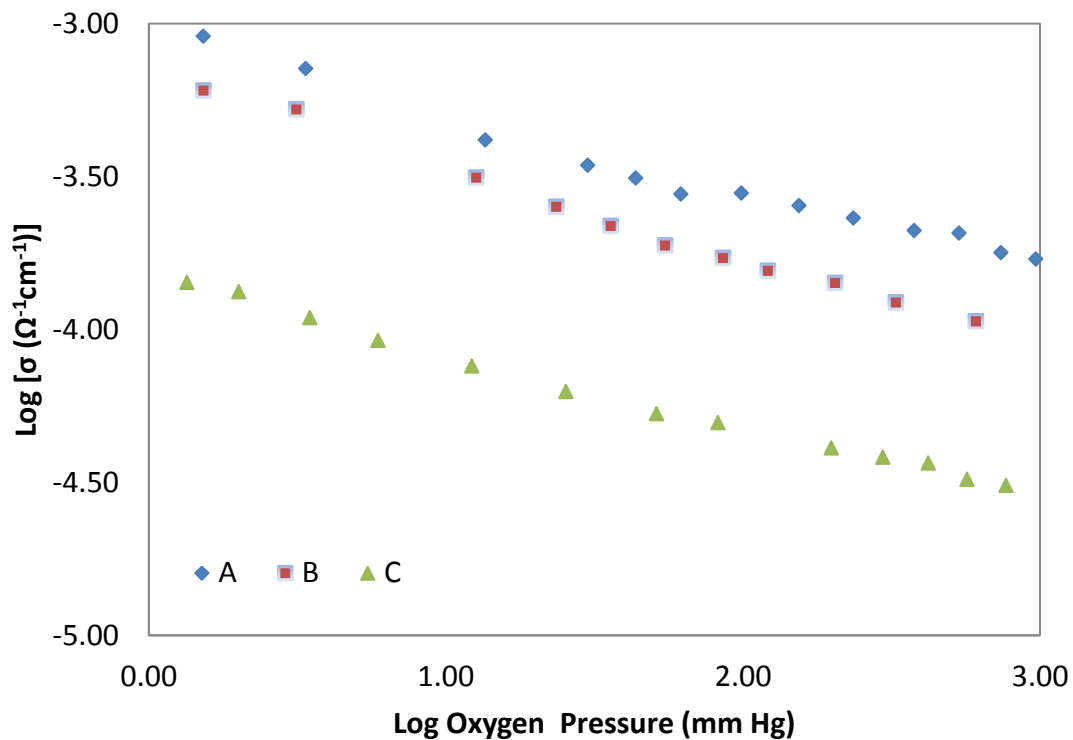


Figure 2.19. Conductivity as a function of oxygen pressure. A - rutile, 968°C; B- rutile, 820°C; C- anatase, 861°C [39].

Grant [40] introduced the term ‘reduced rutile’ to signify that an effort has been made to introduce oxygen vacancies in the specimen by heating in oxygen at reduced pressure, or in an atmosphere of any reducing gas. The same concept can be applied to anatase. The influence on electrical conductivity of oxygen pressure was associated with departures from stoichiometry.

To finalise providing the necessary background for the present research project, it is important to dedicate the rest of this chapter to the theoretical and empirical aspects of the chemical solutions prepared with titanium compounds that are employed in the preparation of the films. To be able to understand its importance in this research an introduction to cathodic electrodeposition of titania is required.

2.7 Cathodic electrodeposition of TiO₂ films.

Cathodic electrodeposition of TiO₂ films has been investigated as an efficient alternative for the preparation of Dye Sensitized Solar Cells (DSSCs). The main route for the synthesis of such films is the hydrolysis of Ti peroxo complexes by electrogenerated base to form Titanium hydroxide deposits on cathodic substrates.

Zhitomirsky et al. have performed cathodic electrosynthesis from commercial TiCl₄ solutions [41-44] on Pt substrates at 1°C. They used different solvents in their solutions such as N,N-dimethylformamide (DMF) and Methyl alcohol-water as well as H₂O₂ to form the peroxo complex. Park, van de Kagenaat and Frank used the electro deposition precipitate (from the hydrolysis of TiCl₄) to prepare a colloid solution in Ethylene Glycol to yield a slurry that was used to cover, via a doctor blade, transparent electrical conducting SnO₂ coated glass substrate [45]. Wessels, Feldhoff, Wark, Rathousky and Oekerman performed the electrodeposition from TiCl₄ route under a N₂

atmosphere, adjusting to a pH of 2.5 with Na₂CO₃ and Sodium Docecyl Sulphate on FTO glass [46]. Gao et al used metatitanic acid (H₂TiO₃) as a precursor, adjusting the pH to 2.4 with HNO₃ [47].

The other main precursor for the Cathodic electrolysis of TiO₂ films is TiOSO₄ (titanyl sulphate). Originally, Natarajan and Nogami [48] dissolved Ti powder in H₂O₂ to form a gel that was subsequently dissolved in H₂SO₄ to obtain the electro bath. The result of the deposition was the formation of titanium oxhydroxide gel on the surface of Indium-tin-oxide coated glass (Cathodic substrate). Karuppuchamy [49-54] et al. used TiOSO₄ powder as a starting point, simplifying the preparation of the bath. Their Cathodic electrodeposition was carried out at constant temperature (283K) under similar conditions as used by Natarajan et al.

A further point to be considered is therefore, the chemistry of the precursor solution for the electrodeposition carried out in this research (peroxo complexes of titanium).

2.8 Peroxo Complexes of Titanium

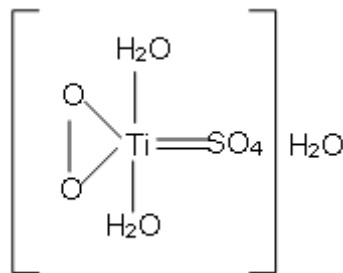
For many years, different researchers have tried to decipher the nature of the peroxo-complexes of titanium. The origin of the intense orange colour obtained on mixing H₂O₂ with an acidic solution of Ti(IV) has been suggested as being due to the presence of various compounds.

Jahr and Gastinger [55] proposed that the colour of the compound was due to the peroxy titanyl cation [TiO₂]⁺². Schwarz [56] considered that the colour originated from the peroxo-disulphato titanate anion [O₂Ti(SO₄)₂]²⁻.

Schaeppi and Treadwell [57] suggested that the colour be attributed to either O₂TiSO₄ or [O₂Ti(SO₄)₂]²⁻. Babko and Volkova [58] concluded that the coloured com-

plex ion is $[\text{Ti}(\text{H}_2\text{O}_2)]^{4+}$. Furthermore, Mori, Shibata, Kyuno and Ito [59] attributed the coloured species to $[\text{TiO}_2 \text{ aq.}]^{2+}$ or $[\text{Ti}(\text{OH})_2(\text{H}_2\text{O})(\text{H}_2\text{O}_2)]^{2+}$.

Patel and Mohan [60] prepared a solution of peroxy titanium sulphate in excess of hydrogen peroxide. The solution was evaporated and the dried obtaining a red-coloured solid peroxy complex $\text{TiO}_2\text{SO}_4 \cdot 3\text{H}_2\text{O}$. They assigned the following chemical structure to the compound:



Cai, Itoh and Sun studied the effect of pH on the optical properties of peroxo-titanium complex [61]. They developed a stable PTC (peroxo-titanium complex) by mixing H_2O_2 with titanium hydroxide. Colour changes with respect to pH values over a wide range were investigated: the pH value for the freshly prepared PTC was 2,21. Table 2.4 shows the relationship between pH value and colour.

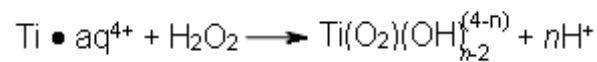
Table 2.4 Dependency of colour and transparency of a peroxo titanium complex solution with its pH. Taken from [61]

pH	Colour	Transparency
0.65	Dark Red	Translucent
0.99	Red Orange	Translucent
2.21	Orange	Transparent
3.90	Light Orange	Transparent
5.80	Yellow	Cloudy

6.70	Pale Yellow	Translucent
8.37	Pale Yellow	Translucent
10.77	Pale Yellow	Translucent

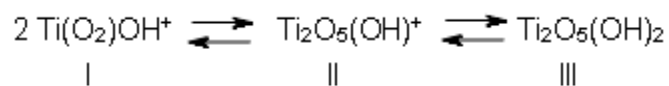
There is an inconvenient limitation in this research, however, as both the online and hard copy of the paper is in black and white and the colours cannot be appreciated. It was concluded, nonetheless, that the $Ti(O_2)(OH)_{n-2}^{(4-n)+}$ model is most adequate to represent the colour forming species in this type of chemical system.

Mühlebach, Müller and Schwarze determined the number of hydrogen ions n which are liberated in the process of mixing $TiCl_4$ and concentrated H_2O_2 at $pH < 1$ and suggested the following reaction [62]:

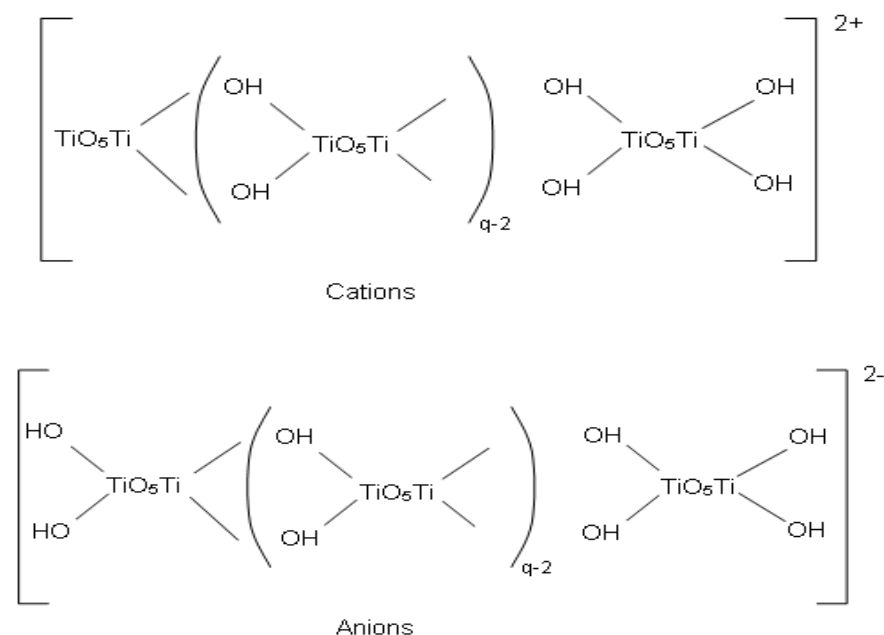


It was found that for very acidic solutions $n=3$, assuming a mononuclear complex $Ti(O_2)OH^+$

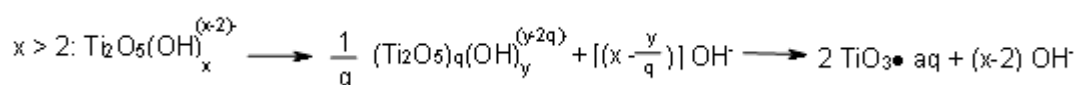
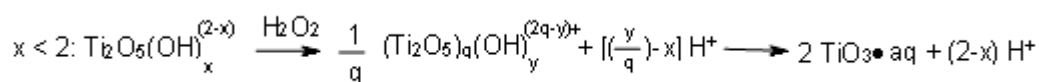
Between $1 < pH < 3$ n increases suggesting deprotonation accompanied by a colour change and condensation from mononuclear TiO_2OH^+ to dinuclear species according to:



Above $pH 3$, it was assumed that $Ti_2O_5(OH)_2$ would condense by forming μ -hydroxy bridges between Ti atoms as shown by:

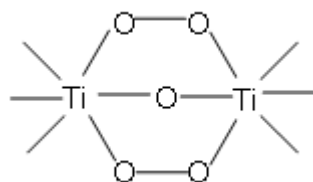


Generalising, the processes are formulated:



Below pH3, x is smaller than 2 and the complexes are either cations or uncharged $\text{Ti}_2\text{O}_5(\text{OH})_2$. Above pH3, x is larger than 2 and the condensing species are anions of $\text{TiO}_5(\text{OH})_2$.

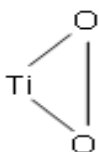
The groups $(\text{Ti}_2\text{O}_5) \cdot \text{aq}^{2+}$ or $\text{Ti}_2(\text{O}_2)_2 \cdot \text{aq}^{2+}$ were concluded to be two-five-membered chelate rings which are formed in the chemistry of chelates [62]:



The Ti Atoms are bonded by a single μ -oxygen bridge and the two μ -peroxy groups that occupy only one coordination site. The colour of the peroxotitanium complex is due to an electron transfer from the ligand O_2^{2-} to the metal cation. It has to be men-

tioned that the structure postulated by Mühlebach, Müller and Schwarzen requires the grouping Ti-O-O-Ti to be planar which suggest that Ti₂O₅·aq⁺² ion might be a superoxy rather than a peroxy group.

From peroxides of other transition metals, Schwarzenbach suggested another possible configuration for the titanium peroxy complexes [62]:



Schwarzenbach based his hypothesis in the rings of other peroxides of different transition metals. It was supported by XRD analysis of C₁₄H₁₆N₂O₁₈K₂Ti₂ crystals where the next configuration of the complex was reported (Figure 2.20):

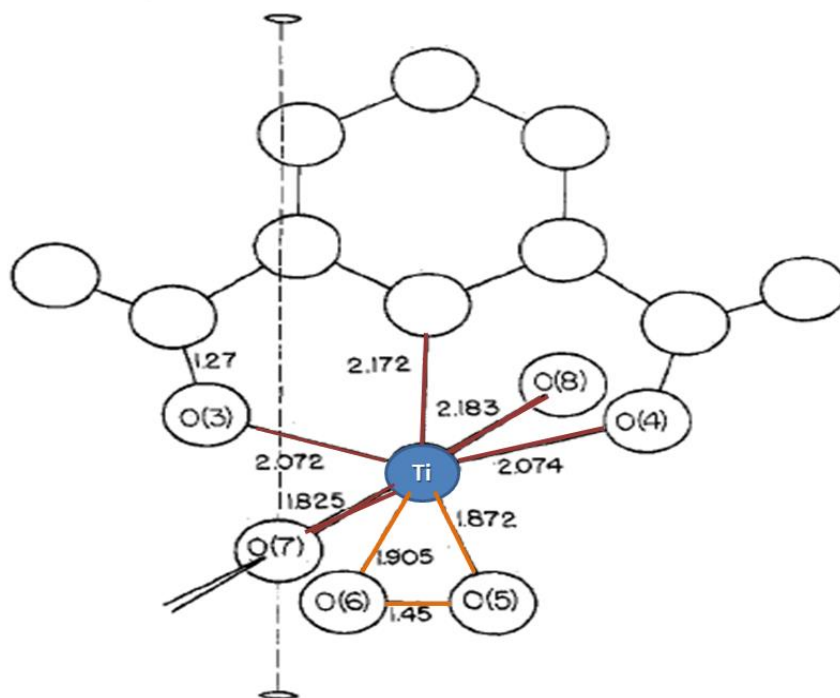
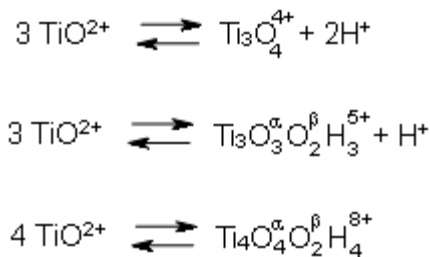


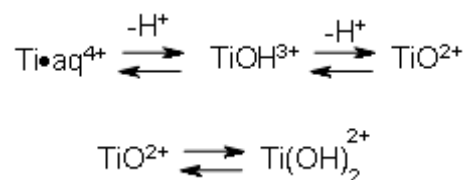
Figure 2.20. Configuration of the titanium complex C₁₄H₁₆N₂O₁₈K₂Ti₂. The distances of the bonds are given in Å. Only bonds surrounding the Ti atom are detailed. From reference [62].

It can be perceived that the peroxy group is laterally coordinated to the metal leading to a distorted pentagonal arrangement with the dumbbell in the plane of the pentagon. The bonding was described as arising from two different possibilities: first, the donation of electrons to the metal ion from the δ bonding and the δ^* antibonding orbitals of the peroxy group. The second alternative presented is that the peroxy group might be bound by two δ bonds to the titanium.

In a complementary work, Comba and Merbach [63], studied quantitative and qualitative compositions of acidic aqueous solutions of dilute hydrolyzed Ti(IV). They established the presence of oligomers (up to five of them) in the solution. They presented a model consisting of two trimers and one tetramer in equilibrium with the titanyl ion:



The research concluded that other monomeric species were present in equilibrium with monomeric titanyl which were most probably $\text{Ti}(\text{OH})_2^{2+}$ and $\text{Ti}^{4+}(\text{aq})$:



Likewise, Gatehouse and, Platts and Williams [64], determined the structure of single-crystal anhydrous titanyl sulphate, TiOSO_4 and titanyl sulphate monohydrate,

TiOSO₄•H₂O via high resolution electron microscopy. The structure consist of [TiO]_n²ⁿ⁺ chains parallel to the crystallographic b axis linked by sulphate tetrahedra to form the arrangement (Figure 2.21). This work illustrates the structural relationship between the S atom and the Ti atom.

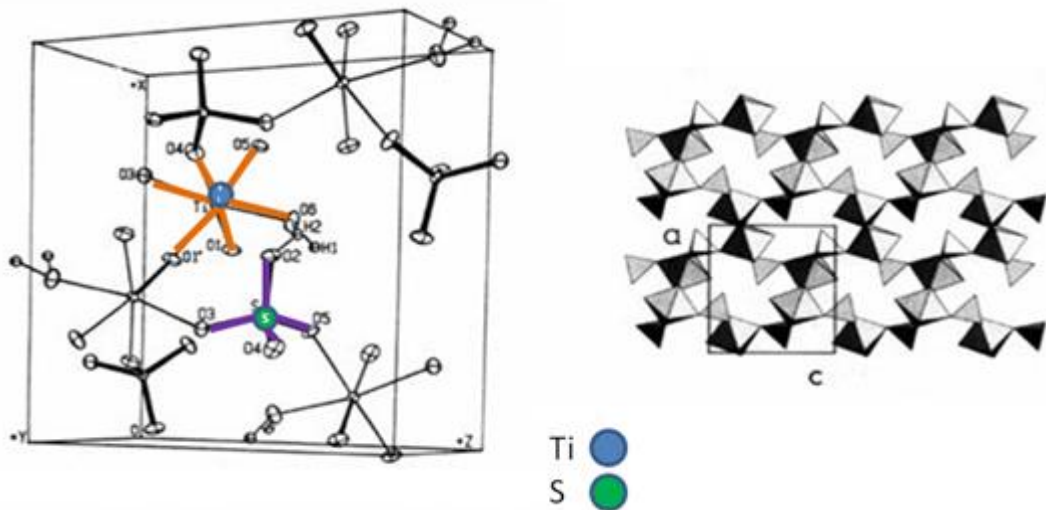


Figure 2.21. On the left: Tinanyl sulphate hydrate structure; on the right: structure of tinanyl sulphate monohydrate viewed along (010). Modified for easier view from reference [64]

The three oxygen atoms from the sulphate ion are bonded to titanium and the fourth atom bonds to the water molecule (left hand side, Figure 2.21). The array of corner-shared octahedra and tetrahedra are shown on the left of Figure 2.21

In order to extend the review to polynuclear Ti structures, it is relevant to describe the work of Sergienko [65]. This research studied the structural characteristics of different peroxy complexes of titanium. His study compared the compounds according to the ratio of titanium atoms to O₂. It was found that titanium forms mono, bi and tetra nuclear peroxy complexes for a ratio Ti:O₂ = 1:1. Mononuclear complexes form a pseudooctahedral coordination structure as seen in Figure 2.22.

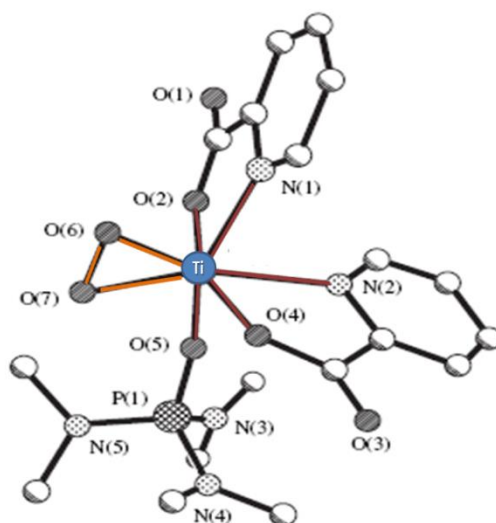


Figure 2.22. Structure of pseudooctahedral mononuclear peroxo complexes of titanium: [Ti (O₂) (Pic)₂(HMPT)]. From reference [65].

It can be seen that the Ti atom is coordinated with the O₂ ligand as well as four O atoms and two more atoms, N(1) and N(2) in Figure 2.23.

On binuclear peroxo complexes of Titanium (IV), the Ti atoms are connected by the bridging oxo ligand on the two fold axis (Figure 2.24). They are also bonded to 3 more O atoms and one more atom, N(4).

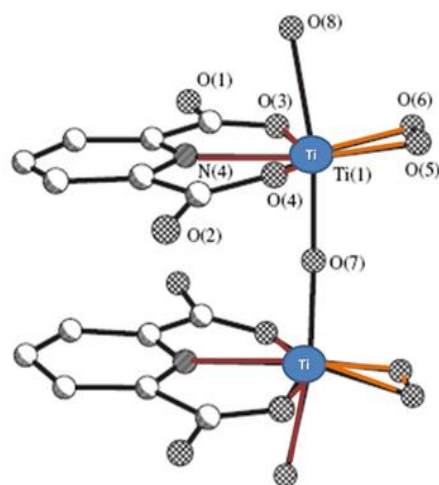


Figure 2.23. Structure of pseudooctahedral binuclear peroxo complexes of titanium: [{Ti (O₂)(Dipic)(H₂O)}₂(μ-O)]²⁻ [65].

The structure of a tetranuclear Ti Peroxo complex is pseudo octahedral. Two binuclear fragments are linked by chelating-bridging carboxylate O(6)-C-O(7) groups of two symmetrically bonded anions of the citric acid (CH₂)₂(COOH)₃(COH)) in the compound (NH₄)₈[Ti(O₂)₄·(C₆H₄O₇)₄]·8H₂O (Figure 2.24).

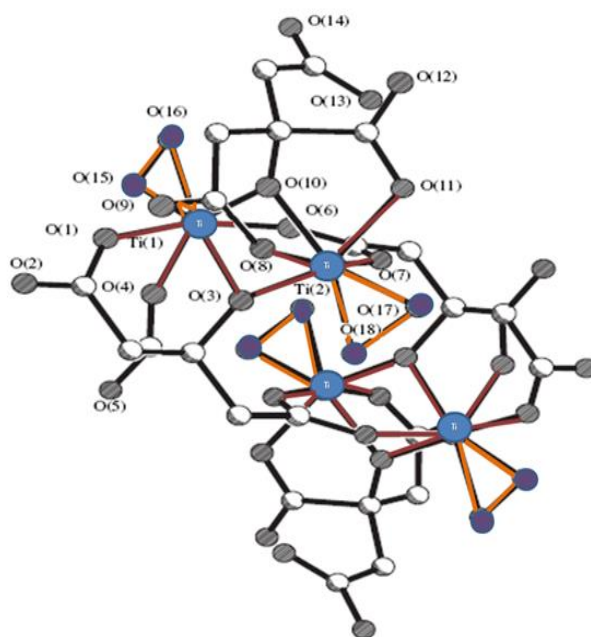


Figure 2.24. Structure of a tetranuclear peroxo complex of titanium: $[\{\text{Ti}(\text{O}_2)(\mu\text{-Cit})\}_4]^{8-}$ [65].

One COO group (out of six) coordinates the Ti(1) and Ti(2) atom with O(6) and O(7) respectively, becoming the chelating-bridging group. One COO group (out of six) coordinates the Ti(1) and Ti(2) atom with O(6) and O(7) respectively, becoming the chelating-bridging group.

It can be argued that despite all the different research approaches, it has proved difficult to generalise the configuration of the complexes caused by titanyl ions in a peroxo solution. A mixture of some or many of the species discussed above (or different ones) might be present at some point during the preparation of the films.

Chapter Three

Experimental Methodology

3.1 Introduction

The experimental procedure presented in this chapter is separated into three parts: The first part of the chapter presents the exploratory experiments carried out in order to check and optimise the potential to be used during the deposition. The electrochemical deposition and film preparation performed are described in the second part of the chapter. The methods and instruments employed in the subsequent characterisation of the films are discussed in the final section of the chapter. Both, important parameters and key variables are provided in either section.

Having established the lack of simplicity due to the different possible structures that peroxo complexes of titanium can form in aqueous solution (chapter 2), it was decided that changing one variable while keeping constant the others was the best methodology to proceed with the study. The temperature of the electrolytic bath (peroxo complex of titanium) is the variable to be changed in a specific range while keeping constant the others (as defined in the research question in chapter one).

3.2 Substrate Preparation

As mentioned in the previous chapter (section 2.7), a cathodic substrate is required for the electrochemical process to take place. Two similar type of Tin Oxide glass are commercially available: Indium Tin Oxide coated glass (ITO) and Fluorine doped Tin Oxide coated glass (FTO). Exhibiting both similar transmissions in the visible region, it was decided to prefer ITO due to its lower sheet resistance (11.7Ω versus 18.6Ω of FTO). ITO glass slides were purchased from Sigma Aldrich Chemicals Ltd. The dimensions of the slides were 10mm x 10mm and thickness of 0.5mm.

It can be argued that both, structure and properties of thin films could be affected by the quality of the substrate used. A rough and unclean surface will affect the homogeneity and uniformity of the deposited film. Any dirt will accidentally increment the chance of crack formation and will considerably affect the quality of the film. A spotless surface will also increase the adherence of the film.

Prior to the deposition, the ITO substrates were ultrasonically cleaned in deionized water, 2-propanol and acetone for 15 min in each solvent. The substrates were dried in air and kept in sealed Petri dishes to reduce the risk of contamination before the deposition.

3.3 Safety Considerations

The chemicals used for the solution preparation can be hazardous if they are in direct contact with the skin or if they are inhaled. Therefore, the solution preparation

procedure was conducted under a fume cupboard and appropriate protective clothing such as gloves, lab coat, mask and safety goggles were worn.

3.4 Preparation of the Peroxo titanium complex

The components used for the formation of the final electrochemical solution were as follows: Titanium Sulphate (TiOSO₄) (15wt% solution in dilute sulphuric acid), Hydrogen Peroxide (H₂O₂) (50wt% solution in water), Ammonium Nitrate (NH₄NO₃) (98+%) (all from Sigma Aldrich Chemicals Ltd, UK) were used to prepare the solution.

The preparation of the bath was performed as follows: Hydrogen Peroxide was added to the TiOSO₄ solution under stirring (250rpm), forming a red transparent solution. The NH₄NO₃ was added immediately and the volume was completed with distilled and deionised water to 200ml. The final composition of the bath is: 2.10wt% TiOSO₄, 0.020wt% H₂O₂ and 0.80wt% NH₄NO₃. The solution was prepared and used fresh, just before the electrodeposition. The composition of the bath was chosen based on previous studies [51-54]. The composition is such that the pH of the solution is acidic (~1) and it maintains the stability of the lower oxidation state of the metal, allowing the higher oxidation state to precipitate the oxide or hydroxide under the application of potential.

Before describing the electrodeposition method it is important to mention that two preliminary exploratory experiments were conducted in order to define the variables such as pH and cathodic deposition potential.

3.5 Exploratory experiments

3.5.1 Temperature vs pH of the Electrolytic Bath

The first exploratory test carried out consisted of heating up the electrolytic solution while measuring the change in pH and observing any change in the appearance of the solution. The objective of this test was to evaluate any variation of pH while changing the temperature of the bath. It was performed under controlled heating rate (1°C/min) while measuring the pH of the solution and taking pictures to monitor changes in solution coloration.

The second exploratory test was implemented in order to optimise the cathodic potential of deposition through cyclic voltammetry.

3.5.2 Cyclic Voltammetry

For this study, Cyclic voltammetry was used to explore the electrochemical system where the film deposition was taking place. Cyclic voltammetry is a potentiodynamic electrochemical method used to locate redox potentials of electroactive species in a solution. As the preparation method in this project involves an electrochemical bath, cyclic voltammetry (CV) becomes a useful tool for analyzing the chemical transformations that can occur in the substrate - solution interface.

In this method, a potential is swept from an original voltage (V1) to a second voltage (V2) at a fixed rate [66]. While the voltage is measured between the reference and the working electrodes; current is recorded between the working and the counter elec-

trodes in a three electrode cell. When the voltage reaches V₂ the sweep is reversed back to the original voltage V₁ (the switching potentials) as showed in Figure 3.1.

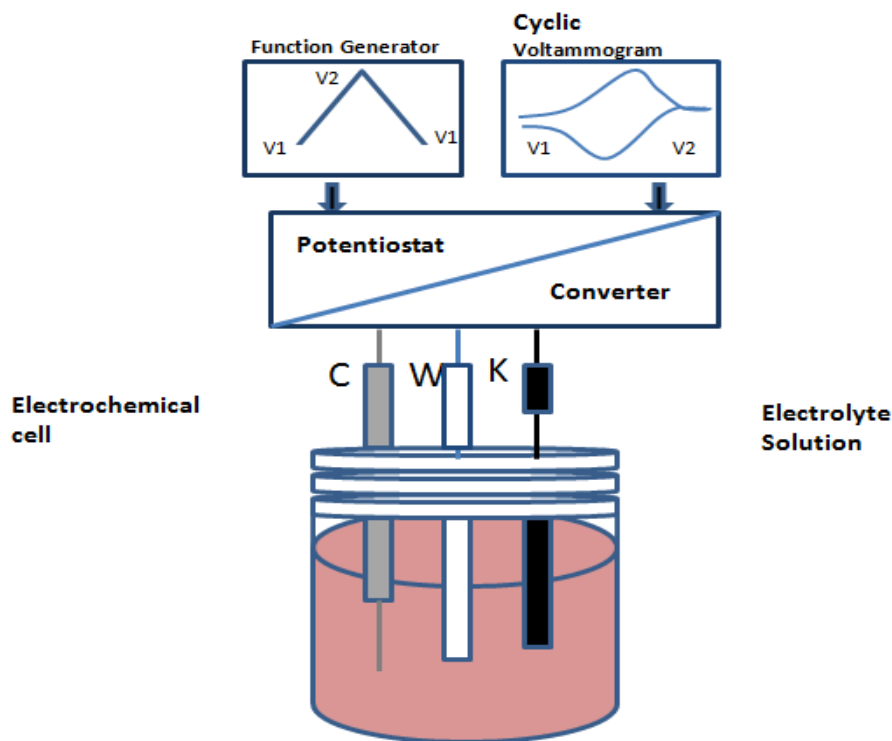


Figure 3.1. Schematic representation of cyclic voltammetry.

The data collected is plotted as potential E, between the reference electrode (K) and the working electrode, versus the current response I, between the work electrode (W) and the counter electrode (C). In forward scan (from V₁ to V₂) the current increases as voltage is swept, the equilibrium position of the electrochemical shifts as a result of the presence of analytes that can be reduced. A peak in current occurs as at a point where the diffusion layer grows sufficiently on the surface of the working electrode so that the flux of reactant to the electrode is not fast enough to satisfy the equilibrium as established by Nernst equation [67]:

$$E = E^0 - \frac{RT}{nF} \ln Q \quad (3.1)$$

E is the potential of the cell to the standard potential (E^0). n is the number of moles of electrons transferred in the cell reaction or half-reaction. Q is the reaction quotient. R is the universal gas constant: $R = 8.314\ 472(15)\ \text{J K}^{-1}\ \text{mol}^{-1}$. T is the absolute temperature in K. F is the Faraday constant, the number of coulombs per mole of electrons: $F = 9.648\ 533\ 99(24) \times 10^4\ \text{C mol}^{-1}$.

This equation relates the useful work that the electrochemical bath can produce, to the (E^0) of the system and to the free energies of the conversion of the reactants into products (the term $[RT]/nF \ln Q$). During the reverse scan (from V_2 to V_1) the current goes from the solution to the working electrode and there will be peaks in current as analytes that can be oxidised are present in the solution.

In this research, cyclic voltammetry is relevant for obtaining the optimum potential value at which the titanium ions are deposited on the electrode (ITO glass). The charge of the ions will vary according to the voltage present. Locating the optimum potential and keeping it constant during the process, will ensure that there is a continuous deposition of material on the substrate.

3.6 Film electrodeposition.

Electrosynthesis is an important technique among solid-state manufacturing methods. It is founded on the induction of diffusion of charged species by the application of an electric potential. This electrochemical process is then utilized to deposit a material onto an electrode.

The deposition achieved by passing an electric current between two electrodes (working and reference) separated by an electrolyte. Synthesis of the film takes place

at the electrode-electrolyte interface. This interface is characterised by a transition region made up of a charge unbalance known as the electric double layer.

The deposition process takes place within the double layer generated by the slight unbalance in the electric charges of the electrode and the solution. This interfacial difference in potential (that extends only a few nanometres, perpendicularly from the substrate surface) resembles in behaviour of that of a capacitor [66] (Figure 3.2).

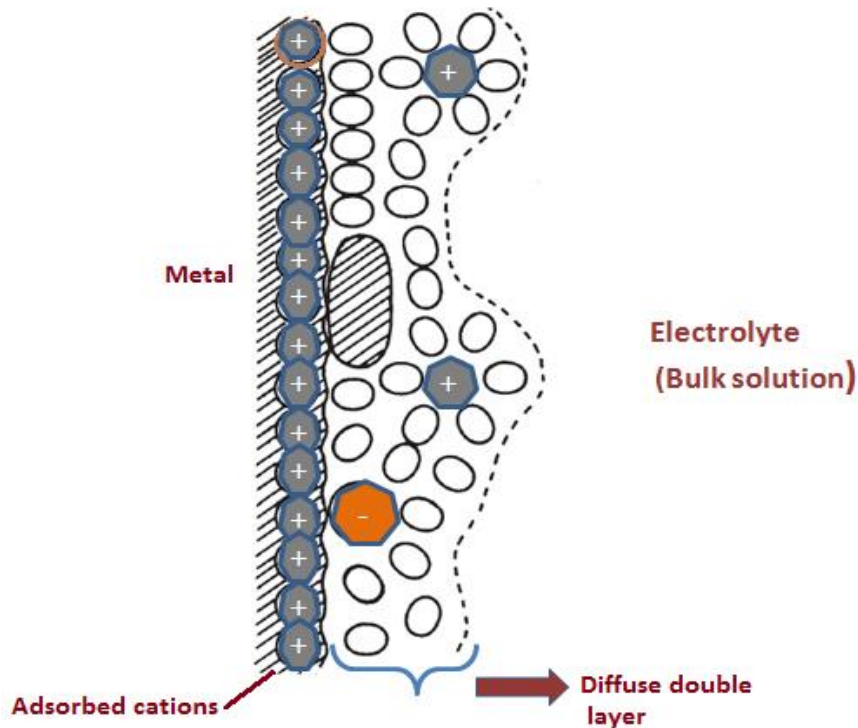


Figure 3.2. Schematic representation of the diffusion double layer at the electrode surface.

The electron transfer at the electrode (substrate) from the solution occurs in that takes place interfacial region at the electrode surface and encompasses a quantum-mechanical tunneling of electrons between the electrode and the electroactive species. Mobilities of the ions exert control on the total amount of charge passed through the solution and consequently on the deposition rate. Handling of the voltage employed

between the electrodes will influence the interfacial potential difference on the electrode reaction.

Cathodic electrodeposition was carried out on a ACM Instruments GilIAC potentiostat where a three electrode cell setup was employed. The electrochemical cell was located on a hot plate with temperature and magnetic stirring control (IKA (BASIC C)). The TiO₂ films were electrodeposited on ultrasonically cleaned indium doped tin oxide-coated (ITO) glass substrates at an optimised potential of -1.2V (vs. Ag/AgCl) at 4 different temperatures: 293K, 318K, 338K and 353K and no stirring. A high purity platinum wire was implemented as a counter electrode as shown in Figure 3.3.

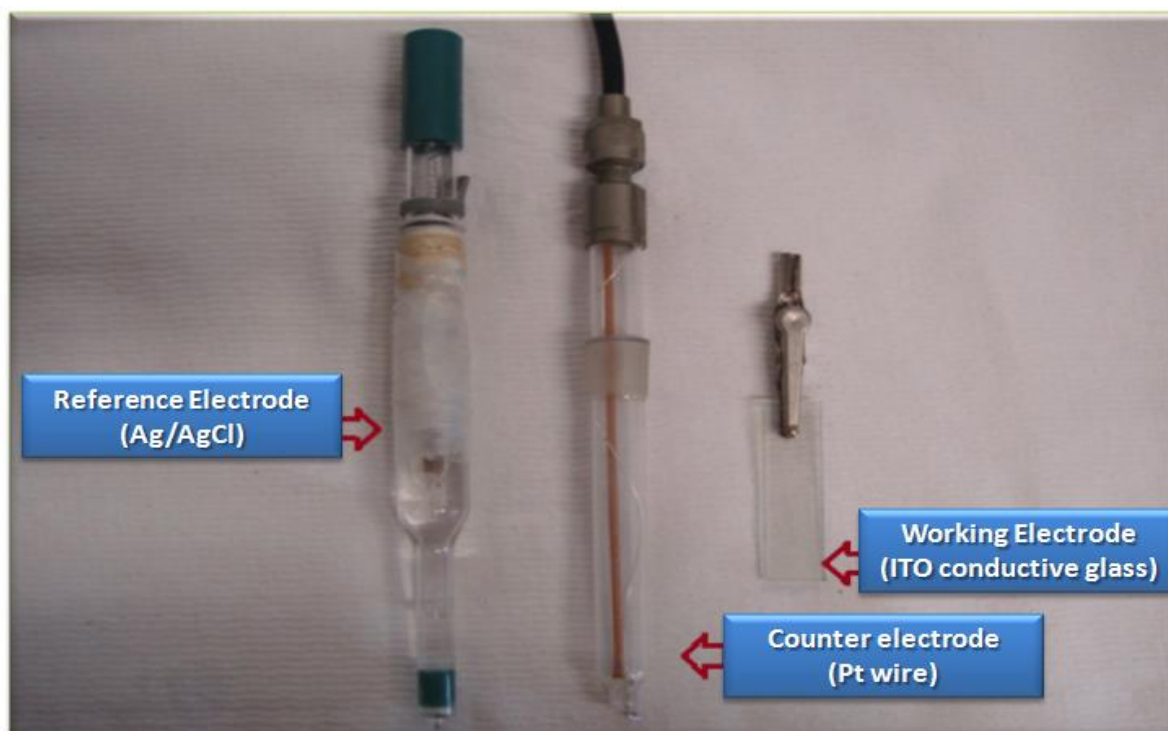


Figure 3.3. Three electrode set up used for the electrodeposition of TiO₂. Reference electrode (Ag/AgCl); working electrode (Indium doped Tin Oxide); Platinum wire was employed as counter electrode.

Ti peroxo complexes formed by the mixture of the chemical reactants were deposited as Ti peroxo hydroxide on the working electrode under the potential applied.

3.7 Characterisation Methods and Equipment

3.7.1 Raman Spectroscopy

Raman spectroscopy is a technique specialised in studying vibrational, rotational and low frequency modes in a material. It also permits the study of properties like crystallinity, orientation, composition, mechanical stress, and doping of a compound. It is based in the inelastic scattering of light by a material (Raman scattering). Fundamentally, the energy of incident laser photons (in the visible, near infrared or near ultraviolet regions) shifts up the electron cloud of the molecule to a ‘virtual’ energy state [68]. Most of the light is scattered elastically, so when the electron cloud drops back to its initial state, photons are released (in any direction) with the same energy as the incoming light (Rayleigh scattering) as shown in Figure 3.4.

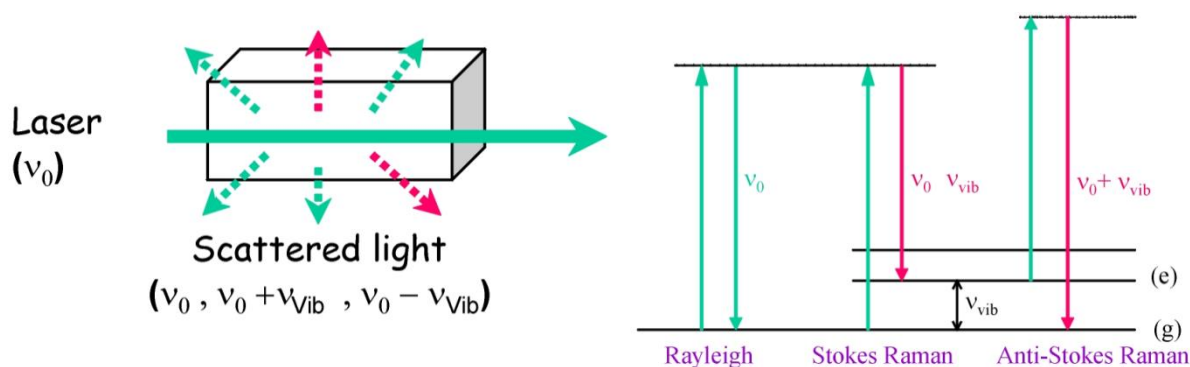


Figure 3.4 Schematic illustration of the vibrational energy state involved in Raman signal

Nevertheless, some of the energy of the incident laser photons is absorbed and an electron-hole pair is generated. The generated electron or hole will interact with the neighbouring lattice generating a phonon (Stokes Raman scattering, shift up) or destroying a phonon (anti-Stokes Raman scattering, shift down) during the interaction

with excitations in the system. Subsequently, the electron-hole pair will recombine by generating a photon. Due to energy conservation principle, the difference between the energies of the incident and scattered photons will be equal to the generated/destroyed phonon.

Figure 3.5 shows different stages involves in Raman Spectroscopy. As can be appreciated, a laser light is radiated to the sample. This light is filtered prior to illumination with the aim of blocking any undesired light being scattered. The light being collected from the sample requires a second filtration in order to block the elastic scattered light at the laser wavelength. This resultant filtered light is finally guided through the detector where the corresponding spectrum is obtained.

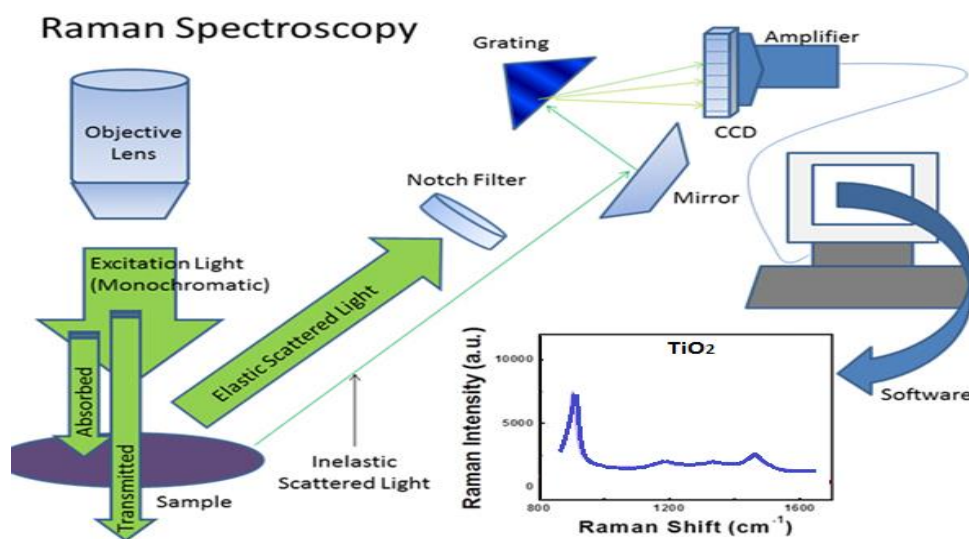


Figure 3.5 Schematic configuration of Raman spectroscopy.

Raman spectroscopy has the huge advantage that it can be used to characterize solids, liquids and even gas samples (although it cannot be used in metals or alloys). It is also a non-contact, non-destructive technique with little sample preparation and short time scale to obtain results which make it very useful in research [69]. For film charac-

terisation in this research it proved very convenient as there was no need of any additional preparation necessary.

Although one unfavourable condition of the method is that the Raman effect is very weak and it can be swamped by fluorescence from some materials, this was not the case in the present study. The Raman characterization was performed on a Nicolet Almega XR dispersive Raman spectrometer, equipped with a 785 nm laser accumulating 128 scans and an exposure time of 2 sec at 4cm⁻¹ resolution. The spectra were collected between 100-800 cm⁻¹ Raman shift.

3.7.2. UV-Visible Spectroscopy

Ultraviolet and visible (UV-Vis) absorption spectroscopy stands for the measurement of the attenuation of a beam of light after it passes through a sample or after reflection from a sample surface. Different molecules absorb radiation of different wavelengths of light, and this can be used to help to identify the substance of particular functional groups in chemical compounds. Absorption measurements can be at a single wavelength or over an extended spectral range. Ultraviolet and visible light are energetic enough to promote outer electrons to higher energy levels. An absorption spectrometer measures the way that the light absorbed by a compound varies across the UV and visible spectrum.

An absorption spectrum shows a number of absorption bands corresponding to structural groups within the molecule. Different structural groups may have very different absorption maxima and absorbances. UV/Vis Spectrophotometry is used to determine the absorption or transmission of UV/Vis light (180 to 820 nm) by a sample where the absorption of UV or visible radiation corresponds to the excitation of outer

electrons in the molecule. There are three types of electronic transition which can be considered: Transitions involving p, s, and n electrons, transitions involving charge-transfer electrons and transitions involving d and f electrons.

When an atom or molecule absorbs energy, electrons are promoted from their ground state to an excited state. In a molecule, the atoms can rotate and vibrate with respect to each other. These vibrations and rotations have discrete energy levels, which can be considered as being packed on top of each electronic level. The light source which gives the entire visible spectrum plus the near ultra-violet covering the range mentioned above (which extends slightly into the near infra-red as well) uses combination of two lamps - a deuterium lamp for the UV part of the spectrum, and a tungsten / halogen lamp for the visible part.

A beam of light from the visible and/or UV source is separated into its component wavelengths by a diffraction grating. Each monochromatic (single wavelength) beam in turn is split into two equal intensity beams by a half-mirrored device. One beam, the sample beam, passes through the film to be analysed. The other beam, the reference, passes through the clean substrate. For each wavelength of light passing through the spectrometer, the intensity of the light passing through the reference cell is measured (Figure 3.6).

The intensities of these light beams are then measured by electronic detectors and compared. The detector converts the incoming light into a current. The higher the current, the greater the intensity of the light. The intensity of the reference beam, which should have suffered little or no light absorption, is defined as I_0 . The intensity of the sample beam passing through the sample cell is also measured for that wavelength, defined as I . Over a short period of time, the spectrometer automatically scans all the component wavelengths in the manner described.

If I is less than I_0 for the same wave length, then obviously the sample has absorbed some of the light. Absorption may be presented as transmittance ($T = I/I_0$) or absorbance ($A = \log I_0/I$) [76]. An absorbance of 0 ($T = 1$) at some wavelength means that no light of that particular wavelength has been absorbed. The intensities of the sample and reference beam are both the same, so the ratio I_0/I is 1. \log_{10} of 1 is zero. Most spectrometers display absorbance on the vertical axis, and the commonly observed range is from 0 (100% transmittance) to 2 (1% transmittance). The wavelength of maximum absorbance is a characteristic value, designated as λ_{max} .

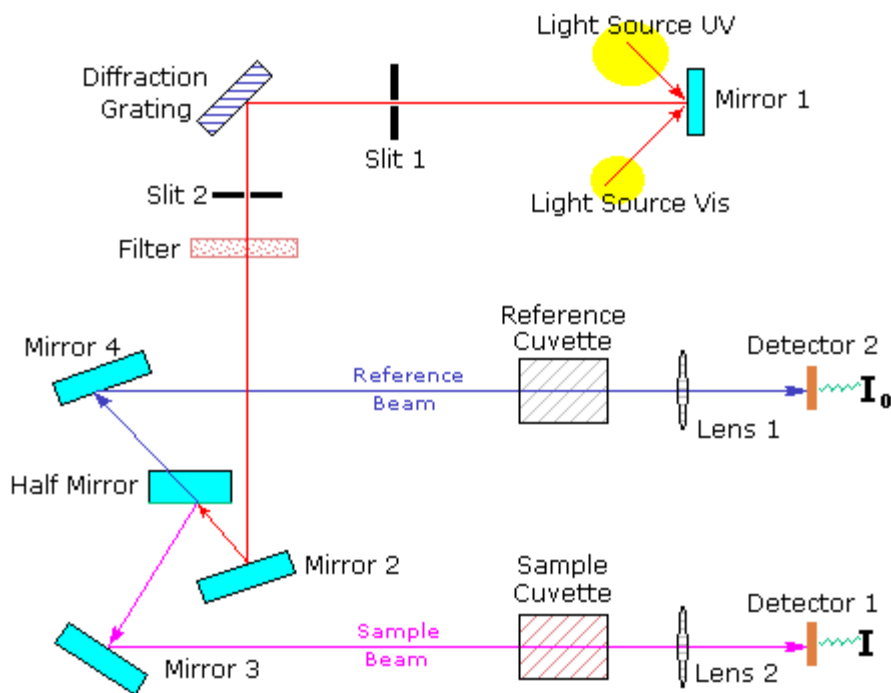


Figure 3.6. Ultraviolet and visible light spectra configuration [71].

The UV and visible spectra of the TiO₂ electrodeposited films were observed using a Perkin Elmer (Lambda 950) Spectrometer on the region 325-600nm with an identical glass slide in the reference beam. The test was performed on air and at atmospheric pressure with no special precautions to control humidity.

Band gap calculation, Tauc's law and Urbach tail region determination on the different films were possible after analysing the data obtained from UV/Vis.

3.7.3. X-Ray Diffraction

XRD diffraction is a non destructive analytical technique that reveals information about the crystallographic structure (including the determination of unit cell dimensions, phase, etc), the chemical composition (sample purity, etc) and physico-chemical properties in a sample. The method is based in observing the elastic scattered intensity of an X-ray beam that hits the sample and interacts with the electron clouds of the individual atoms in the material as X-rays primarily act upon electrons in atoms (Figure 3.7). That intensity of the scattered radiation is a function of the incident and scattered angle and the wavelength of the incident beam.

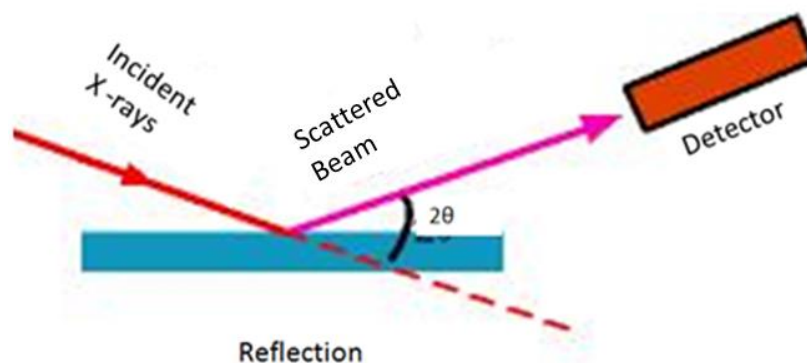


Figure 3.7. Schematic illustration showing the scattered x-ray deflected beam

X-ray electromagnetic radiation has wavelengths of a few Angstrom, the same as typical inter-atomic distances in crystalline solids. When x-ray photons collide with the electrons, some photons from the incident beam will be deflected away from the direction where they originally travel and can constructively interfere, producing a dif-

fracted beam (X-ray diffraction). In this case, the geometry of the incident X-rays impinging the sample satisfies Bragg's Law:

$$n\lambda = 2d \sin\theta \quad (3.2)$$

In Bragg's equation, λ is the wavelength of the incident x-ray radiation, n is an integer, d is the inter-atomic spacing of the sample (film or powder) and θ is the angle of the scattered radiation [72][73]. Once this condition is fulfilled, a peak in intensity occurs (Figure 3.8)

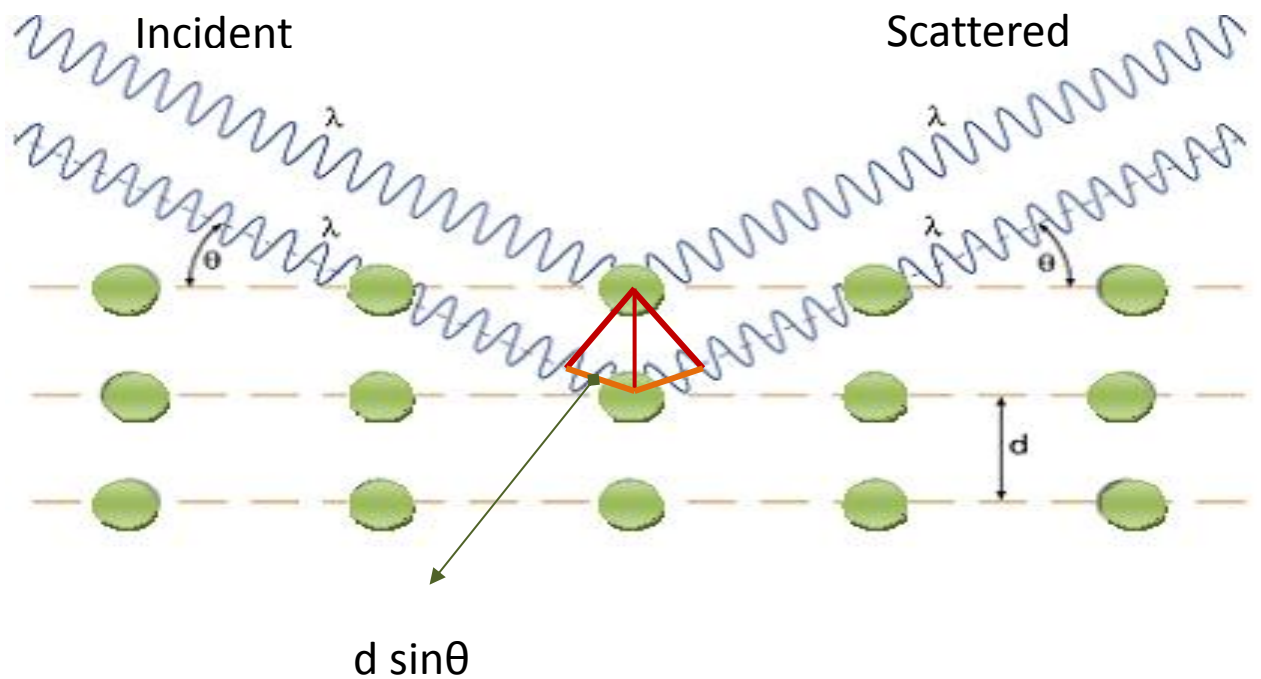


Figure 3.8 Bragg's Law. Constructive scattering of deflected waves [72].

If the wavelength of these scattered x-rays does not change (meaning that x-ray photons did not lose any energy), the process is called elastic scattering (Thompson Scattering) and it means that only momentum has been transferred in the scattering process. These are the x-rays that are measured in diffraction experiments, as the scattered x-rays carry information about the electron distribution in materials. A peak in intensity takes place when the sample contains lattice planes with d-spacings appropriate to diffract X-rays at that value of θ .

The intensity of the reflected radiation is continuously recorded using a goniometer, as the sample and detector are rotated during the test. Then this X-ray signal is then processed and converted to a count rate which is then output to a device such as a printer or computer monitor. The data is analysed for the reflection angle to calculate the various lattice spacings in a crystalline sample (d). This conversion of the diffraction peaks to d-spacing allows identification of the material as each material has a set of unique d-spacings. Greater d separation occurs at higher values of θ . The 2λ position of the diffraction peak is typically measured as the centre of the peak at 80% peak height [73].

The X-ray diffraction patterns were acquired with a Siemens/Bruker D500 diffractometer, scanning in the 2θ range of 20° to 60° , with a step size of 0.03° per second. The instrument is equipped with CuK α radiation of wavelength $\lambda = 0.15406$ nm.

XRD was particularly advantageous for obtaining the crystal phase and the crystallite size and for identifying the oxidation state of the titanium on the films after heat treatment and to establish the change in its crystallinity.

3.7.4. The Scanning Electron Microscope (SEM)

The Scanning Electron Microscope (SEM) is a microscope that uses electrons rather than light to form an image capable of showing very detailed 3-dimensional images at much higher magnifications than is possible with a light microscope. In SEM, a filament made of tungsten wire is heated by passing a high voltage through it. Negatively charged electrons are produced and directed down through the microscope by a series of electromagnetic lenses.

The beam of electrons passes through a small aperture before coming into contact with the sample. This electron beam is passed over the surface of the specimen and causes energy changes in the surface layer producing secondary electrons from within the sample. The secondary electrons are directed toward a detector that has a phosphor-ed light guide. When the electrons strike the phosphor they cause flashes of light that are picked up by a photomultiplier tube and are converted into an electrical signal that in turn goes to a cathode ray tube (monitor screen) (Figure 3.9). As the energy changes are generated on the surface of the sample, SEM yields information only from the surface or near-surface of the specimen.

In SEM, it is necessary that column always be is a vacuum (remove the air from inside the microscope) so as electrons (both from the beam and secondary) cannot move very far in air and are easily deflected.

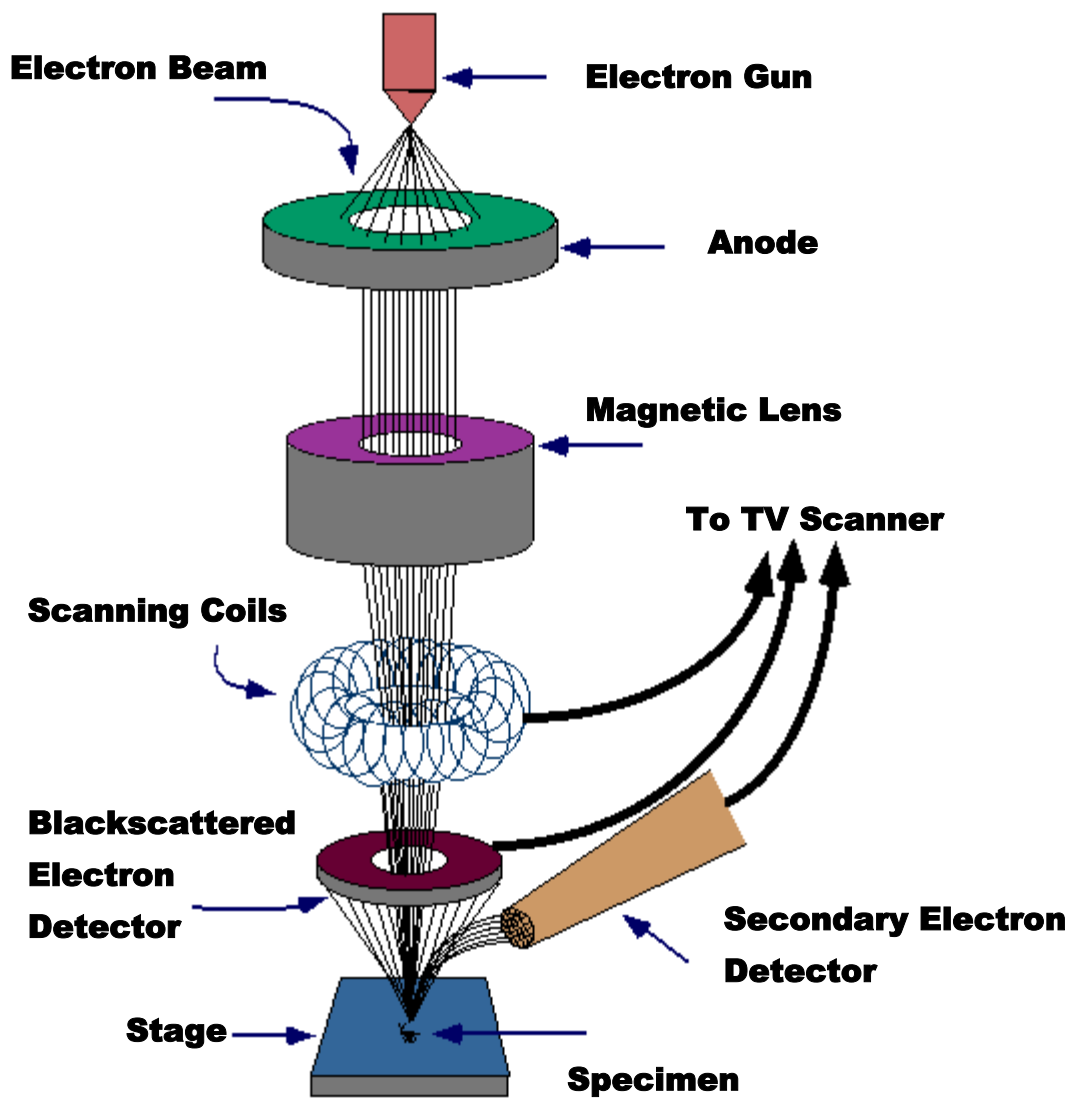


Figure 3.9 Diagram showing the components of SEM. Adapted from reference [74].

The SEM images, created without light waves are rendered black and white. When a SEM is used, the column must always be at a vacuum. There are many reasons for this. If the sample is in a gas filled environment, an electron beam cannot be generated or maintained because of a high instability in the beam. Gases could react with the electron source, causing it to burn out, or cause electrons in the beam to ionize, which produces random discharges and leads to instability in the beam. The transmission of the beam through the electron optic column would also be hindered by the presence of

other molecules. It appears as three dimensional but true 3-D can only be attained by using two pictures taken at different angles. Best resolution is up to 10 nm.

The SEM has a large depth of field, which allows a large amount of the sample to be in focus at one time. The SEM also produces images of high resolution, which means that closely spaced features can be examined at a high magnification. Preparation of the samples is relatively easy since most SEMs only require the sample to be conductive.

In a scanning electron microscope, a tiny electron beam is focussed onto the sample. Simultaneous to scanning the beam across a selected sample area, generated signals are being recorded and thereby an image is formed pixel by pixel., compact samples can thus be investigated by SEM. Valuable information about morphology, surface topology and composition can be obtained. SEM microscopes achieving resolutions below 1 nm are available now.

SEM images were obtained using a JEOL JSM 6300 Scanning Electron Microscope equipped with energy dispersive X-ray element analysis (EDX) and field emission method.

3.7.5. Energy Dispersive X-Ray Spectroscopy (EDX)

Energy dispersive X-ray spectroscopy (EDX) is a spectroscopic method which depends on the examination of the light emitted from the sample by means of electromagnetic radiation. By this technique it is possible to reveal evidence about the elemental and chemical features of the material. Each element has a unique atomic

structure and will emit x-rays that are characteristic of that element permitting the identification of the atomic structure.

As indicated earlier, the atoms are typically in the ground state when not excited and the electrons round the nuclei are in discrete energy levels. As exemplified in figure 3.11, when the sample is irradiated by electromagnetic radiation the electron will be excited to a higher energy, creating a hole. To fill this hole, an electron from higher energy level will release energy to move down to the lower and now unoccupied energy level as shown in Figure 3.10

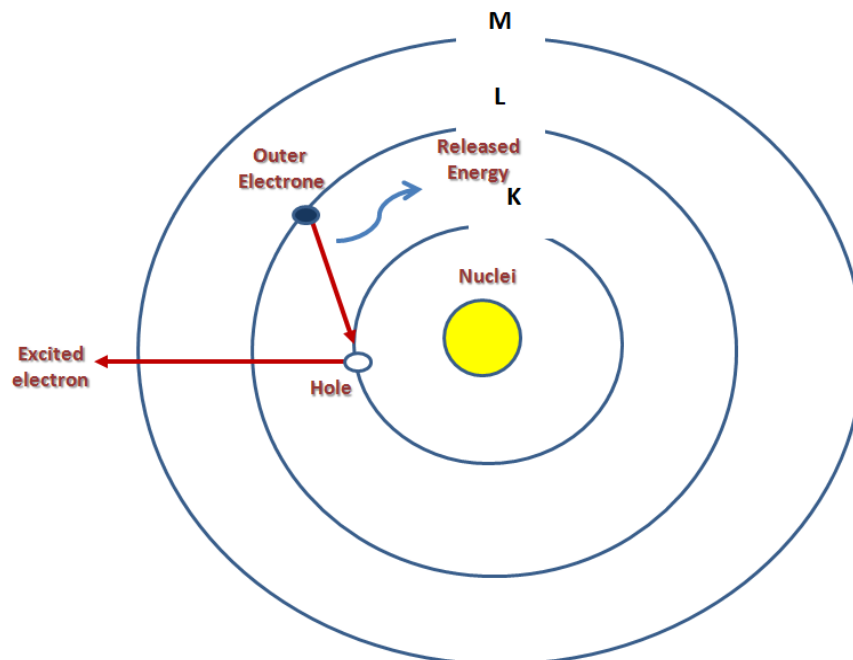


Figure 3.10 Illustration of the atomic structure and the principle of EDX [74].

The energy released will be emitted from the material in the form of X-Rays which can be measured employing an energy dispersive spectrometer. The measured X-Ray energy results from the difference between the energy levels within the atomic structure and is unique for each element in the periodic table. Therefore, EDX spectroscopy provides the elemental composition of the sample. [75].

JEOL Scanning Electron Microscope with a Link pentafet-ST windowless energy dispersive X-ray detector was used.

3.7.6. X-Ray Photoelectron Spectroscopy

Electrodeposited films were studied using X-ray photoelectron spectroscopy (XPS) in order to support EDX results on the chemical composition of the ceramic films. XPS techniques utilizes X-rays within photon energy range of 200-2000 eV in order to analyse the electronic state of the materials. The sample is hit by an X-ray beam with a fixed energy. The photon is absorbed by an atom causing the ionization of the atom and the emission of an inner-shell electron.

Ultra high vacuum is crucial so that the emitted electrons do not collide with gas molecules. The spectrum obtained is a curve of number of electrons detected per unit of time versus the binding energy of the electrons. Such electrons escape to the surface of the film from 1-10nm deep in the material. As each element possesses a characteristic set of peaks in the spectrum and the intensity of the peaks is proportional to the concentration of the species present, XPS is therefore a quantitative composition analysis method.

The penetrating photons interact with atoms in the surface region by the photoelectric effect, causing electrons to be emitted (Figure 3.11). The emitted electrons have kinetic energies given by [76]:

$$E_{KE} = h\nu - E_{BE} - \phi_s \quad (3.3)$$

where $h\nu$ is the energy of the photon, E_{BE} is the binding energy of the atomic orbital from which the electron originates, and ϕ_s is the spectrometer work function.

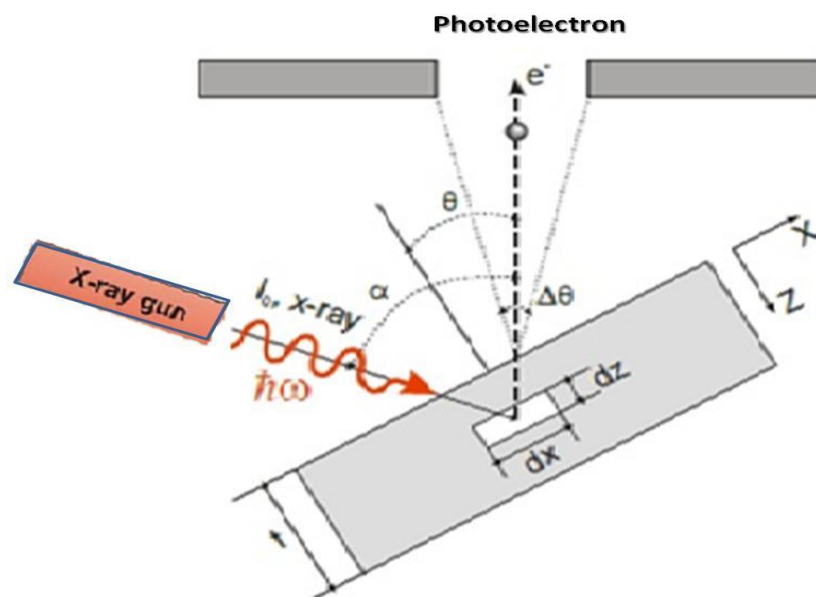


Figure 3.11 Schematic diagram of X-ray photoelectron spectroscopy [78] .

X-ray photoelectron measurements (XPS) were made using a VG ESCALAB 210 Photoelectron Spectrometer. The X-ray source was a non-monochromated Al Ka source (1486.6eV), operated with an X-ray emission current of 20 mA and an anode high tension (acceleration voltage) of 12 kV. The takeoff angle was fixed at 90° relative to the sample plane. The area corresponding to each acquisition was of 1 mm². Each analysis consisted of a wide survey scan (pass energy 50eV, 1.0eV step size) and high-resolution scans (pass energy 50eV, 0.05eV step size) for component speciation. 10 scans were taken for the survey spectra, and 5 scans were taken for each one of the expansions. The software CasaXPS 2.3.13 was used to fit the XPS spectra peaks.

3.7.7. Surface profilometry

The profilometer method is one of the more practical techniques of determining surface features on film. It is a physical contact device that permits the thickness of a solid layer to be measured. A diamond-tipped probe is positioned on top of the layer

close to the step formed by the film deposited on the substrate. Electro-mechanically operated, the tip sits on and moves through the surface, responding on the z axis as the variations of the material are sensed by the tip.

The scan rate of the movement of the probe and the force of the tip of the stylus on the surface can be changed as they can affect the reading. As the probe reaches the end of the deposited material, the stylus steps down and makes contact with the substrate underneath. The height of the step corresponds to the thickness of the film (

Figure 3.12.) It is significant that both, the substrate and the film deposited are as uniform as possible.

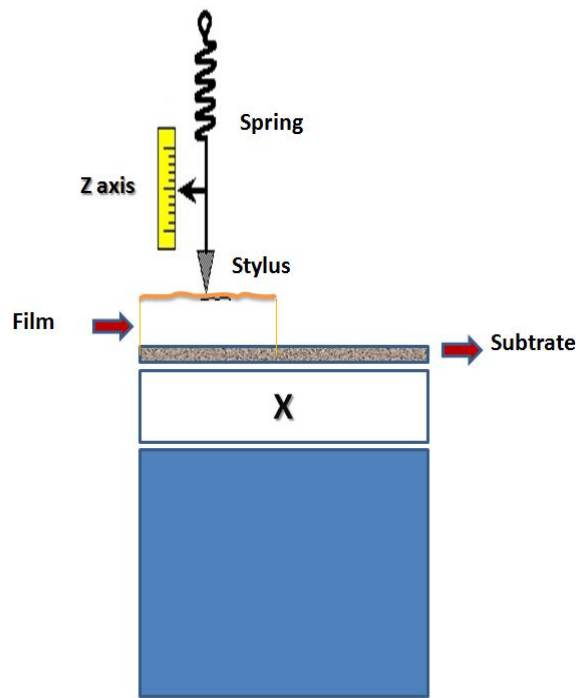


Figure 3.12. Principle of Profilometer [78].

Roughness of the film is also obtained as well as rugosity statistical characteristics of the deposition layer (variations in amplitude) with this device. Average roughness R_a , the arithmetic average deviation from the mean line is obtained via the software present with the device. A Dektak 3ST stylus surface profilometer was employed to

deduce film thicknesses, The standard stylus diamond of 2.5 micron radius performed the measurements at a medium scan speed and a tracking force of 5mg.

3.7.8. Non-Contact Atomic Force Microscopy

This instrument is essentially an extremely high resolution profilometer. In order to understand the method straightforwardly it is advisable to explain firstly the basics of its predecessor (contact mode AFM). Contact mode AFM is still one of the more broadly used scanning probe modes, and operates by combing across the sample, a very fine tip having a typical end radius of a few nanometres (attached to a low spring constant cantilever) that is used as a probe. An exceptionally low force ($\sim 10^{-9}$ N, interatomic force range) is sustained on the cantilever, thus pushing the tip against the sample as it investigates through the surface. Whichever the repulsive force between the tip and sample or the tangible tip deflection is recorded relative to spatial variation and then converted into an analogue image of the sample surface. With this aim, the cantilever is attached to a piezoelectric transducer (pzt). Light from a laser diode is reflected from the cantilever onto a quadrant photocell. As the cantilever and tip move over the surface, the cantilever bends and the light beam reflected from the cantilever is diverged by the bending, henceforth its position on the photocell changes [79].

By maintaining a constant tip-sample separation and using Hooke's Law ($F = -kx$ where F is force, k is the spring constant, and x is the cantilever deflection), the force between the tip and the sample is calculated. Finally, the distance the scanner moves in the z direction is stored in the computer relative to spatial variation in the x - y plane to generate the topographic image of the sample surface.

The In non-contact setup, the cantilever is oscillated at its resonant frequency. In this operation, what is being sensed is changes in force between the tip and sample, despite the fact they are not in contact. These force changes are also denoted to as the force gradient. As the probe gets near to the sample surface, the force gradient changes, consequently changing both the oscillation amplitude and phase of the pulsating cantilever. Either one, the change in amplitude or change in phase can be identified and used to regulate the trailing of the probe over the surface (feedback-control loop) (Figure 3.13).

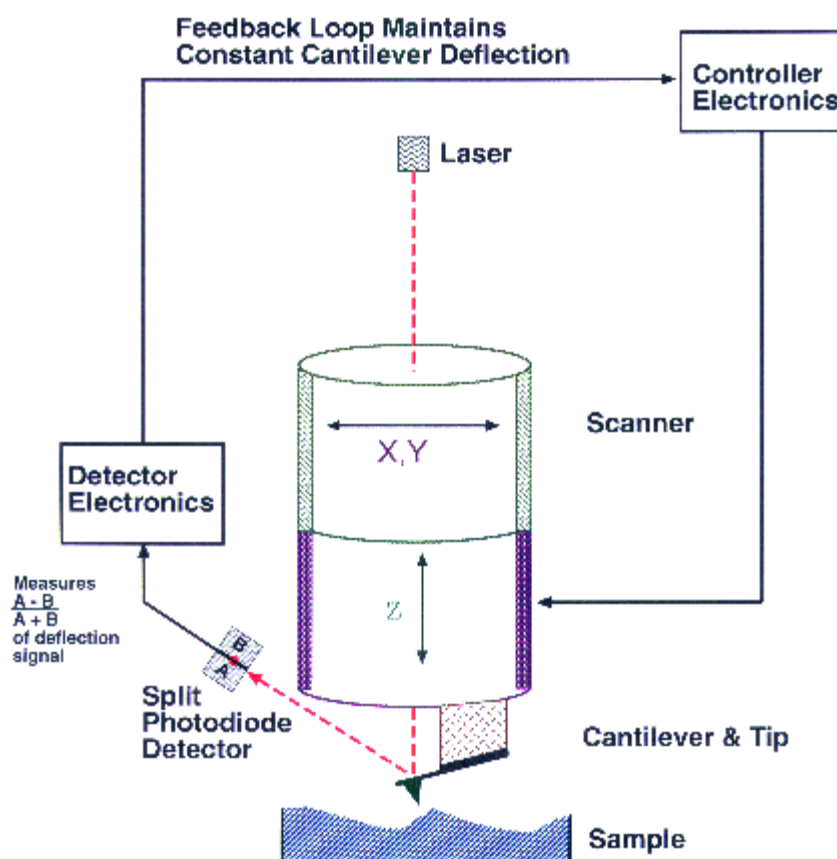


Figure 3.13 Schematic illustration of Atomic Force Microscopy (AFM)[80].

Amplitude detection is the non-contact method usually used for high-amplitude cantilever vibration. The AFM tip is first conveyed (manually) close to the sample surface

before the scanner makes a final tuning in tip–sample distance based on the chosen setpoint. The tip, now in ‘contact’ with the sample surface as a result of any adsorbed gas layer, is then scanned through the sample under the action of a piezoelectric actuator. The laser beam directed at the back of the cantilever–tip device reflects off the cantilever surface to a split photodiode, which measures the small cantilever deflections. The feedback loop, conserves constant the tip–sample separation by moving the scanner in the z direction to keep the deflection set.

The study of surface morphology and roughness of the as-deposited and annealed films were possible with the aid of digital Nanoscope III atomic force microscope (AFM) in a non-contacting mode. . The area scanned was $5\mu\text{m} \times 5\mu\text{m}$ and the scan rate was $80 \mu\text{m/s}$.

Chapter 4

Experimental Results

4.1 Introduction

Several parameters had to be considered in the preparation of the TiO₂ films: deposition potential, deposition time, temperature, pH, annealing temperature, annealing time etc. An all-inclusive study of the interaction of all these variables on the properties of the final films is outside the objectives of this research. The intention in this chapter is to focus on the experimental findings about the electrochemical solution, followed by a comprehensive chemical and physical analysis on the final dried hydroxyl gel before and after thermal treatment.

4.2 pH variation in electrochemical solution due to Temperature

As discussed in earlier (section 3.5) there were two different sets of preliminary or exploratory tests which guided the subsequent experimentation towards the goal of optimising the titania film. Table 4.1 shows the value of pH of a peroxy complex solution that was heated up at a rate 1°C/min and kept under constant slow stirring (100rpm).

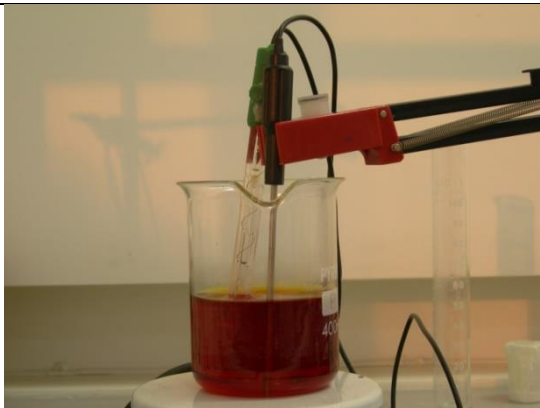
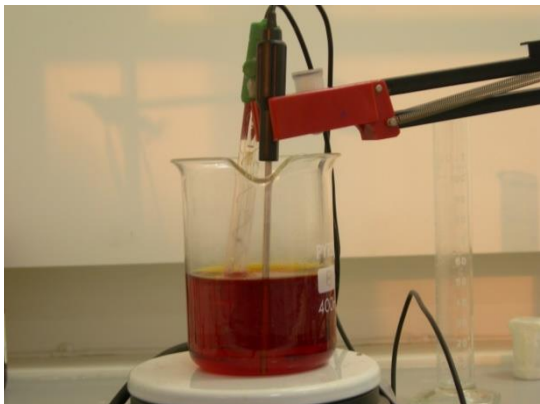
Table 4.1 Experimental variation of pH of Peroxo Titanium solution at different temperatures.

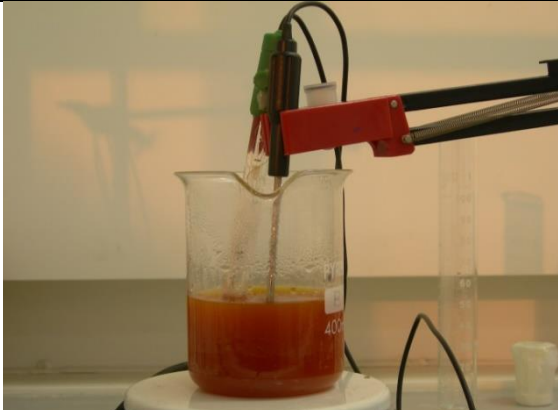
Temperature (K)	pH (± 0.03)
293	1.36
303	1.20
313	1.02
323	0.87
333	0.85
343	0.84
353	0.79
363	0.77

From 293K-318K the solution maintains its original intense transparent red. From 318K-333K the colour slowly changes towards orange and becomes less and less transparent. At 344K the solution becomes ochre and it has completely lost the transparency. At 353K the colour changes abruptly to pale yellow and opaque. The solution was highly acidic, having the pH value between ~ 0.8 and 1.4. The addition of hydrogen peroxide to titanyl sulphate diluted in sulphuric acid generated an intense red colour solution due to the formation of peroxo complexes of Ti. The solution maintained its original intense transparent red colour for the bath temperature from 293K to 318K. The colour changed gradually to orange while losing transparency in the temperature regime of 318K to 333K. Continual heating of the Peroxo-complex of titanium solution also caused hydrolysis and a mixture of metatitanic acid ($\text{TiO}_2 \cdot n\text{H}_2\text{O}$) and sulphuric acid was formed according to the chemical reaction:

$\text{TiOSO}_4 + \text{H}_2\text{O} \rightarrow \text{TiO}_2 \cdot n\text{H}_2\text{O} + \text{H}_2\text{SO}_4$, giving rise to a decrease of pH [81]. The metatitanic acid is not soluble in water and forms a colloidal solution up to 323K. A further rise in temperature to 344K turned the solution ochre and opaque. At 353K, the precipitation of white powder was observed to have occurred due to the agglomeration of the colloid particles. Consequently, the solution colour changed abruptly to pale yellow and became translucent. The following table (Table 4.2) presents the values of pH at three different temperatures and a picture of the solution.

Table 4.2. Colour variation of the Peroxo Titanium solution at different temperatures and its correspondent pH value.

Colour of Solution	Temperature	pH
	298 K	1.28
	313 K	1.02

Colour of Solution	Temperature	pH
	338 K	0.85

Similar pH dependent colour changes were reported for the product of the hydrolyzation of TiCl₄ by Cai et al. [61]. The pH of the solution was found to be increasing from 3.0 to 8.4 when the solution diluted to 0.10 M in de-ionized water was followed by keeping it refrigerated over 17 days (it becomes relevant to emphasise once more the absence of colour photographs on their paper). Although increasing the temperature did not increase the pH of the solution but rather the opposite, it is important to realise that the changes in colour indicate a change in the chemistry of the solution. As expected, pH is dependent from temperature, however, as variation of pH occurs in the very acidic region (1.36 – 0.77) generating the precipitation of (TiO₂·nH₂O).

4.3 Results of Cyclic Voltammetry

From the three chemical components of the electrochemical bath: H₂O₂, TiSO₄ and NH₃NO₄, three redox pair solutions were prepared to observe the change in current due to potential and therefore establish the appropriate potential required for the electrodeposition, by determination of the chemical species present in the solution.

Using the same composition as the electrochemical bath employed in all depositions (as presented in section 3.4), solutions of TiOSO₄:NH₃NO₄, TiOSO₄:H₂O₂ and NH₃NO₄:H₂O₂. Cathodic Voltammetry was performed for these solutions under the same conditions: 1000mV/min scan rate, between 2V and -2V of potential (vs. Ag/AgCl) at room temperature. Figure 4.1 illustrates the three cyclic voltammetry analysis for each solution.

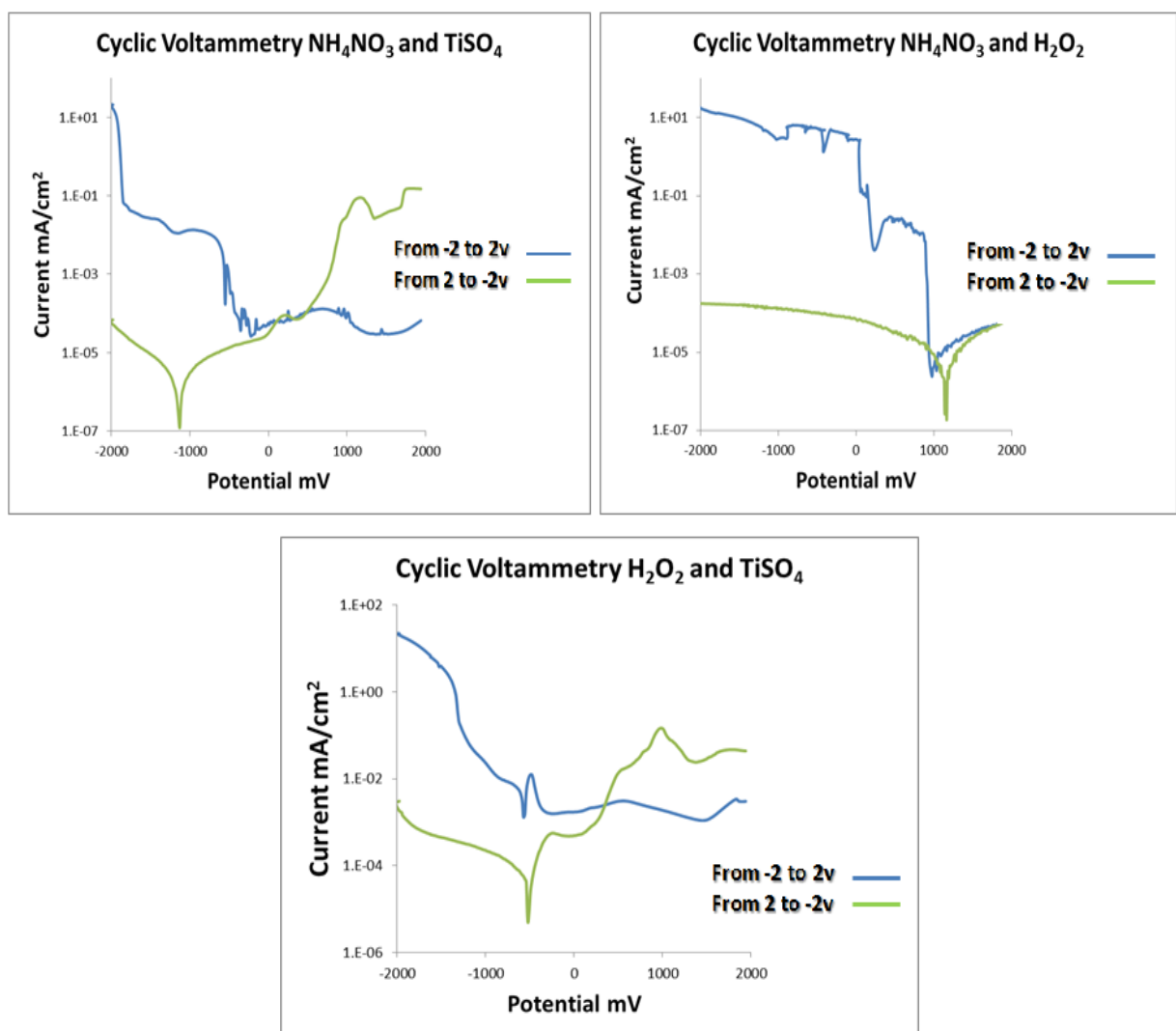


Figure 4.1. Cyclic voltammetry for the redox pairs; TiOSO₄:NH₃NO₄, TiOSO₄:H₂O₂ and NH₃NO₄:H₂O₂ at 293K.

It is noticeable that for the three solutions there is a sharp rise in cathodic current beyond -0.5V with respect to the Ag/AgCl reference electrode. According to equilibrium data for each system, the ions present in solution are expected to be: Ti⁺² (titanous ion) H₂S (aq)(aqueous hydrosulfuric acid), NH₄⁺ (ammonium ion) and H₂O₂ [100].

Secondly, as shown in Figure Figure 4.2, the cyclic voltametry was performed at room temperature to optimize the deposition potential of TiO₂ thin films in the complete peroxo-complex of titanium solution by making sure the ionic species needed for the electrochemical deposition were present in the bath. A sharp increase in the cathodic current was observed for the potentials ranging from -1.0V to -1.50V with respect to the Ag/AgCl reference electrode, indicating the diffusion-limited deposition of metallic Ti via the forward path. Further increase of the current for a potential larger than -1.53V was attributed to the hydrogen evolution reaction [82]. Highly transparent (milky-white) films of TiO₂, with silvery-grey coloured edges (metallic Ti particles) were deposited on the substrates during this test.

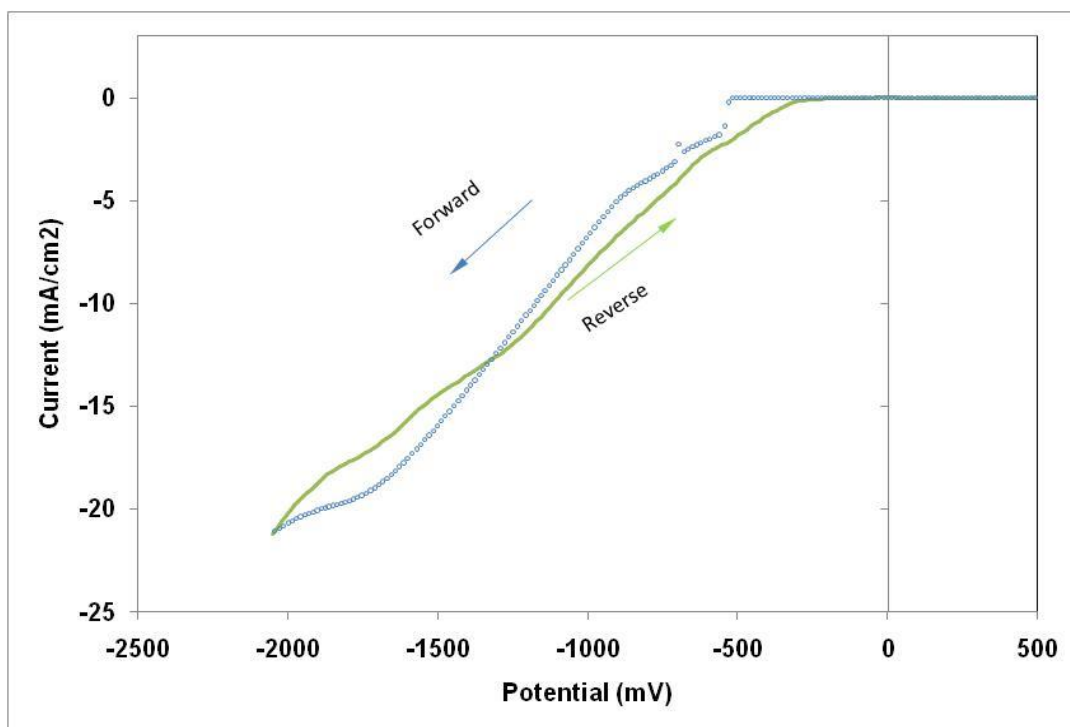


Figure 4.2. Experimental voltammetry of Peroxo-titanium in a aqueous solution at a scan rate of 120m V/min, pH 1.3, 293K. There is a rapid increase in current around around -1.2 V corresponding to the formation of metallic Ti.

Finally, 2 more cyclic voltammetry tests were performed. This time the temperature of the bath was set at 313K and 336K respectively, maintaining all the other parameters equal.

The same acute increase in cathodic current (associated to the metallic electrodeposition of Ti) was observed in the same range ($E < -1.2V$ with respect to the Ag/AgCl reference electrode). It can be noted that the rise in current is more intense for the temperature of bath equal to 336K. There is a strong indication that at such temperature, the diffusion process of the titanium ion from the solution to the electrode in form of metallic Ti, is more vigorous than at 313K.

4.4 Chemical analysis of electrodeposited titania films by Raman spectral analyses

Figure 4.3 shows the Raman spectra (at room temperature) for the films deposited after annealing. Also on the graph, the Raman shift for the crystallographic phase Anatase is shown in order to identify any structural change within the films.

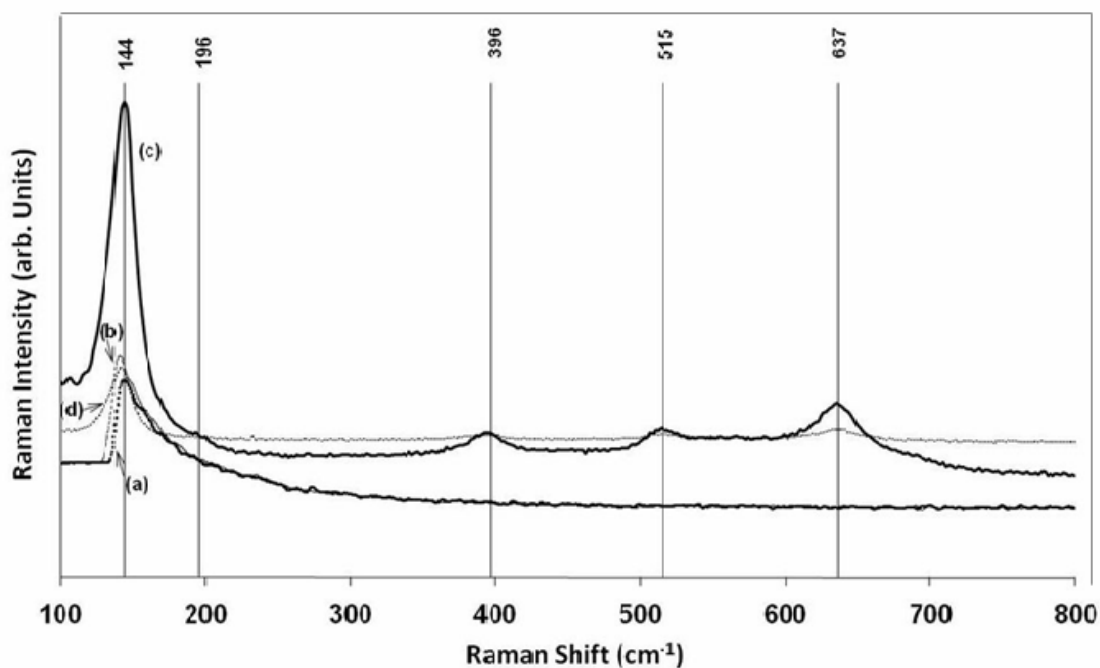


Figure 4.3. Raman Spectra for TiO₂ films electrodeposited at temperatures: (a) 296K, (b) 318K, (c) 336K and (d) 353K. The Raman values for anatase peaks are shown for reference (anatase powder from Aldrich)

Furthermore it is shown (for the films annealed at 823K) the crystallographic phases relative to the bath temperature. The origin of the Raman bands in natural and synthetic anatase samples between 100cm⁻¹ and 800cm⁻¹ region was ascribed to different modes of vibrations of Ti-O bonds due to short range interactions in distorted tetragonal structure [83]. The assignments of the peak positions of the spectra in Fig-

ure 4.3 are summarised in Table 4.3 and it can be maintained that the agreement between experimental and theoretical values is good.

Table 4.3 Raman Peak positions and their assignment for anatase.

Peak positions (cm ⁻¹)		Intensity of the peak				Assignments of vibrations	
Experimental	Theoretical	Sample bath temperature (K)				Mode	Type
		296	318	336	353		
144	144	2443	2500	13059	5000	E _g (1)	0-Ti-0 bending
196	197	109	116	194	199	E _g (2)	0-Ti-0 bending
396	400	81	91	812	385	B _{1g}	0-Ti-0 bending
515	507 +519	124	138	726	517	B _{1g} ⁺ A _{1g}	Ti-0 bond stretching
633	640	49	4	1868	87	E _g (3)	Ti-0 bond stretching

The structure of the film was found to be primarily anatase but the relative intensities of Raman modes were dependent on the bath temperature. The intensities of the peaks in the Raman spectra directly depend on the amount of crystalline material without a significant influence of the crystal size. The film deposited at 336K showed 32-38% more anatase phase than the films electrodeposited at other bath temperatures. The Raman activities were found to be the most pronounced for the film deposited at bath temperature of 336K, showing a sharp peak at 144cm⁻¹ corresponding to the E_g mode of vibration and also the presence of B_{1g}, A_{1g} and E_g modes of vibrations. The presence of the anatase phase is dominant in films electrodeposited at 336K possibly due to the thermal effect on kinetic energy of ions [84]. The presence of 144cm⁻¹ (E_g)

peak for the films deposited at 296K and 318K indicates that these films are primarily anatase in structure. However the peak is broad and low in intensity. The minor Raman peaks for anatase (196, 369, 515 and 633) were also absent from the spectra possibly due to crystalline imperfections or nonstoichiometric titanium oxide [85]. The Raman intensity of the E_g peak at 144cm⁻¹ was found to have diminished for the film deposited at 353K, indicating small amount of polycrystalline anatase phase.

4.5 Energy dispersive spectroscopy

EDX analysis was used to verify the presence of TiO₂ on the films after annealing. The elemental composition of the film surface was found to be 17.17 : 82.83 (deposition temperature, 338K) and 16.89 : 83.11 (deposition temperature, 353K) (atomic%) ratio for Ti : O.

4.6 Optical characterisation

UV/vis spectra in Figure 4.4 obtained for titania films shows that the intensity of optical absorption increased with the rise of the bath temperature. This observation is consistent with the thickness measured earlier for the films deposited at different bath temperatures. The fundamental absorption edge was found to be approximately 375 nm of indirect band gap of TiO₂. Irrespective of the bath temperature, the spectra show two distinct regions: (i) absorption edge due to interband transition at 3.53-3.73eV (351-332nm) and (ii) absorption tail at the low energies, 2.65-3.00eV (468-413nm).

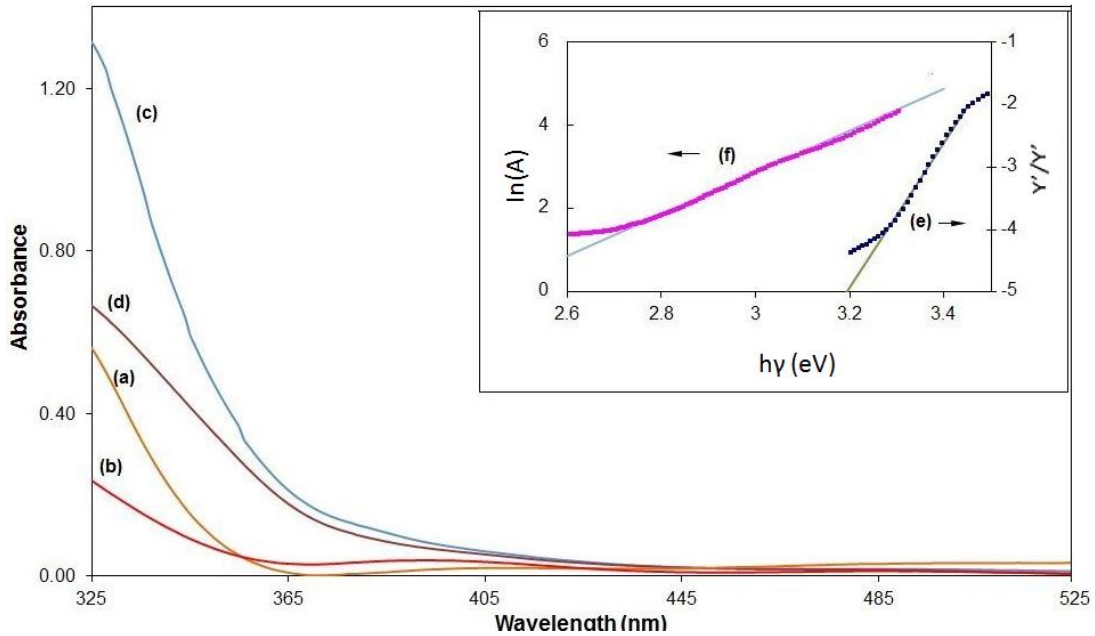


Figure 4.4 Optical absorption spectrum of TiO₂ films of ITO glass at different bath temperatures (a) 296K, (b) 318K, (c) 336K and (d) 353K. All samples were heat treated at (823K in air for 30 min). (e) Tauc region for the near the absorption edge, (f) Urbach low energy tail.

Similar results have been reported by Reddy et al [23] using the method of extrapolation of the absorption edge onto the wavelength axis. For the interband transition (high energy region), the dependence of absorption coefficient $A(h\nu)$ on incident photon energy $h\nu$ is given in terms of the Tauc's power law in the form [86]:

$$A(h\nu) = \frac{B}{h\nu} (h\nu - E_0 \pm E_p)^n \quad (4.1)$$

where B is a constant, depending upon the film thickness, minimum metallic conductivity, refractive index, width of band edges and nature of electronic transition. $h\nu$ is the energy of the photon (frequency times Plank constant), E_0 is the optical band gap for the interband transition.²⁵, E_p is the phonon energy and n is a constant that depends on the type of absorption edge [87]. The \pm sign corresponds to the type of interaction that occurs in the optical absorption process: $(+E_p)$ for phonon energy emission or $(-$

E_p) for phonon energy absorption [88]. E_p is much lower than E_g and can be dismissed. The power index n signifies the nature of electronic transitions associated with optical processes. In order to determine the values of n and E_0 simultaneously, Equation (1) is written in the modified form [89]

$$\frac{Y}{Y'} = \frac{h\nu - E_0}{n} \quad (4.2)$$

Where $Y = h\nu A(h\nu)$ and its energy derivative $Y' = \frac{\partial Y}{\partial(h\nu)}$

Equation (2) offers a method of determining values of n and E_0 simultaneously.

The value of n was estimated to be 2 from the slope to the best linear fit to the plot

of $\frac{Y}{Y'}$ against $h\nu$ in Figure 4.5 for the film produced at the bath temperature of 296K, indicating that the transition was allowed indirect. The intercept on the ordinate extrapolated to $h\nu=0$ produced a value of 3.4eV for E_0 .

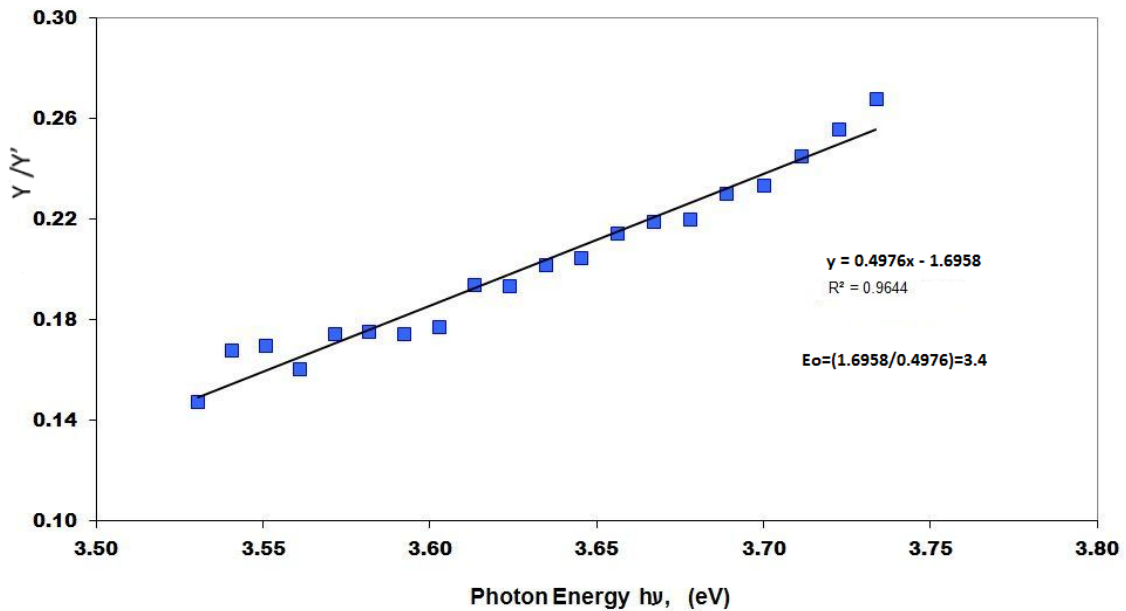


Figure 4.5. Numerical fitting of Y'/Y vs $h\nu$. Y' is the numerical differentiation for A $h\nu$ vs. $h\nu$. The inverse of the slope is the exponent n in the Tauc equation.

The low energy absorption regime represents localized states tailing into the gap. Figure 4.6 shows the logarithm-linear plot of absorption coefficient (α) calculated from the graph for the photon energy within this regime below the optical gap $E_0 = 3.4\text{eV}$. This exponential dependence of (α) on the incident photon energy $h\nu$ is generally described in terms of the Urbach law in the exponential form [90]:

$$A(h\nu) = A_0 \exp\left[\frac{h\nu - E_{CE}}{E_U}\right] \quad (4.3)$$

Where A_0 is a fitting parameter (a constant characteristic of the material). The converging energy E_{CE} is taken to be higher than the optical band gap energy E_0 and ($h\nu$) is the photon energy. The Urbach energy E_U which is defined as the width of band tails of localized states into the gap was found to be 0.39eV from the inverse of the slope of the linear fit.

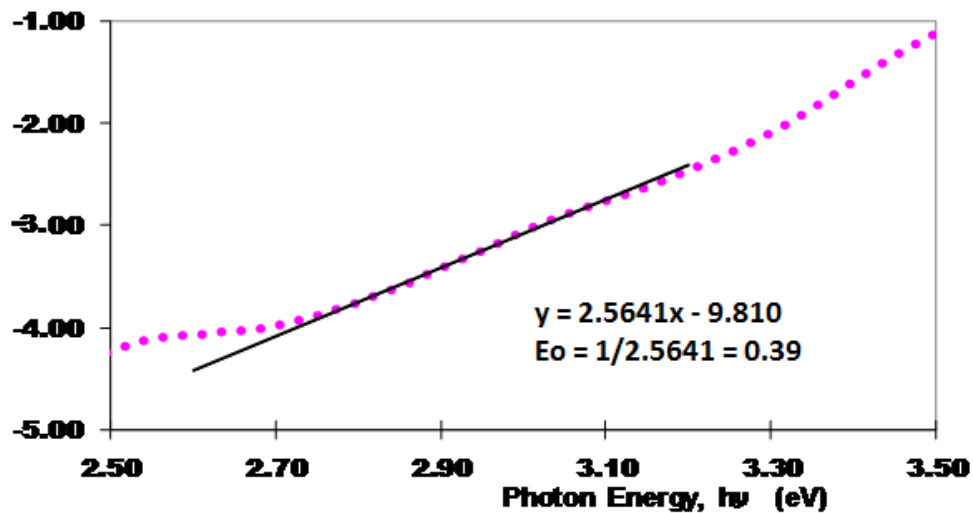


Figure 4.6. From the inverse of the slope of the linear part of the curve (Urbach region) is E_U (Urbach energy) for TiO_2 film electrodeposited at 296K , -1.2V (potential).

Table 4.4 shows the estimation of band gap calculated from the Tauc region and the value of the constant n plus the Urbach energy for films after annealing.

Table 4.4 Parameters derived from optical absorption spectra.

Deposition Temperature (K)	Thickness* (nm)	Analysis due to			
		Tauc		Urbach	
		E ₀ (eV)	n	α ₀	E _u (eV)
296	53.0 (185.2)	3.4	2	7 x 10 ⁻²⁶	0.4
318	61.5 (190.4)	3.4	2.	5 x 10 ⁻⁵	0.3
336	87.2 (223.1)	3.3	2	0.0873	0.3
353	113.1 (264.7)	3.2	2	0.2464	0.3

* values in parenthesis are thickness of as deposited peroxotitanium hydrates

Similar calculations for n , E_0 and E_u were performed for the films deposited using different bath temperatures and the results were included in Table 4.4 Values are found to be in agreement with those reported for TiO₂ films deposited by reactive RF sputtering [91]. Transitions are allowed indirect giving the values of E_0 of TiO₂ films which were dependent upon the crystalline phase, grain size, stoichiometry, density and defects [92]. Thermal energy is significantly smaller than E_U and therefore, the value of E_U may be correlated to carrier concentration and shallow traps below the conduction band due to structural disorder.

4.7 X-Ray Diffraction

Initially, the precipitate formed when the peroxocomplex of titanium was heated up (section 3.1) the produced precipitate was collected, dried in air at room temperature

and then analysed by XRD, as precipitated and after annealing the powder at the same conditions of the films: 823 K for 30 min. Figure 4.7. Shows the peak at $2\theta = 25.281$ that correspond to the (1 0 1) diffraction pattern for Anatase [93]. The result confirms the Raman spectroscopy results.

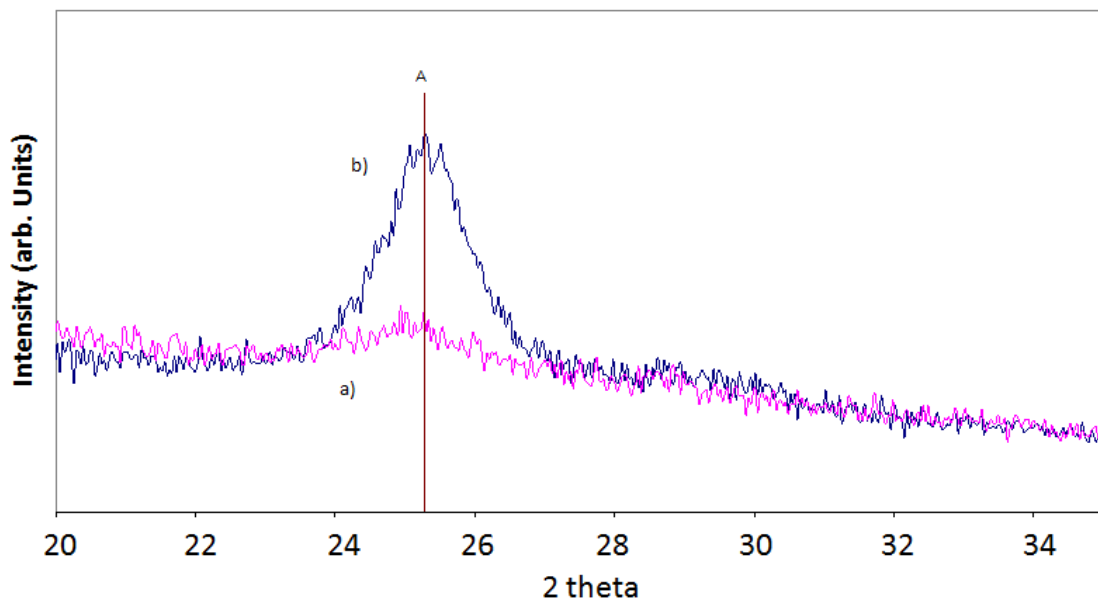


Figure 4.7 XRD of TiO₂ precipitated after heating the solution. a) As precipitated. b) After annealing at 823K for 30 min.

XRD in spectra Figure 4.8 of the same TiO₂ films were obtained for further evidence of post annealing crystallisation of TiO₂ electrodeposited at 336K. The as-deposited TiO₂ film is amorphous and the interfacial interactions are believed to be responsible for the broadening of XRD peak at $2\theta = 25^\circ$. The positions of the peak were compared with the standard data in Table 4.5 and the peaks were identified with the anatase phase of polycrystalline TiO₂ films with a preferential orientation along (101) direction [94].

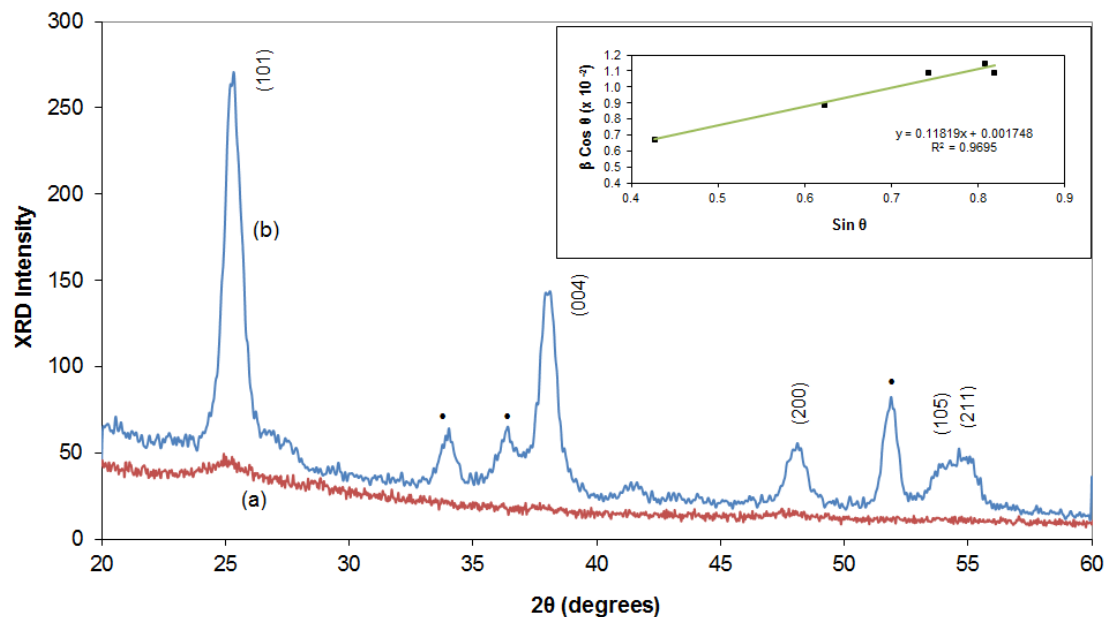


Figure 4.8 XRD of TiO₂ electrodeposited film (-1.2V; 30 min, 336K) as deposited (a) and after annealed at 823K for 30 min (b). Anatase peaks for different crystallographic planes are labelled. The peaks from the conductive glass Indium doped tin oxide (ITO) glass substrate are marked as solid circles (•). The inset shows the linear fitting of the Hull equation.

The peaks from the conductive glass indium doped tin oxide (ITO) glass substrate are marked as solid circles. The experimental results are compared with standard data and summarized in Table 4 which gives the observed X-Ray diffraction peaks for TiO₂ films electrodeposited at -1.2V (vs Ag/AgCl) and 338K bath temperature for 30 min with further heat treatment (823K for 30 min.). It also shows the Standard values of the Anatase phase for 2θ as well as the Miller indices for each crystallographic plane [93].

Table 4.5. XRD peaks for TiO₂ electrodeposited films (Experimental and Standard [95])

2θ (Degrees)		(h k l)	d (Å)		Phase Assigned
Observed	Standard		Observed	Standard	
25.34	25.281	1 0 1	3.512	3.520	Anatase
38.11	38.576	1 1 2	2.359	2.332	Anatase
48.11	48.050	2 0 0	1.889	1.892	Anatase
53.84	53.891	1 0 5	1.701	1.699	Anatase
55.07	55.062	2 1 1	1.666	1.666	Anatase

The grain size is calculated using the Scherrer equation [96]:

$$t = \frac{K \cdot \lambda}{\beta \cdot \cos\theta} \quad (4.4)$$

Where:

t is the crystallite length, in nm

K is a numerical constant, equal to 0.90

λ is the XRD wavelength, equal to 1.5406 Å

β is the width of the peak at half maximum intensity of a specific phase (hkl), in radians

θ is the Bragg angle, in radians. [*2θ* is equal to 25.34° (0.442 radians)]

The calculated value of the grain size was 88nm.

The plot of $\beta\cos\theta$ as a function of $\sin\theta$ in the inset of Figure 4.8 was found to be linear according to the Hull equation in the form [97]:

$$\beta\cos\theta = 4\eta\sin\theta + \frac{\lambda}{\langle D \rangle_{av}} \quad (4.5)$$

Where β is the angular line width of half maximum intensity at the Bragg angle θ , η is the strain and $\langle D \rangle_{av}$ is the mean crystal size. Value of 1.2×10^{-2} was estimated for the strain η from the slope of the straight line.

4.8 X- Ray photoelectron spectroscopy of TiO₂

The Ti⁺³ oxidation state of the metal remained stable, allowing the Ti⁺⁴ oxidation state to precipitate the hydroxide under the application of the potential. XPS characterization of the titanium hydroxide gel film deposited at room temperature is shown in Figure 4.9, the binding energies of the peaks were determined using the C1s peak at 284.5eV for calibration. The spin-orbit components Ti_{2p3/2} (458.2eV) and Ti_{2p1/2} (463.8 eV) peak locations are characteristic of anatase TiO₂ and suggest that Ti is in the +4 oxidation state and forming a Ti⁺⁴-O bond when reacting with air after the deposition. The fact that titanium is present with only one valence Ti⁺⁴ is typical of a stoichiometric surface [95][97-99].

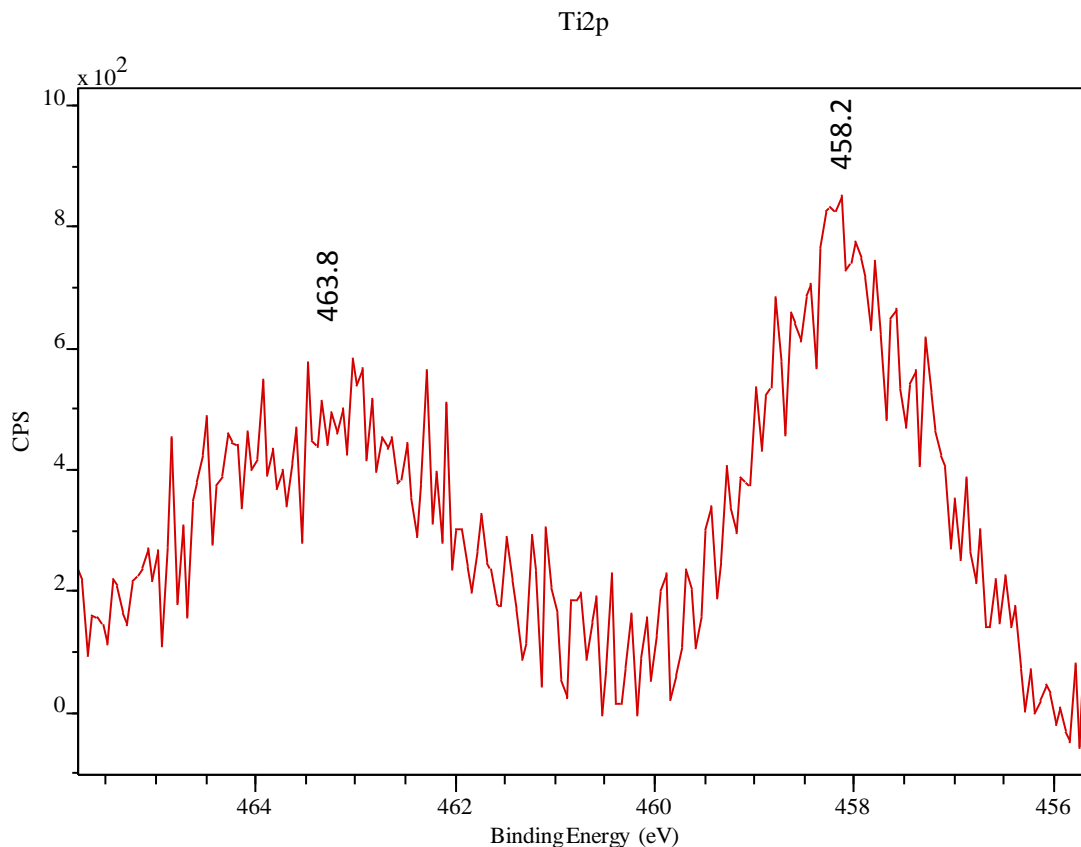


Figure 4.9. XPS spectra of titanium hydroxide gel film deposited at room temperature. The $2_{p1/2}$ and $2_{p3/2}$ peaks correspond to Ti+4 typical of anatase.

There is not apparent change in the spectrum of the film after heat treatment ($Ti_{2p3/2}$ 458.3eV and $Ti_{2p1/2}$ 463.8 eV). The separation between the $Ti_{2p1/2}$ and $Ti_{2p3/2}$ peaks ranges from 5.3eV (hydroxide gel) - 5.5eV (TiO_2 film). Small metallic particles of silvery gray colour were found to be deposited on the edges of the films which was the metallic titanium for the higher cathodic potential ($V < -1.2V$ versus Ag/AgCl).

4.9 TiO₂ film surface microstructure

Figure 4.10 shows an SEM picture of a film deposited at 338K after further heat treatment at 823K for 30 min. It can be observed that the film is formed by an aggregation of particles of open porous rough crystallites of size in the range 100-250nm.

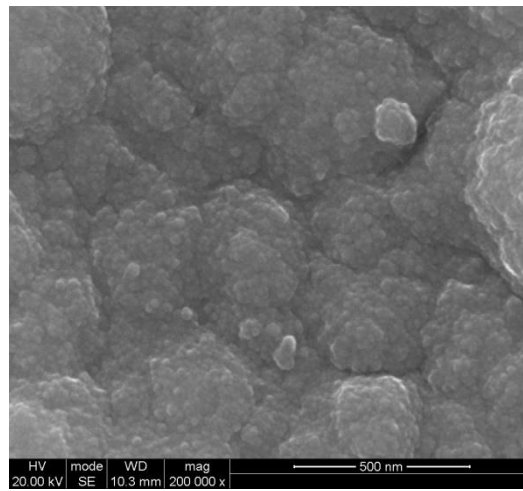


Figure 4.10 SEM photograph of TiO₂ electrodeposited film as deposited (deposition temperature, 338K) and further annealing at 823K for 30 min.

SEM pictures in Figure 4.11 show the surface of the samples deposited at 338K and 353K as deposited. The pictures reveal submicron cracks present on the surface of the film possibly caused when drying on ambient after taking the films out of the bath (water evaporation). It can be observed that the film is formed by an aggregation of amorphous particles that are bigger in size in the films deposited at higher temperature (353K).

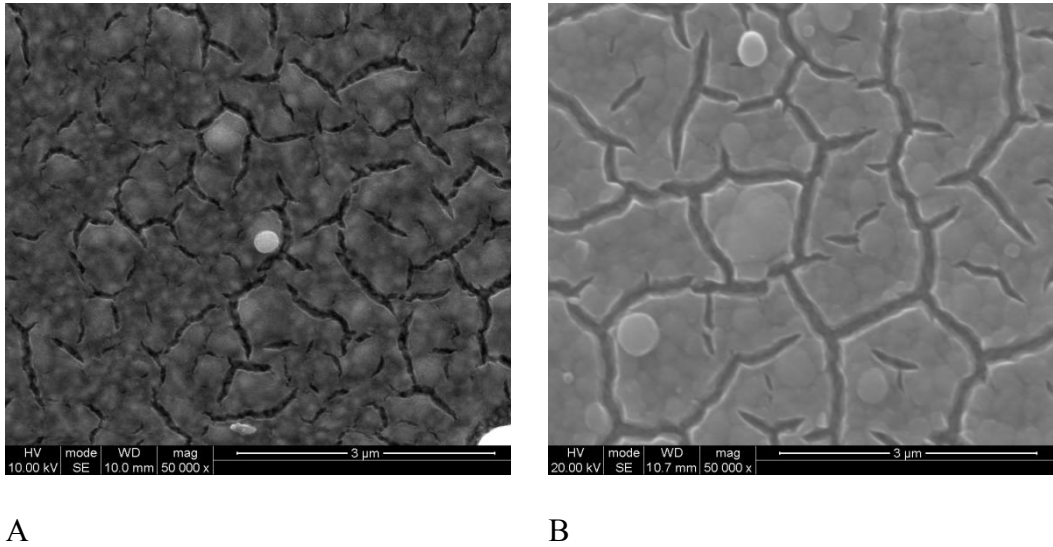
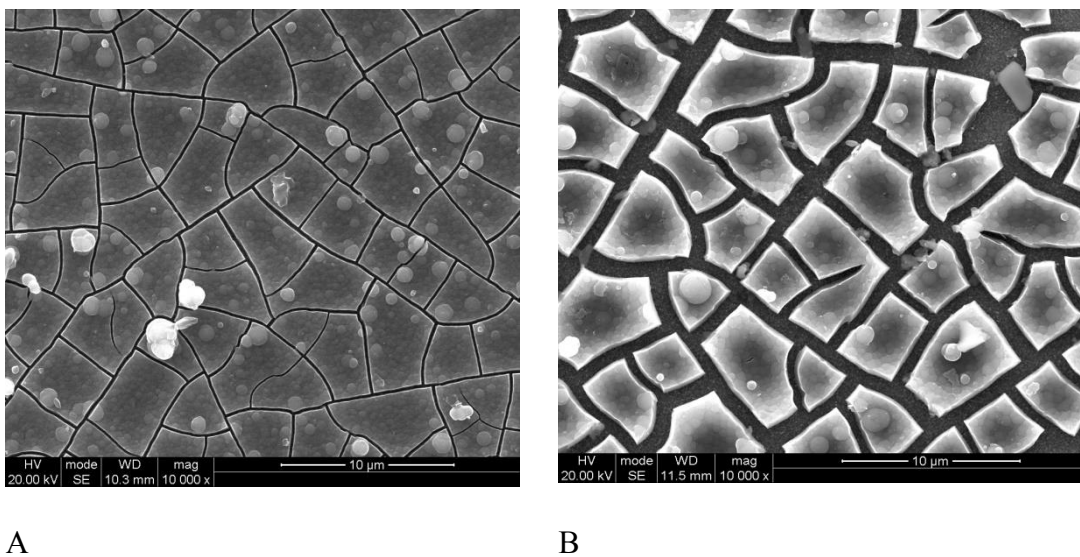


Figure 4.11 SEM photograph of TiO₂ electrodeposited films as deposited (A – deposition temperature, 338K; B – deposition temperature, 353K)

After heat treatment the films (823K, 30 min), the morphology changes with the annealing process and the cracks on the surface of the film grow in size (Figure 4.12.) leaving the film as an aggregate of rough crystallites of size in the range 100-500nm (C-D)



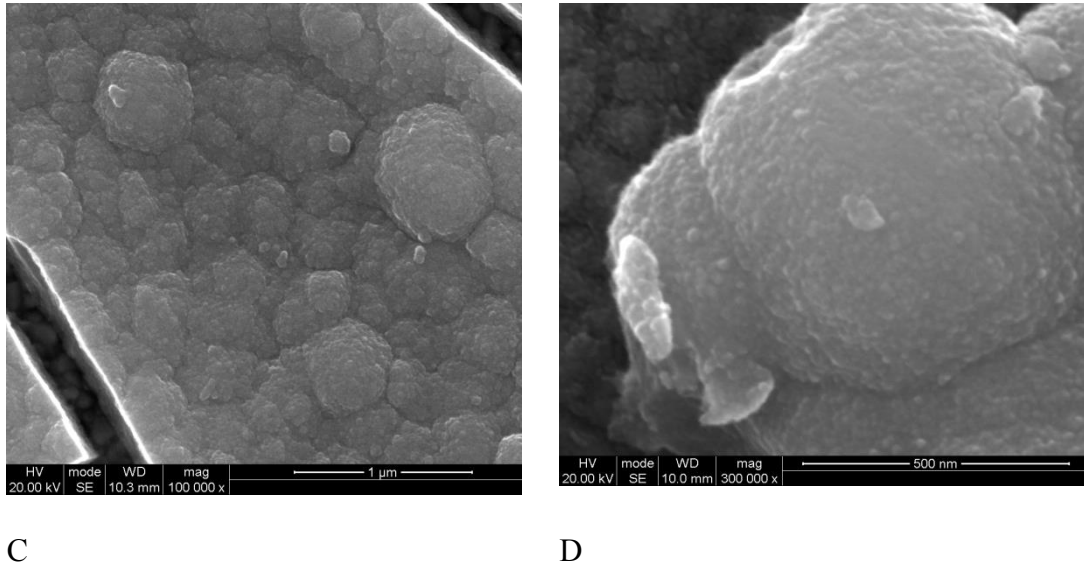


Figure 4.12 SEM photograph of TiO₂ electrodeposited films as deposited (A – deposition temperature, 338K; C – deposition temperature, 353K) and after annealing at 823K for 30 min (C,D) submicrophotography of film in (A). Cracks are visible on the films.

The presence of the cracks in the electrodeposited films, made impossible the electrical characterisation of the films.

4.10 Atomic force scans of as-deposited and heat-treated TiO₂ films

The AFM images are given in Figure 4.13 for as-deposited and annealed films, showing the transformation from amorphous to polycrystalline phase on annealing. The root mean square value of surface roughness was found to decrease from 35nm for the as-deposited films to 14nm in average for annealed TiO₂ films with an irregular textured surface. AFM analysis produced an average smaller value of 63nm for the mean grain size for the films deposited at 336K.

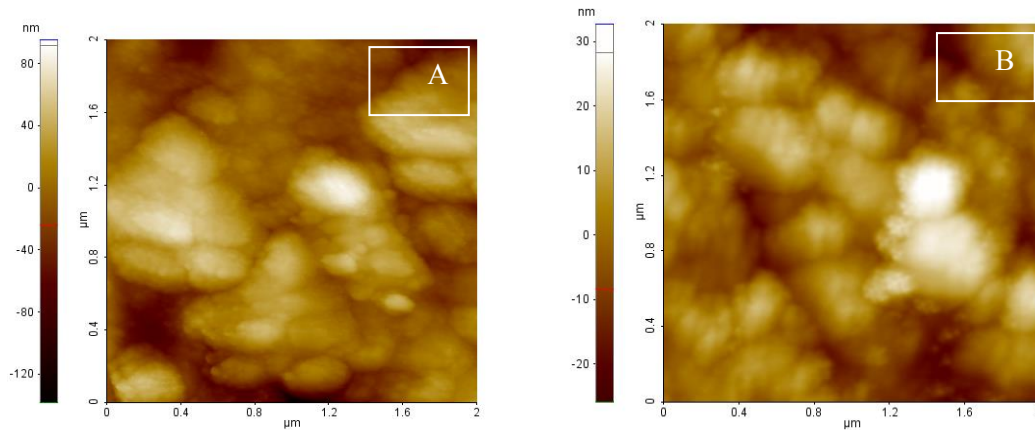


Figure 4.13 AFM images for TiO₂ films electrodeposited at 336K. A (as deposited). B (after annealing at 823K for 30 min).

The increase temperature is believed to possibly have vaporised the trapped water molecules leaving the pores empty and allowed the crystals to collapse. This led to increases in the crystal size and the removal of the interfacial interactions at the same time. The shape of the grains changes after heat treatment due to the formation of the crystallites. From spherical shaped grains as deposited, the TiO₂ becomes a very rough film. The mean square roughness value for the ‘as deposited’ film is 34.63nm. After annealing the mean square roughness decreases to 13.63nm. The crystallite aggregation is the cause of this change in morphology.

Chapter 5

Conclusions and Future Work

The present study was designed to include the consideration of the temperature of the chemical bath in the study of cathodic electrodeposition of TiO₂ anatase on conductive glass. The evidence from this study suggests that for constant potential, concentration of the bath, time and substrate, increasing the temperature of the electrochemical solution improves the optical absorption of the films.

This research has shown that the films obtained at 336K and 353K were highly rough in texture which is a very important characteristic for sunlight harvesting. Films deposited at 336K showed a higher crystallinity according to Raman and exhibited a higher optical absorbance.

A growth temperature dependent absorbance was noticed. At lower growth temperatures (296K and 318K) the absorption is significantly lower because at lower bath temperature the electrochemical reaction is mass transport limited, hence the cathodic deposition current is less, which results in thinner films. Indeed, films deposited at lower bath temperatures are thinner (confirmed by Dektak thickness monitor). At higher bath temperatures, the reaction is influenced by mass transport plus the migration of charged ions, thus increasing the cathodic current and so resulting in thicker films. These findings enhance our understanding of the importance of the electrochem-

ical bath temperature as a variable that must be taken into account to optimise the electrical and optical properties of anatase films.

Another major finding was that the change in colour around 335-345K in the electrochemical solution, corresponds with the highest optical absorption peak in the UV-vis graph for the subsequent films, indicating that there is a change in the chemistry of the solution that facilitates the electrodeposition of TiO₂ at -1.2V applied voltage.

Whilst this study did not confirm its chemistry, it did partially point to the ongoing lack of definite answers and supports the inconclusive evidence from earlier studies to the question of the exact nature of peroxotitanium solutions and their influence on the electrodeposited films. Due to the difficulty in understanding the chemistry of the peroxy complex of titanium, further optimization of the film deposition conditions should include the analysis of the interaction of temperature and pH of the bath.

A number of caveats need to be noted regarding the present study. Firstly, the fact that both, the as-deposited and the heat-treated films presented superficial cracks caused the no inclusion of electrical characterisation of the films. Although extreme care taken during the whole process of preparation of the films in order to prevent any thermal shock after electrodeposition and during and after heat treatment, it resulted difficult to avoid the occurrence of inhomogeneous forces at micro and nanoscale level.

Secondly, it would have been ideal to perform UV/vis analysis of the electrochemical solution at different temperatures to compare and correlate with the changes in both, colour and pH observed during this research.

Finally, a number of possible future studies using the same experimental set up are apparent. It would be advisable to design an experiment that includes the interaction of variables such as heat treatment, temperature of electrochemical bath and its possible correlation with pH and colour changes in the solution. Experiments directed to reduce the mismatch in thermal coefficient between substrate and deposited films are needed as well. It might be interesting performing multiple thin depositions, annealing after each one. Finding a relationship between thickness of the film and the amount or size of the cracks would help to identify and minimize its appearances.

Conducting experiments on the heat treatment would also prove helpful to avoid or diminish the cracks on the films; varying the temperature (decreasing preferably) or slowing down the cooling rate should be studied thoroughly in order to identify optimal parameters.

References

- [1] Satterfield CN (1991) *Heterogeneous catalysis in industrial practice*. 2nd edition p Medium: X; Size: Pages: (542 p).
- [2] Biener J, Wang J, & Madix RJ (1999) *Direct observation of the growth of vanadium on TiO₂(110)-(1x2)*. *Surface Science* 442(1):47-54.
- [3] Guo Q, Lee S, & Goodman DW (1999) *Vanadium oxides thin films grown on rutile TiO₂(110)-(1x1) and (1x2) surfaces*. *Surface Science* 1(20):38-48
- [4] Zhang Z & Henrich VE (1992) *Electronic interactions in the vanadium/TiO₂(110) and vanadia/TiO₂(110) model catalyst systems*. *Surface Science* 277(3):263-272.
- [5] Baumgartner HR (1983) *The oxide handbook* (IFI-Plenum, New York) 2nd Ed: 140.
- [6] KRONOS Worldwide I (2010) KRONOS Information 6.26. *KRONOS titanium dioxide pigments in water-reducible and water-soluble vehicles*. in *KRONOS Information Series*, ed KRONOS Worldwide I (KRONOS Worldwide Inc., Dallas).
- [7] Phillips LG & Barbano DM (1997) *The Influence of Fat Substitutes Based on Protein and Titanium Dioxide on the Sensory Properties of Low fat Milks I*. *Journal of dairy science* 80(11):2726-2731.
- [8] Dussert AS, Gooris E, & Hemmerle J (1997) *Characterization of the mineral content of a physical sunscreen emulsion and its distribution onto human stratum corneum*. *International Journal of Cosmetic Science* 19(3):119-129.
- [9] Selhofer H, Ritter E, & Linsbod R (2002) *Properties of Titanium Dioxide Films Prepared by Reactive Electron-Beam Evaporation from Various Starting Materials*. *Appl. Opt.* 41(4):756-762.
- [10] Braun JH (1997) *Titanium dioxide : A review* (Federation of Societies for Coatings Technology, Blue Bell, PA) (0361-8773).
- [11] Osburn L (2008) *Literature review on the application of titanium dioxide reactive surfaces on urban infrastructure for depolluting and self-cleaning applications*. *5th Post Graduate Conference on Construction Industry Development*, p 11.
- [12] Fujishima A & Honda K (1972) *Electrochemical Photolysis of Water at a Semiconductor Electrode*. *Nature* 238(5358):37-38.
- [13] Völz HG, et al. (2000) *Pigments, Inorganic*. *Ullmann's Encyclopedia of Industrial Chemistry*, (Wiley-VCH Verlag GmbH & Co. KGaA).

- [14] Hewitt JP (1992) Titanium Dioxide: *A Different Kind of Sunshield. Drug and Cosmetic Industry*. 51(3).
- [15] O'Regan B & Gratzel M (1991) *A low-cost, high-efficiency solar cell based on dye-sensitized colloidal TiO₂ films. Nature* 353(6346):737-740
- [16] Matsumoto Y, *et al.* (2001) *Room-Temperature Ferromagnetism in Transparent Transition Metal-Doped Titanium Dioxide. Science* 291(5505):854-856.
- [17] Dutta PK, *et al.* (1999) *Interaction of Carbon Monoxide with Anatase Surfaces at High Temperatures: Optimization of a Carbon Monoxide Sensor. The Journal of Physical Chemistry B* 103(21):4412-4422.
- [18] Titgemeyer EC, Armendariz CK, Bindel DJ, Greenwood RH, & Löest CA (2001) Evaluation of titanium dioxide as a digestibility marker for cattle. *Journal of Animal Science* 79(4):1059-1063.
- [19] Samsonov GV (1982) *The Oxide Handbook* (IFI / Plenum, New York and London) (English) 2nd Edition Ed p 463.
- [20] Tang H, Berger H, Schmid PE, Levy F, & Burri G (1993) Photoluminescence in TiO₂ anatase single crystals. *Solid State Communications* 87(9):847-850.
- [21] Downs B & Heese P (1997 - 2012) *The American Mineralogist Crystal Structure Database*. (Mineralogical Society of America and Mineralogical Association of Canada)
- [22] Diebold U (2003) *The surface science of titanium dioxide. Surface Science Reports* 48(5-8):53-229.
- [23] Smyth JR & Bish DL (1988) *Crystal Structures and Cation Sites of the Rock-forming Minerals* (Allen & Unwin).
- [24] Thomas AG, *et al.* (2007) *Comparison of the electronic structure of anatase and rutile TiO₂ single-crystal surfaces using resonant photoemission and x-ray absorption spectroscopy. Physical Review B* 75(3):035105.
- [25] Kavan L, Gratzel M, Gilbert SE, Klemenz C, & Scheel HJ (1996) *Electrochemical and Photoelectrochemical Investigation of Single-Crystal Anatase. Journal of the American Chemical Society* 118(28):6716-6723.
- [26] Wang H & Lewis JP (2006) *Second-generation photocatalytic materials: anion-doped TiO₂. Journal of Physics: Condensed Matter* 18(2):421.
- [27] Glassford KM & Chelikowsky JR (1992) *Structural and electronic properties of titanium dioxide. Physical Review B* 46(3):1284-1298.
- [28] Tang H, Levy F, Berger H, & Schmid PE (1995) *Urbach tail of anatase TiO₂. Physical Review B* 52(11):7771-7774.

- [29] Tang H, Prasad K, Sanjines R, Schmid PE, & Levy F (1994) *Electrical and optical properties of TiO₂ anatase thin films*. *Journal of Applied Physics* 75(4):2042-2047.
- [30] Orton JW & Powell MJ (1980) *The Hall-effect in polycrystalline and powdered semiconductors*. (Translated from English) *Rep. Prog. Phys.* 43(11):1263-1307 (in English).
- [31] Mardare D, Baban C, Gavrilă R, Modreanu M, & Rusu GI (2002) *On the structure, morphology and electrical conductivities of titanium oxide thin films*. *Surface Science* 507-510:468-472.
- [32] Mardare D & Rusu GI (2010) *Electrical conduction mechanism in polycrystalline titanium oxide thin films*. *Journal of Non-Crystalline Solids* 356(28-30):1395-1399.
- [33] Yildiz A, Lisesivdin SB, Kasap M, & Mardare D (2008) Electrical properties of TiO₂ thin films. *Journal of Non-Crystalline Solids* 354:4944-4947.
- [34] Mott NFS & Davis EA (1971) *Electronic processes in non-crystalline materials*, by N. F. Mott and E. A. Davis (Clarendon Press, Oxford).
- [35] Bessergenev V & Gomes HL (2010) *Electrical properties of thin-films wide-band gap semiconductor TiO₂ prepared by CVD*. *Physica Status Solidi (c)* 7(3-4):949-952.
- [36] Cronmeyer DC (1952) *Electrical and Optical Properties of Rutile Single Crystals*. *Physical Review* 87(5):876-886.
- [37] Forro L, et al. (1994) *High-Mobility n-type Charge Carriers in Large Single Crystals of Anatase (TiO₂)*. (Translated from English) *Journal of Applied Physics* 75(1):633-635 (in English).
- [38] Oja I, et al. (2006) *Structural and electrical characterization of TiO₂ films grown by spray pyrolysis*. *Thin Solid Films* 515(2):674-677.
- [39] Earle MD (1942) *The Electrical Conductivity of Titanium Dioxide*. *Physical Review* 61(1-2):56-62.
- [40] Grant FA (1959) Properties of Rutile (Titanium Dioxide). *Reviews of Modern Physics* 31(3):646-674.
- [41] Zhitomirsky I, et al. (1995) *Electrodeposition of Ceramic Films from Nonaqueous and Mixed-Solutions*. *Journal of Materials Science* 30(20):5307-5312.
- [42] Zhitomirsky I (1997) *Cathodic electrosynthesis of titania films and powders*. *Nanostructured Materials* 8(4):521-528.
- [43] Zhitomirsky I (1998) *Electrophoretic and electrolytic deposition of ceramic coatings on carbon fibers*. *Journal of the European Ceramic Society* 18(7):849-

856. Zhitomirsky I (1999) *Electrolytic deposition of oxide films in the presence of hydrogen peroxide. Journal of the European Ceramic Society* 19(15):2581-2587.
- [44] Zhitomirsky IaLG, (1996) *Cathodic electrosynthesis of ceramic deposits. Journal of the European Ceramic Society* 16(8):819-824.
- [45] Park NG, van de Lagemaat J, & Frank AJ (2000) *Comparison of Dye-Sensitized Rutile- and Anatase-Based TiO₂ Solar Cells. The Journal of Physical Chemistry B* 104(38):8989-8994.
- [46] Wessels K, et al. (2006) *Low-temperature preparation of crystalline nanoporous TiO₂ films by surfactant-assisted anodic electrodeposition. Electrochemical and Solid State Letters* 9(6):C93-C96.
- [47] Gao YF, et al. (2003) *Room temperature deposition of a TiO₂ thin film from aqueous peroxotitanate solution. Journal of Materials Chemistry* 13(3):608-613.
- [48] Natarajan C & Nogami G (1996) *Cathodic electrodeposition of nanocrystalline titanium dioxide thin films. Journal of the Electrochemical Society* 143(5):1547-1550.
- [49] Karuppuchamy S, et al. (2001) *Cathodic electrodeposition of TiO₂ thin films for dye-sensitized photoelectrochemical applications. Chemistry Letters* (1):78-79.
- [50] Karuppuchamy S, et al. (2002) *Cathodic electrodeposition of oxide semiconductor thin films and their application to dye-sensitized solar cells. Solid State Ionics* 151(1-4):19-27.
- [51] Karuppuchamy S, et al. (2006) *Photoinduced hydrophilicity of titanium dioxide thin films prepared by cathodic electrodeposition. Vacuum* 80(5):494-498.
- [52] Karuppuchamy S, Iwasaki M, & Minoura H (2006) *Electrochemical properties of electrosynthesized TiO₂ thin films. Applied Surface Science* 253(5):2924-2929.
- [53] Karuppuchamy S, Iwasaki M, & Minoura H (2007) *Physico-chemical, photoelectrochemical and photocatalytic properties of electrodeposited nanocrystalline titanium dioxide thin films. Vacuum* 81(5):708-712.
- [54] Karuppuchamy S & Jeong JM (2005) *Super-hydrophilic amorphous titanium dioxide thin film deposited by cathodic electrodeposition. Materials Chemistry and Physics* 93(2-3):251-254.
- [55] Gastinger E (1954) *Über die Konstitution des farbgebenden Komplexes beim Titannachweis mit Wasserstoffperoxyd. Zeitschrift für anorganische und allgemeine Chemie* 275(6):331-337.
- [56] Schwarz R (1933) *Notiz Über das Wesen der kolorimetrischen Titanbestimmung. Zeitschrift für anorganische und allgemeine Chemie* 210(3):303.

- [57] Schaeppi Y & Treadwell WD (1948) *Über die kolorimetrische Bestimmung der Stöchiometrie einiger Farbkomplexe. Helvetica Chimica Acta* 31(2):577-588.
- [58] Babko AK & Volkova AI (1951) *The Colored Complex of Titanium with Hydrogen Peroxide. J. Gen. Chem* 21:1949.
- [59] Mori M, Shibata M, Kyuno E, & Ito S (1956) *Reaction of Hydrogen Peroxide with Titanium (IV) at Different pH Values. Bulletin of the Chemical Society of Japan* 29(8):904-907.
- [60] Patel CC & Mohan MS (1960) *Nature of the Colour-forming Species in Peroxy Titanium Sulphate. Nature* 186(4727):803-804.
- [61] Cai R, Itoh K, & Sun C (2005) *pH Effect on the Optical Properties of Peroxo-Titanium Complex. Nanoparticles and Nanostructures in Sensors and Catalysis*, eds Zhong C-J, Kotov NA, Daniell W, & Zamborini FP.
- [62] Muhlebach J, Muller K, & Schwarze G (1970) *Peroxo Complexes of Titanium. Inorganic Chemistry* 9(11):2381-&. Schwarzenbach D (1970) *Structure of a chelated dinuclear peroxytitanium(IV). Inorganic Chemistry* 9(11):2391-2397.
- [63] Comba P & Merbach A (1987) *The Titanyl Question Revisited. Inorganic Chemistry* 26(8):1315-1323.
- [64] Gatehouse BM, Platts SN, & Williams TB (1993) *Structure of anhydrous titanyl sulfate, titanyl sulfate monohydrate and prediction of a new structure. Acta Crystallographica Section B* 49(3):428-435.
- [65] Sergienko V (2004) *Structural characteristics of peroxo complexes of group IV and V transition metals. Review. Crystallography Reports* 49(6):907-929.
- [66] Plieth, W. (2008). *Electrochemistry for materials science*. Elsevier Science.
- [67] Bard, A. J., & Faulkner, L. R. (1980). *Electrochemical methods: fundamentals and applications* (Vol. 2). New York: Wiley.
- [68] Garcia Sole, J. Bausa, L E & Jaque, D (2005) *An Introduction to the Optical Spectroscopy of Inorganic Solids*. UK, John Wiley and Sons, Ltd pp: 1-38
- [69] Szymenski, H A (1967) *Raman Spectroscopy: Theory and Practice*. USA, Plenum Press pp: 1-43
- [70] Fox, M (2001) *Optical Properties of Solids*. USA, Oxford University Press pp: 1-24
- [71] <http://www2.chemistry.msu.edu/faculty/reusch/virttxtjml/spectrpy/uv-vis/uvspec.htm>

- [72] C Kittel 2005 *Introduction to Solid State Physics*. USA, John Wiley and Sons, Ltd pp: 23-43
- [73] B D Cullity, S R Stock 2001 *Elements of X-Ray Diffraction*. USA, Prentice Hall pp: 89-122
- [74] <http://www4.nau.edu/microanalysis/Microprobe-SEM/Instrumentation.html>
- [75] Goldstein, J., Newbury, D. E., Joy, D. C., Lyman, C. E., Echlin, P., Lifshin, E. & Michael, J. R. (2003). *Scanning electron microscopy and X-ray microanalysis*. Springer.
- [76] Wagner, C. D. (1979). *Handbook of X-ray photoelectron spectroscopy*. G. E. Muilenberg (Ed.). Perkin-Elmer.
- [77] http://m.portalnano.ru/read/tezaurus/en/r_f_spectroscopy
- [78] <http://micromagazine.fabtech.org/archive/04/06/chong.html>.
- [79] Blanchard, C. R. (1996). *Atomic force microscopy. The chemical educator*, 1(5), 1-8
- [80] <http://scixchange.missouri.edu/blog-post/afm-an-introduction-part-iii/>
- [81] Grzmil, B., Grela, D., Kic, B., et al. (2008). *The influence of admixtures on the course of hydrolysis of titanyl sulfate. Polish Journal of Chemical Technology*, 10(3), pp. 1-49.
- [82] Pauporté, T. and D. Lincot (2001). "Hydrogen peroxide oxygen precursor for zinc oxide electrodeposition II—Mechanistic aspects." *Journal of Electroanalytical Chemistry* 517(1–2): 54-62.
- [83] Ohsaka, T., Izumi, F., & Fujiki, Y. (2005). *Raman spectrum of anatase, TiO₂. Journal of Raman Spectroscopy*, 7(6), 321-324.
- [84] Fletcher, S. I., Sillars, F. B., Carter, R. C., Cruden, A. J., Mirzaeian, M., Hudson, N. E., ... & Hall, P. J. (2010). *The effects of temperature on the performance of electrochemical double layer capacitors. Journal of Power Sources*, 195(21), 7484-7488.
- [85] Zhang, W. F., He, Y. L., Zhang, M. S., Yin, Z., & Chen, Q. (2000). *Raman scattering study on anatase TiO₂ nanocrystals. Journal of Physics D: Applied Physics*, 33(8), 912.
- [86] Wood DL & Tauc J (1972) *Weak Absorption Tails in Amorphous Semiconductors. Physical Review B* 5(8):3144-3151.
- [87] Mott, N.F.S. and E.A. Davis, *Electronic processes in non-crystalline materials*. 2nd ed. ed. 1979, Oxford: Clarendon Press. xiv,590p.

- [88] Moss, T.S., G.J. Burrell, and B. Ellis, *Semiconductor opto-electronics*. 1973, London: Butterworths. xii,441p.
- [89] Ray, A. K., & Hogarth, C. A. (2000). *On the analysis of experimental data for optical absorption in non-crystalline materials*. *Journal of Physics D: Applied Physics*, 23(4), 458.
- [90] S. R. Elliott, *Physics of amorphous materials*, Longman: London and New York, (1983)
- [91] Xiong, J., Das, S. N., Kim, S., Lim, J., Choi, H., & Myoung, J. M. (2010). *Photo-induced hydrophilic properties of reactive RF magnetron sputtered TiO₂ thin films*. *Surface and Coatings Technology*, 204(21), 3436-3442.
- [92] Tian, G. L., H. B. He, et al. (2005). "Effect of microstructure of TiO₂ thin films on optical band gap energy." *Chinese Physics Letters* 22(7): 1787-1789.
- [93] Majumdar, A., H. Z. Xu, et al. (2004). "Bandgap energies and refractive indices of Pb_{1-x}Sr_xSe." *Journal of Applied Physics* 95(3): 939-942.
- [94] McCarthy, G. J., J. M. Holzer, et al. (1991). *Evaluation of reference x-ray-diffraction patterns in the icdd powder diffraction file*. New York, Plenum Press Div Plenum Publishing Corp.
- [95] Sanjines, R., H. Tang, et al. (1994). "Electronic-structure of anatase TiO₂ oxide." *Journal of Applied Physics* 75(6): 2945-2951.
- [96] Vella, E., R. Boscaino, et al. (2007). "Irradiation effects on the absorption edge of silica glass." *Journal of Non-Crystalline Solids* 353(5-7): 559-563.
- [97] B. D. Cullity, S.R. Stock, *Elements of X-ray diffraction*. 3rd ed. Ed. Prentice – Hall International: Upper Saddle River, N.J., (2001) p xviii, 664 p.
- [98] C. R. Wagner, W.M. Davis, L.E Moulder, J.F Muilenburg, G. E, Eds., *Handbook of X-Ray Photoelectron Spectroscopy*. Perkin-Elmer Corporation Physical Electronics Division, 6509 Flying Cloud Drive, Eden Prairie, Minnesota 55344 (1979).
- [99] Gil-Sun Kim, S. G. Ansari, Hyung-Kee Seo, Young-Soon Kim, Hyung-Shik Shin. *J. Appl Phys.*, 101 (2007), 024314.
- [100] Takeno, N. Atlas of Eh-pH diagrams. Geological Survey of Japan Open File Report, 419, 102 (2005)

Publication

C. Cruz and A.K. Ray, “Morphological and Elemental Studies on Titania Thin Films Electrodeposited at Different Bath Temperatures”, *Journal of The Electrochemical Society*, 159 (2) E1-E7 (2011).